

Needle-free Drug Delivery Using Shock Wave Techniques

by

Atanas Pavlov

B.S., Physics

Massachusetts Institute of Technology, 2004


Submitted to the Department of Mechanical Engineering
in Partial Fulfillment of the Requirements for the Degree of
Master of Science in Mechanical Engineering

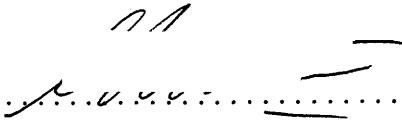
at the

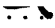
Massachusetts Institute of Technology

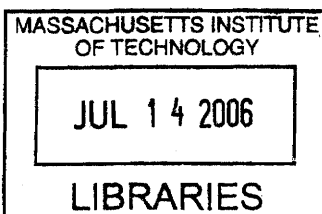
June 2006

© Massachusetts Institute of Technology
All Rights Reserved

Signature of Author 
Department of Mechanical Engineering
May 6, 2006

Certified by 
Ian W Hunter
Hatsopoulos Professor of Mechanical Engineering and
Professor of Biological Engineering
Thesis Supervisor

Accepted by 
Lallit Anand
Professor of Mechanical Engineering
Chairman, Department Committee on Graduate Students



ARCHIVES

Needle-free Drug Delivery Using Shock Wave Techniques

by

Atanas Pavlov

Submitted to the Department of Mechanical Engineering on May 12, 2006
in Partial Fulfillment of the Requirements for the Degree of
Master of Science in Mechanical Engineering

ABSTRACT

A recent advancement in the area of needle-free injection systems has been the development of devices capable of epidermal delivery of powder medications. These devices use high-pressure compressed gas to accelerate drug particles 2 to 50 μm in size to velocities of 200 to 1000 m/s. At these speeds the particles have sufficient momentum to penetrate the skin barrier and reach the viable epidermal layers. The devices offer much better control over the depth of penetration than traditional hypodermic needles, a factor particularly important in vaccine delivery. However they still have not found wide spread use, because of their cost.

We studied the parameters determining the performance of these devices and used that knowledge to create a simple and reusable device capable of delivering 3 to 10 mg of powder formulation to the viable epidermis. Furthermore we showed that hydrogen-oxygen combustion could be used to create the shock wave required to accelerate the drug particles. This proves that portable reusable devices powered by hydrogen can be constructed and used for vaccine and medication delivery.

Thesis Supervisor: Ian W. Hunter

Title: Professor of Mechanical Engineering and Professor of Biological Engineering

Acknowledgements

I would like to thank my advisor, Prof. Ian Hunter, for giving me the opportunity to work in one of the most amazing laboratories in MIT both as UROP and as a graduate student. I also want to thank him for his support and mentorship.

I want to thank Dr. Andrew Taberner for his invaluable help in designing experiments and interpreting results.

I want to thank Dr. Cathy Hogan for bearing with my ignorance in the subject of biology and for trying to fill up the gaps; for explaining to me how to run experiments and for helping me analyze the results.

I want to thank Norwood Abbey for providing the funding for this project.

I would like to thank my mother for all her support and her efforts to motivate me to go on.

I would like to thank Jordan Brayanov for helping me “convert” to mechanical engineering and for teaching me how to use the machine shop.

Nayden Kambouchev provided me great help to understand the basic theoretical principles of compressible fluid dynamics.

Andrea Bruno always listened patiently to my questions, helped me when he could and always entertained me with his Sicilian wit.

Thanks to all my colleagues and friends for their support and advice and all the good time we have had together.

Table of contents

Acknowledgements.....	3
Table of contents.....	4
List of figures.....	6
1 Introduction.....	8
1.1 Intradermal needle-free drug delivery	8
1.2 Thesis Overview	9
2 Background.....	10
2.1 Structure of the skin.....	10
2.1.1 Epidermis.....	10
2.1.2 Dermis.....	11
2.2 Targeting the skin	12
2.2.1 Vaccines.....	12
2.2.2 Other medications	12
2.3 Going needle-free.....	13
2.4 Current needle-free devices	14
2.5 The PowderJect Device.....	15
2.5.1 Structure of the device	15
2.5.2 Experimental studies.....	17
3 Shock Wave Dynamics.....	22
3.1 Wave propagation in gases	22
3.2 Small amplitude waves	24
3.3 Large amplitude waves	24
3.4 Characterization of the shock wave	27
3.4.1 Stationary shock relations.....	27
3.4.2 Traveling shock wave	30
3.5 Expansion Waves.....	31
3.6 Shock Tube	33
3.7 Shock wave formation distance	36
4 Experimental Setup.....	38
4.1 The rupture/combustion chamber and the shock tube	41
4.2 Gas flow control.....	42
4.3 Pressure sensors	42
4.4 High speed camera.....	43
4.5 Optical setup	44
4.6 Oscilloscope.....	45
4.7 Lexan Enclosure.....	45
5 Experiments with Compressed Nitrogen	48
5.1 Overview.....	48
5.2 Membrane rupture.....	48
5.2.1 Rupture Pressure	50
5.2.2 Membrane Dynamics	50
5.3 Shock wave generation	52
5.3.1 Pressure Equilibration.....	52
5.3.2 Shock tube under different conditions	53

5.3.3	Shock strength and speed variations.....	54
5.4	Injection experiments with eversible membrane	56
5.5	Eversion of the drug membrane.....	57
5.6	Alternative designs for the drug membrane.....	59
5.7	Injections into tissue	61
6	Combustion Analysis.....	63
6.1	Energy density of combustion	63
6.2	Thermodynamic calculations for H ₂ combustion	63
6.2.1	Complete Combustion	65
6.2.2	Incomplete Combustion.....	66
6.3	Effects of temperature on the shock wave	68
7	Hydrogen Combustion Experiments.....	70
7.1	Modifications of the setup	70
7.2	Hydrogen flame propagation and pressure rise	71
7.3	Shock wave propagation.....	74
7.4	Accelerated plastic slug	76
7.5	Alternative Methods of Powering the Device.....	78
8	Conclusions and Future Work	81
Appendix	82
A	Material And Physical Properties	83
A.1	Physical Properties of Air	83
A.2	Physical Properties of Hydrogen	83
B	Drawings.....	84
C	Code and simulations.....	86
C.1	Matlab Shock wave graphs	86
C.2	MathCad shock wave model.....	87
C.3	Combustion calculations.....	89
References	93

List of figures

Figure 2-1: a) Skin diagram b) layers of the Epidermis.....	11
Figure 2-2: a) Dermal PowderJect Device with converging-diverging nozzle b) Oral PowderJect device using Shock-Tube c) Detailed view of the plunger valve and the first membrane d) Detailed view of the second membrane (Oral PowderJect).	16
Figure 2-3: Measurements on the Dermal PowderJect device.....	20
Figure 3-1: Propagation of a disturbance along a pipe.	23
Figure 3-2: Distortion of a pressure wave of finite amplitude due to the nonconstant wave speed across the wave.	26
Figure 3-3: a) Propagating shock wave in a pipe before the transformation	28
Figure 3-4: Propagation of an expansion wave along a pipe.	32
Figure 3-5: Operation of a shock tube	34
Figure 3-6: Shock wave strength versus initial pressure ratio at two different conditions.	36
Figure 4-1: Experimental setup for studying the operation the needle-free injector powered by compressed nitrogen.....	39
Figure 4-2: Rupture chamber and shock tube models	40
Figure 4-3: Pressure transducer and couplers (a) Kistler 211B2 pressure transducer (b) 5114 coupler and power supply (c) 5118B2 coupler and power supply.....	43
Figure 4-4: Phantom high-speed camera.	44
Figure 4-5: Optical setup for transmission measurements of velocity.	45
Figure 4-6: Lexan “bulletproof” enclosure.	46
Figure 4-7: Completed device setup.	47
Figure 5-1: Pressure measurements of the chamber pressure demonstrating (a) repeatability of rupture pressure (b) independence of supply pressure.	49
Figure 5-2: Rupturing process for different membranes.....	51
Figure 5-3: Pressure equilibration after membrane rupture	53
Figure 5-4: Shock wave behavior at different downstream end conditions of the shock tube.....	54
Figure 5-5: Shock wave propagation at different membrane thicknesses/ shock wave strengths.	55
Figure 5-6: Comparison between theoretical predictions and experimental measurements for the shock wave speed	56
Figure 5-7: Tungsten particles ejected from the drug membrane.	57
Figure 5-8: Series of frames showing the process of everting the drug membrane.....	58
Figure 5-9: Experiments firing.....	59
Figure 5-10: (a, b) Head attachment for the injection device (c) stabilized membrane traveling on the pins.....	60
Figure 5-11: Tungsten particles cloud created with the device and the head attachment.	60
Figure 5-12: Transdermal injection in lamb skin.....	61
Figure 5-13: Epidermal injection in pig skin	62
Figure 6-1: Final temperature of the product gases in Hydrogen-Oxygen combustion process.....	66

Figure 6-2: Thermodynamic state of the hot products, assuming equilibrium state is reached.	68
Figure 7-1: Triggering circuit for the high-speed camera.	71
Figure 7-2: Images from constant volume stoichiometric hydrogen burning.	72
Figure 7-3: Measured pressure during the combustion process.	73
Figure 7-4: Shock wave pressure measurements.	75
Figure 7-5: Combustion generated shock wave propagating in a translucent shock tube.	76
Figure 7-6: Plastic slug accelerated by the hot gases in the shock tube.	77
Figure 7-7: Electrolyzers for hydrogen production.	79

1 Introduction

1.1 Intradermal needle-free drug delivery

In spite of the boom in the biomedical industry and the advancements made in the development of therapeutic drugs over the last few decades, little progress has been made in the delivery methods used. Syringes and hypodermic needles are still the most widespread way to deliver medications, vaccines and local anesthetics. As simple and effective as this method is, it still has its problems. The instinctive fear of sharp needles is one of them, although not the most important one. Cross contamination and needle re-use is an issue, especially in poor third-world countries. For certain medications to be effective, injection location is of key importance. Positioning and controlling this location by hand is not an easy task. It requires certain skill, and when it comes to large scale mass vaccinations finding experienced medical personnel is a potential problem. Vaccines are particularly sensitive to injection depth because different cells have very different abilities to mount effective immune response. The lower viable layers of the epidermis are often the target for various vaccines and manually controlling the injection depth with the necessary precision of less than 50 μm is virtually impossible. While liquid jet needle-free injectors have been developed in recent years and provide some depth control, delivery to the epidermis is still problematic. Therefore a new technique was needed for epidermal injection and such a technique was the needle-free powder drug delivery.

The current powder drug delivery devices use high pressure gas to accelerate a dose of drug particles to very high speeds, so that they can penetrate through the dense keratinized layers of the epidermis and reach the lower viable epidermal layers. Variations of the device were successfully tested for delivery of vaccines, local anesthetics and gene therapy medications. However these devices have not found wide spread use because they are expensive and designed for single use. A new, less expensive

and reusable device is needed which will finally allow the full potential of the needle-free devices to be utilized in large scale immunizations and mass therapeutic drug delivery. The goal of our research was to prove that such a device could be made and to provide practical means for powering it.

1.2 Thesis Overview

In Chapter 2 the advantages of needle-free devices will be explained in detail, as well as the requirements they have to meet, the current state of the market and the operational principles of the PowderJect device, which is used as a base point for this research. Chapter 3 will provide a theoretical background for modeling the complicated transient phenomena on which these devices rely. Chapter 4 describes the components of the laboratory setup used to experimentally study and optimize the functioning of the needle-free devices. Chapter 5 describes the experiments and the results we obtained from our compressed-nitrogen powered device. The theoretical fundamentals of hydrogen-oxygen combustion are discussed in Chapter 6 in view of the possibility of using it to power a reusable version of the device. The results from experiments with the hydrogen device are presented in Chapter 7. Finally Chapter 8 presents our conclusions and guidelines for possible future work on the device.

2 Background

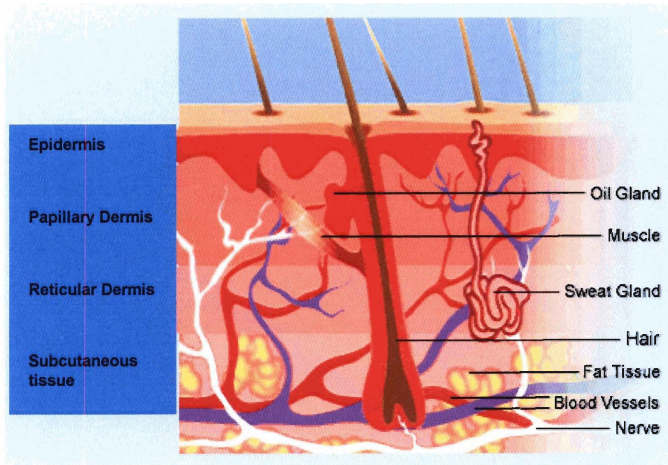
2.1 Structure of the skin

The skin is the outermost body organ and its main purpose is to retain and protect all other organs from the surrounding world. Additionally, it is a major barrier against pathogens and chemicals, provides temperature insulation and regulation, and synthesizes certain vitamins and pigments.

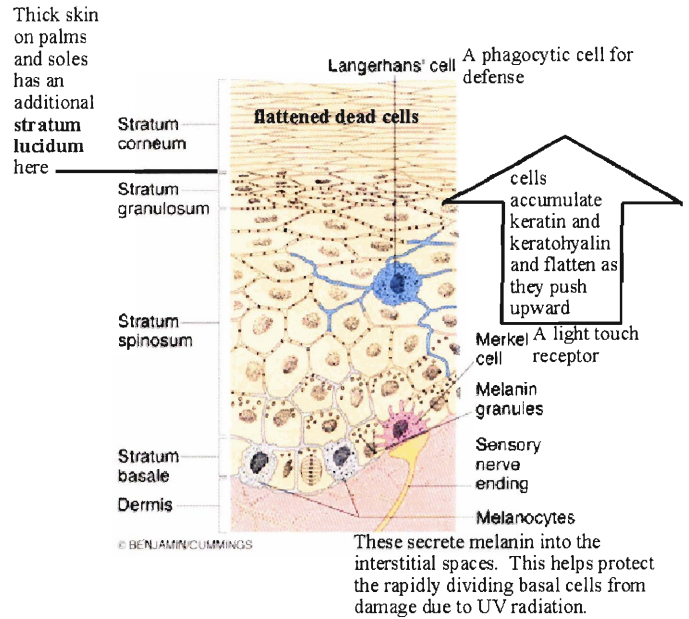
The skin varies in thickness and structure between species and within a given species depends on the anatomical location. For humans the range of thicknesses is 0.5 to 5 mm. The skin consists of three layers- epidermis, dermis and subcutaneous tissue.[1, 2]

2.1.1 Epidermis

The epidermis is classified as stratified epithelial tissue. The five layers of the epidermis (strata) counting from inside out are basale, spinosum, granulosum, lucidum, and corneum (Figure 2-1b). The first two layers form the stratum Malpighii, which is the viable part of the epidermis. The next two layers are thin and are only present at certain locations of the skin (palms, feet). Stratum corneum, which in humans is 10-15 μm thick, is the outermost layer and consists of flattened, highly compacted and ordered cells. They have thickened cell membranes, no nuclei and the cytoplasm is replaced with keratin protein, which gives them rigidity. The surface of the skin is covered with fine furrows. Similar furrows are also observed at the interface between the dermis and the epidermis, making the boundary wavy.



(a)



(b)

Figure 2-1: a) Skin diagram b) layers of the Epidermis

Image source [3, 4].

Cell division occurs in the stratum Malpighii, and the daughter cells travel through the layers to the surface, to renew the dead cells in the corneum, which eventually get stripped off. The process is called *keratinization* and it takes about 30 days for a cell to reach the stratum corneum. During this period of time the cell differentiates to become a keratinocyte. Although keratinocytes are the predominant type of cells in the epidermis, there are also melanocytes, which produce skin pigments, Merkel cells which respond to pressure and Langerhan's cells which process and present antigens to the T-cells in the lymph nodes.

2.1.2 Dermis

The dermis is the layer immediately below the epidermis and it is built out of connective tissue. It contains blood vessels, which by means of diffusion nourish the viable epidermal layers. Its thickness is 0.2 to 4 mm and consists of reticular and subepithelial layers. The reticular layer contains a complicated mesh of coarse collagenous fiber, which forms an elastic net. The subepithelial (papillary) layer is similar

to the reticular layer, but contains finer collagenous fibers. The dermis also contains sweat glands, and hair follicles.

Below the dermis is the subcutaneous tissue, which is a type of fascia. It attaches the skin to the muscles and bones and being very flexible, provides freedom for the skin to move. Many fat cells are present in the subcutaneous tissue.

2.2 Targeting the skin

2.2.1 Vaccines

It has long been known that skin is a passive part of the immune system, physically preventing pathogens from entering the body. Recent studies [5-7], however, indicate that skin also plays an active part in the immune response. Keratinocytes produce and respond to cytokines that cause inflammation. The Langerhan's cells process, transport and present antigen proteins to the T-cells located in proximity to the skin. Furthermore in the perivascular area of the papillary dermis a high concentration of T-cells is observed. Although these cells are not skin specific, their proliferation is partially induced by the cytokines produced in the epidermis.

Due to its significance for the immune system and its strong reaction to antigens, the skin is often chosen as a target for vaccines. Studies [8] of the efficiency of influenza vaccine, show that intramuscular administration of the vaccine leads to low efficiency. Chen et al. [9] demonstrate using mice as test subjects, that delivery of vaccine to the epidermis is not only possible but also results in an improved immune response. Henderson et al. [10] show that intradermal vaccination against Hepatitis B achieves efficiencies comparable to, if not better than, intramuscular vaccination using lower doses.

2.2.2 Other medications

The skin has been targeted not only by vaccines, but also by various drugs. Local anesthesia traditionally applied either on the surface in the form of a spray or as an intramuscular injection, can be administered intradermally. This improves the effect, compared to surface application and avoids the pain associated with deep injection.

Dentists would appreciate intradermal anesthesia, because of the frequency they have to use it and the sensitivity of the mouth. Skin has also drawn attention in gene therapy. DNA fragments are inserted into the cell nuclei and incorporated into the host DNA where they are expressed to yield a specific protein product. This could be done either for vaccination or treatment purposes.

2.3 Going needle-free

Years of research have been devoted to eliminating the needles used to administer injections. Needle phobia, together with needle stick injuries and the improper reuse of needles are serious issues. Needle reuse is especially problematic in poor overpopulated third world countries, where pandemic spread of diseases occurs on a regular basis and where mass vaccinations are most needed. Kane [11] estimates that every year about 8 to 16 million Hepatitis B, 2.3 to 4.7 million Hepatitis C and 80 000 to 160 000 HIV A infections result from unsafe injections.

A second problem, associated with epidermal injection, is positioning the needle during the injection. Intramuscular injection requires certain skills, but even for professionals, epidermal injection is a challenge. The epidermis, which has a thickness often less than a millimeter, requires a very fine needle and extreme precision and stability both during insertion of the needle and injection of the drug. Ensuring such precision in mass vaccination is virtually impossible. A needle free system, on the other hand, having predetermined injection parameters, that have been shown to repeatably deliver drug to a desired depth, is a viable option for mass immunization.

Vaccine stability is an additional factor, which has to be taken into account, especially in third world countries, where the supply of vaccines is very irregular and they are often stored under improper conditions. Powder vaccines have been proven to retain their strength over longer periods of times than liquid vaccines. Furthermore some vaccines are presently produced in powder form, and only dissolved before injection. The natural next step would be to directly inject the vaccines in powder form. However this is impossible with the traditional syringe and needle, and a novel device is needed to replace it.

2.4 Current needle-free devices

There are two classes of needle-free devices - liquid injectors and powder injectors.

Liquid injectors are usually actuated using a spring or compressed gas and use a piston and a small orifice (50 μm to 200 μm) to create narrow high speed jet of liquid that penetrates the skin. Bioject has marketed a reusable device [12] powered by a CO₂ cartridge. Using disposable needle-free syringes, it is capable of delivering up to 1mL as an intramuscular or subcutaneous injection. The Mini-Ject™ device [13] by Biovalve, uses a chemical charge to deliver 0.1 to 1.3 mL of drug intradermally, subcutaneously or intramuscularly, as desired. The needle-free injection device [14] developed by the MIT Bioinstrumentation Lab, using a voice coil actuator, and the MicroJet device developed in Berkeley [15] are amongst the first to continuously control the parameters of the injection during the injection cycle, and thus achieve a specific injection profile.

Although all of the above devices have been shown to reproducibly deliver liquid dye intradermally, subcutaneously, and intramuscularly only the powder based injectors reproducibly target the epidermis. Designed for shallower penetration depth than the liquid injectors, these devices can be specifically adjusted for injections into the stratum corneum or the stratum Malpighii. Because these devices are not limited to a narrow jet of liquid, they could be designed to cover a larger footprint- a few tens of square millimeters of skin. As a result excessive localized damage of the tissue would be limited thereby obviating immune response to wounding. In addition, spreading vaccine antigens over a larger area could ultimately result in a stronger immune response as more antigens may be transported by the Langerhan's cells to the lymph nodes. With anesthetics a single shot can replace a series of shots performed in order to desensitize an entire area.

Examples of commercial devices delivering powder formulations are the AlgoRx device used to deliver lidocaine, the Helios Gene Gun [16] used for gene therapy and the device [17] used by Chiron for vaccine delivery. They all utilize compressed helium as a power source, and different size and density particle carriers to achieve the penetration depth desired. The AlgoRx and the Chiron devices are both variations of the PowderJect device, which is the subject of the next section.

2.5 The PowderJect Device

The PowderJect device is one of the first and most successful commercial needle-free devices for powder drug delivery. It was initially developed by Brian Bellhouse in Oxford around 1994, and later marketed as two different devices[18]- the Dermal PowderJect and the Oral PowderJect. The working principle of the Oral PowderJect device is the basis for much of the research described in this thesis and therefore understanding the design and the operation of the original device is an important step towards constructing and characterizing an improved device.

2.5.1 Structure of the device

The CAD models of the two devices shown on Figure 2-2 are created using drawings and descriptions from the patents of the Dermal [19] and the Oral[20] PowderJect devices. The two devices are quite similar and both have a gas tank in the back filled with helium at a pressure of 4 to 8 MPa. A Plunger with two O-rings forms a valve that opens into the rupture chamber when pressed. The rupture chamber serves as a gas accumulator and the pressure there steadily rises as it is filled with gas. Once the rupture pressure of the membrane at the end of the rupture chamber is reached, it tears open and releases the gas into the channel formed in the head attachment of the device. The membrane and the head attachments differ for the two devices.

The Dermal PowderJect device utilizes a double rupturable membrane. The drug particles are placed between the two membranes. Inelastic material, such as polyester, is used for the membranes, so that they rupture almost instantaneously at a pressure of 2 to 8 MPa. The downstream membrane opens first, releasing the drug, and shortly afterwards, the upstream membrane opens, releasing the gas that projects the drug particles down the channel. The shape of the channel is that of a converging-diverging nozzle.

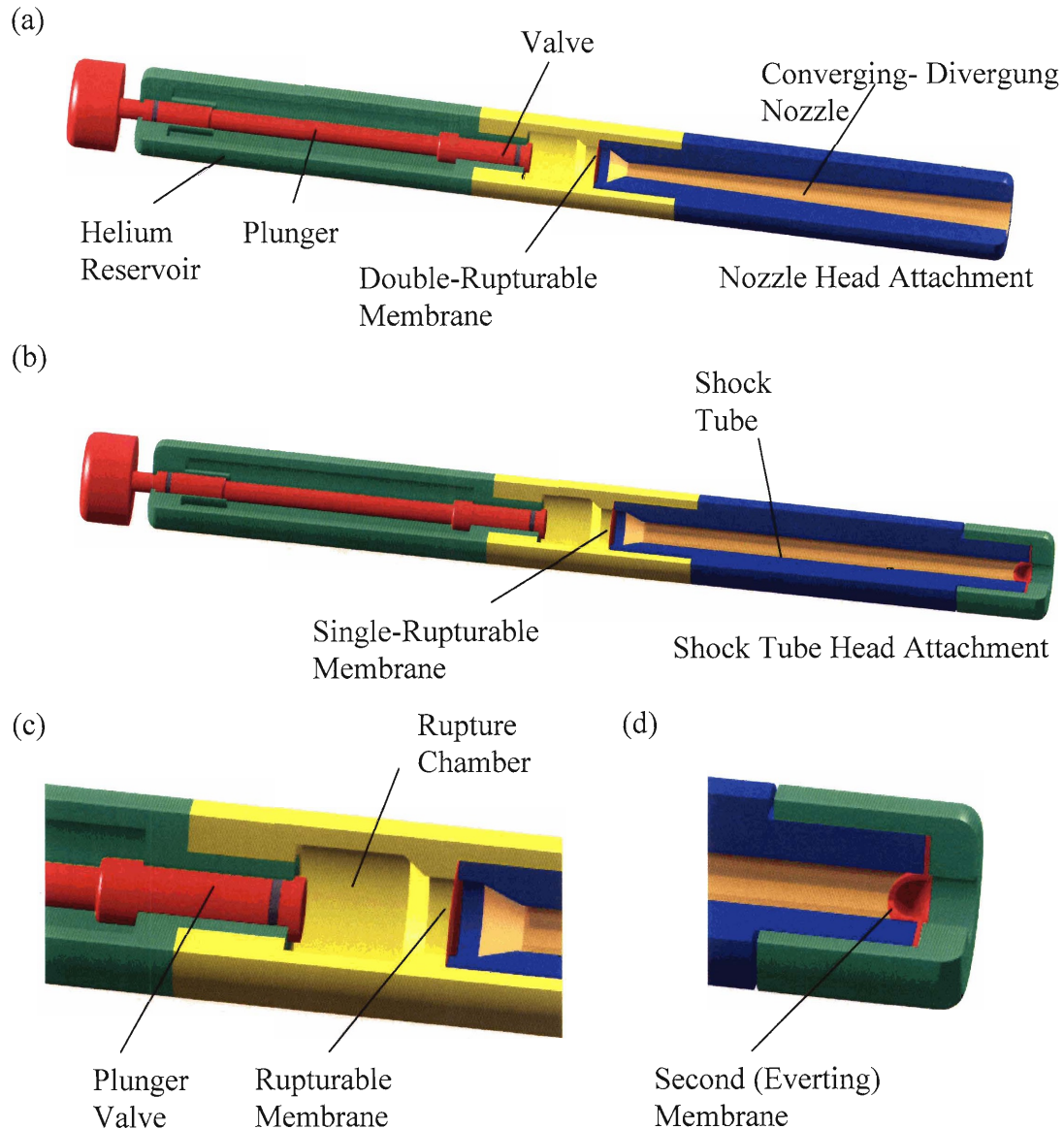


Figure 2-2: a) Dermal PowderJect Device with converging-diverging nozzle b) Oral PowderJect device using Shock-Tube c) Detailed view of the plunger valve and the first membrane d) Detailed view of the second membrane (Oral PowderJect).

It is known from compressible gas dynamics that as the gas propagates down the convergent part of the channel it compresses and accelerates until it reaches sonic velocity at the throat of the nozzle. At sonic velocity, the equations of the flow change signs, and as the gas expands in the divergent part of the nozzle, it keeps on accelerating. The diverging angle should be small, or otherwise the flow will not be able to expand fast

enough and boundary layer separation will occur at the walls- angle of 15° or less is used. The exit velocity of the gas is determined by the geometry of the nozzle and the pressure in the rupture chamber. As the gas accelerates, it also accelerates the drug particles, and in the end of the channel, they have comparable velocities. Velocities up to 1000 m/s are claimed using this technique.[19]

The Oral PowderJect device uses quite a different method of accelerating the powder. The rupture chamber is sealed by a single membrane, which again ruptures at predetermined pressures, similar to the pressures used in the nozzle device. The channel in the head attachment does not have a diverging part, but a constant cross section. At its end a second membrane is affixed with the drug particles attached to its external surface. The membrane has a concave shape inward. It is constructed either of relatively strong elastic material (polyurethane) or an easily deformed inelastic material (polyester). In both cases, it is bistable and everts outwards when a pressure above a threshold pressure is applied. During the operation of the device, after the first membrane ruptures, a compression wave is released and propagates down the channel. This wave has a sharp pressure gradient, which is determined by the time it takes the membrane to rupture, and, as the wave propagates, the gradient becomes steeper and steeper until a shock wave is formed. The shock wave, hitting the second membrane, causes an almost instantaneous rise in pressure behind it. The pressure reaches values close to those in the rupture chamber and rapidly everts the membrane. The membrane, acting as a sling, catapults the drug particles at very high speed. Provided it is tough enough to resist the pressure, the membrane does not rupture, and therefore retains the gas inside the device. This makes the device quieter and safer to use.

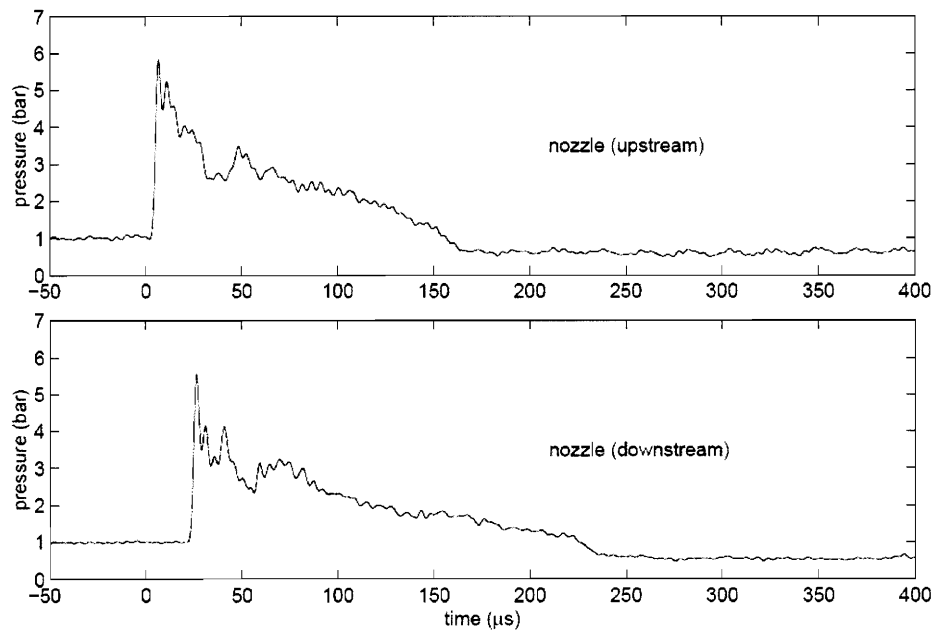
2.5.2 Experimental studies

The two articles [18, 21] describe studies on the gas and particle dynamics of the PowderJect devices. The two parameters studied are pressure and particle velocities. Pressure is measured using fast response pressure transducers mounted on the gas reservoir, the rupture chamber and at different locations of the head attachment channel. The particles velocity was measured using Doppler Global Velocimetry (DGV). In the DGV technique [26,27], a laser beam passed through a cylindrical lens creates a laser

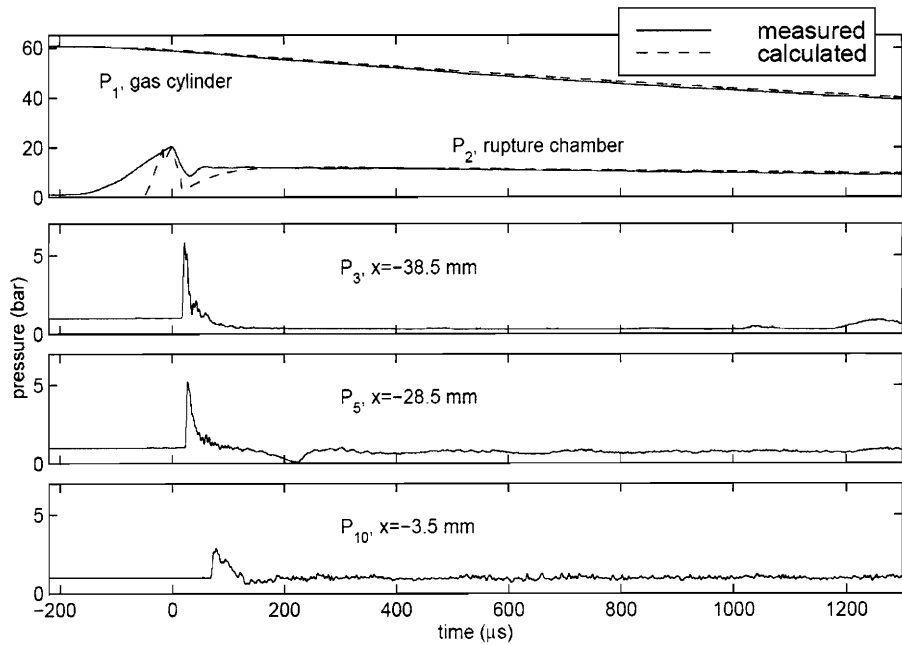
sheet which is sent towards the moving particles. The particles reflect light which is Doppler-shifted because of their relative motion to the source. The reflected light is then passed through a filter (an iodine cell), which has very narrow absorption lines in the frequency range of the laser. The intensity of the light transmitted through the cell is a function of the frequency shift and therefore of the particle velocity. The light is collected, recorded by a camera and compared to unfiltered light to achieve a high signal to noise ratio. The strength of this method is that it can measure the velocity of every particle in every point of the laser sheet at a single shot. If the sheet is directed along the axis of the device exit channel, a single snapshot can yield measurements along the whole length of the channel.

Two different sets of nozzles were used with the Dermal device- a contoured nozzle, having a very small diverging angle (and consecutively small exit to throat area ratio), and a conical nozzle, having much higher divergence angle and area ratio. Two pressure sensors were used in the case of the contour nozzle and ten in the case of the conical nozzle, the first two being in the reservoir and the rupture chamber respectively. Figure 2-3a and b show pressure measurements for the two nozzles; Figure 2-3c shows Mach number (see Section 3.1) measured, compared to the calculated Mach number, assuming no shock wave is present inside the nozzle; and Figure 2-3d shows DGV measurements for the conical nozzle. The distance x is measured with respect to the exit of the device.

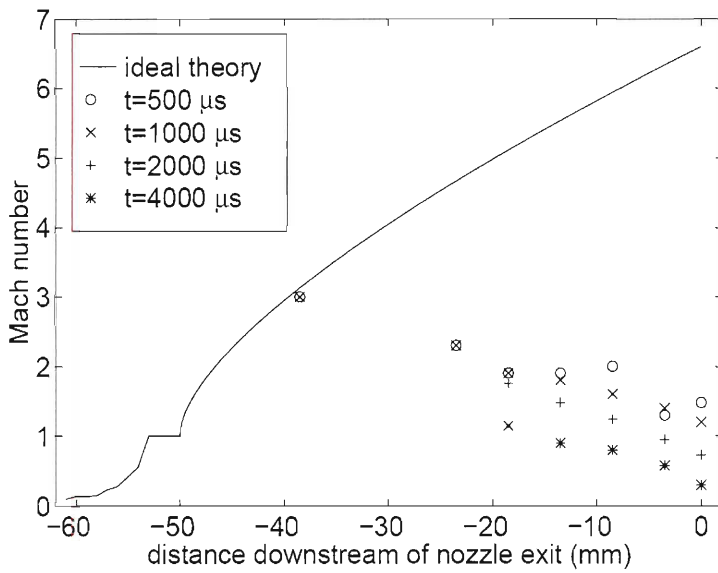
With either nozzle we observe a rapid rise in pressure, caused by a shock wave traveling downstream, followed by a transient response lasting for approximately 200 μ s. Perhaps a second shock wave causes a sudden change in the behavior in the following interval and we observe a slowly varying flow with a pressure slightly below atmospheric. The flow is supersonic, overexpanded and quasistatic. In the case of conical nozzle, due to the high expansion ratio, the initial shock wave slows down from about 850 m/s to 610 m/s at the end of the nozzle. The flow is unstable, and after the initial transient, a shock wave is observed traveling upstream, which eventually sets up the static shock wave inside the nozzle. As can be seen from Figure 2-3c, this decreases the Mach number at the nozzle exit significantly below the value predicted by theory.



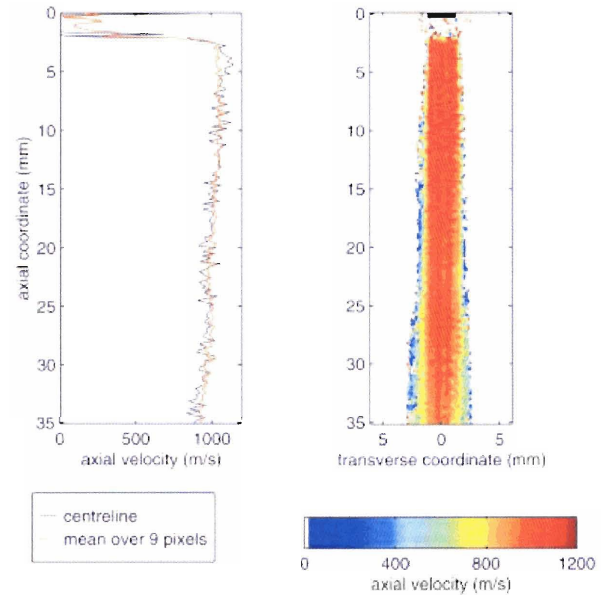
(a)



(b)



(c)



(d)

Figure 2-3: Measurements on the Dermal PowderJect device.

Pressure measurements with the a) contoured b) conical nozzle profile c) Calculated and measured Mach number for conical nozzle d) DGV of polymer microsphere in a contoured nozzle.

Picture source [21].

The speed of polymer microspheres was measured using DGV to assess the nozzle geometries. The contour nozzle yielded velocities of 740 to 810 m/s for 26.1 μm spheres and 1000 to 1050 m/s for 4.7 μm spheres. The velocities of the particles exiting the conical nozzle were in the range 310 to 550 m/s independent of the particle size. This indicates that the conical nozzle underperforms the contour nozzle because in the latter flow becomes subsonic within the nozzle. In the case of the contour nozzle the particle velocities are much higher than the velocities of the initial shock wave propagation, which suggest the acceleration is due to the quasisteady gas processes rather than the initial gas blowdown. Finally in the case of the conical nozzle the particles exit with speeds close to the speed of the gas flow (velocity and size not correlated), while in the contour nozzle case the particles probably move slower than the flow.

The articles also describe animal studies and clinical trials which have been performed with both devices. Doses of 2 mg and 1 mg of testosterone were delivered with the Dermal and Oral PowderJect respectively. Blood probes showed positive in both

cases and skin response was also acceptable. In clinical trials 3 mg lidocaine was delivered to people, and local anesthesia was achieved within 1 to 3 minutes.

3 Shock Wave Dynamics

This chapter gives a brief overview of the fundamentals of compression and expansion wave propagation in gases and shows how to use them to model the transient phenomena occurring during expansion of compressed gas in a one dimensional tube of constant cross section. For more details refer to [22-24].

3.1 Wave propagation in gases

The state of a gas at each point in space and time is characterized by state variables such as pressure, temperature, density, entropy, velocity and Mach number. In an equilibrium steady state only two of these are independent, and all the rest can be determined using thermodynamics equations. If the gas is in motion, but the state in every point in space does not change with time, three variables are necessary to fully define the state at each location. In our treatment of the gas phenomena the processes we consider will be reversible and isentropic (except for some localized entropy generation). In this case the variables usually used to characterize the flow are pressure, temperature and Mach number.

If any of the parameters of the gas is changed from its equilibrium value, then this disturbance propagates through the gas in the form of a pressure wave. For example, Figure 3-1 shows a piston at the end of the pipe which suddenly starts moving to the right at time $t=0$. As a result, the pressure in front of the piston momentarily increases. The created pressure gradient drives the gas away from the high pressure area, and compresses the gas ahead. Thus the pressure increase by the motion of the piston creates a compression wave, propagating to the right, as shown in the figure. If the piston instead started moving to the left, then the pressure of the gas in front would suddenly decrease, and the pressure gradient would drive the gas to the left. In this case a rarefaction wave will propagate down the pipe to the right.

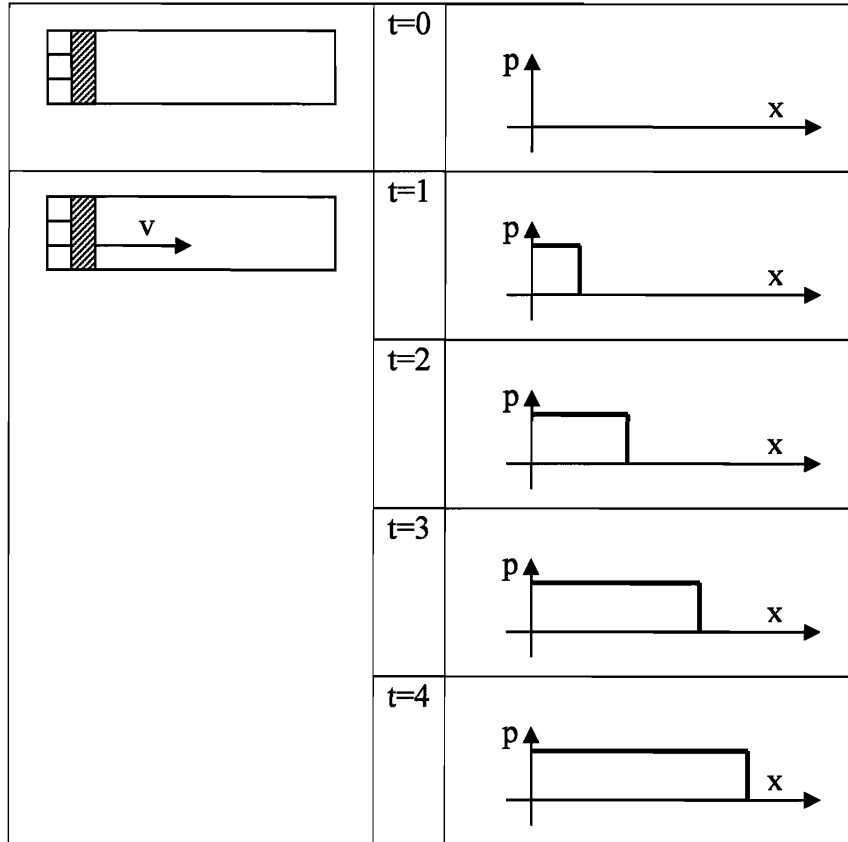


Figure 3-1: Propagation of a disturbance along a pipe.

The velocity of the pressure wave depends on the gas properties, and is called speed of sound. It is given by the equation:

$$a = \sqrt{\partial p / \partial \rho} . \quad (3-1)$$

Assuming that the wave propagation is an isentropic process, for the case of ideal gas, the pressure and density are related by:

$$p\rho^{-\gamma} = const , \quad (3-2)$$

where $\gamma = c_p / c_v$ is the specific heat ratio. Combining this equation with the ideal gas law:

$$pV = \nu RT , \quad (3-3)$$

we obtain for the speed of sound:

$$a = \sqrt{\frac{\gamma RT}{\mu}} = \sqrt{\frac{\gamma p}{\rho}} . \quad (3-4)$$

For air ($\gamma = 1.4$, $\mu = 29\text{g/mol}$) at room conditions ($p = 101\text{ kPa}$, $T = 293\text{ K}$), the resulting speed is 343 m/s . This is the familiar speed of sound at room conditions, which however, clearly depends on temperature, being proportional to \sqrt{T} .

Using the speed of sound in a gas as a reference speed, we can define the Mach number as:

$$M = u/a . \quad (3-5)$$

For subsonic speeds $M < 1$, and for supersonic speeds $M > 1$. Gases behave significantly differently depending on whether $M > 1$ or $M < 1$.

3.2 Small amplitude waves

When the amplitude of the pressure waves is much smaller than the equilibrium value of the pressure at any given point, they are described as “sound” waves. Audible sounds fall into this category. Sound intensity of 85dB , which is loud enough to damage the ear (over a long period), corresponds to a pressure amplitude of 0.36Pa or $3.56 \times 10^{-4}\%$ pressure variations.

One-dimensional sound waves do not change shape as they propagate in space and time. The equation describing them is:

$$p(x,t) = f(x \pm at) . \quad (3-6)$$

Here a is the speed of sound given by (3-4). The negative sign denotes wave propagation towards the right, and the positive sign- towards the left. If a wave has an arbitrary shape at a given moment of time, it will retain that shape as it propagates. Every portion of the wave will propagate at the same speed, and no distortion will be observed.

3.3 Large amplitude waves

Large amplitude means that the pressure disturbances that occur are not small compared to the equilibrium value of the pressure. In this case we cannot apply (3-6) in a straight- forward manner, because the different parts of the wave travel at different speeds, and the processes describing the wave are much more complicated.

As previously mentioned, processes associated with the wave propagation are assumed to be isentropic (i.e. they are reversible and heat exchange and viscosity are neglected). Therefore, a change in one of the state variables causes changes in the rest of them. The fluctuations of pressure, carried by the wave, cause fluctuations in the density, temperature and velocity of the fluid. Equation (3-2) shows that local increase in the pressure leads to increase in the density. Rearranging Equation (3-2), we can express the dependence between pressure and temperature as:

$$p^{1-\gamma} T^\gamma = \text{const.} \quad (3-7)$$

Therefore increase in pressure leads to increase in temperature, and vice versa. But as the speed of sound increases with temperature, the wave will propagate faster through areas of compression than through areas of rarefaction. This effect is negligible in the case of sound waves, due to the low amplitude of the temperature variations, but as the amplitude increases, the effect becomes more and more significant.

Let us consider again a sine pressure wave propagating to the right. The initial shape of the wave is shown in Figure 3-2a. The pressure is equal to the equilibrium value at points B and D, below the equilibrium at A (the gas is in expansion), and above the equilibrium at C (the gas is in compression). The temperature is therefore T_0 at points B and D, $T_0 - \Delta T$ at point A and $T_0 + \Delta T$ at point C. If the speed of sound in the gas is a_0 (at temperature T_0), then points B and D travel at speed a_0 , point A travels at speed lower than a_0 and point C- at speed higher than a_0 . As we follow the propagation of the wave with time, in a reference frame moving with the wave at speed a_0 , we will see A lagging behind B, and C leading ahead of B, as shown in Figure 3-2b. As time goes by, the ABC portion of the wave becomes flatter, and the CD portion of the wave becomes steeper. If this process continued infinitely, the point C will get ahead of D and the slope of CD will change sign, as shown in Figure 3-2d. This however is physically impossible because it would mean that in points like D there would be three different values for the pressure. The contradiction comes from the fact that we considered all the processes to be isentropic and neglected viscosity. What happens in reality is that as the slope DC becomes steeper and steeper, the pressure gradient and the velocity gradient at point D become so high that viscosity starts to play role.

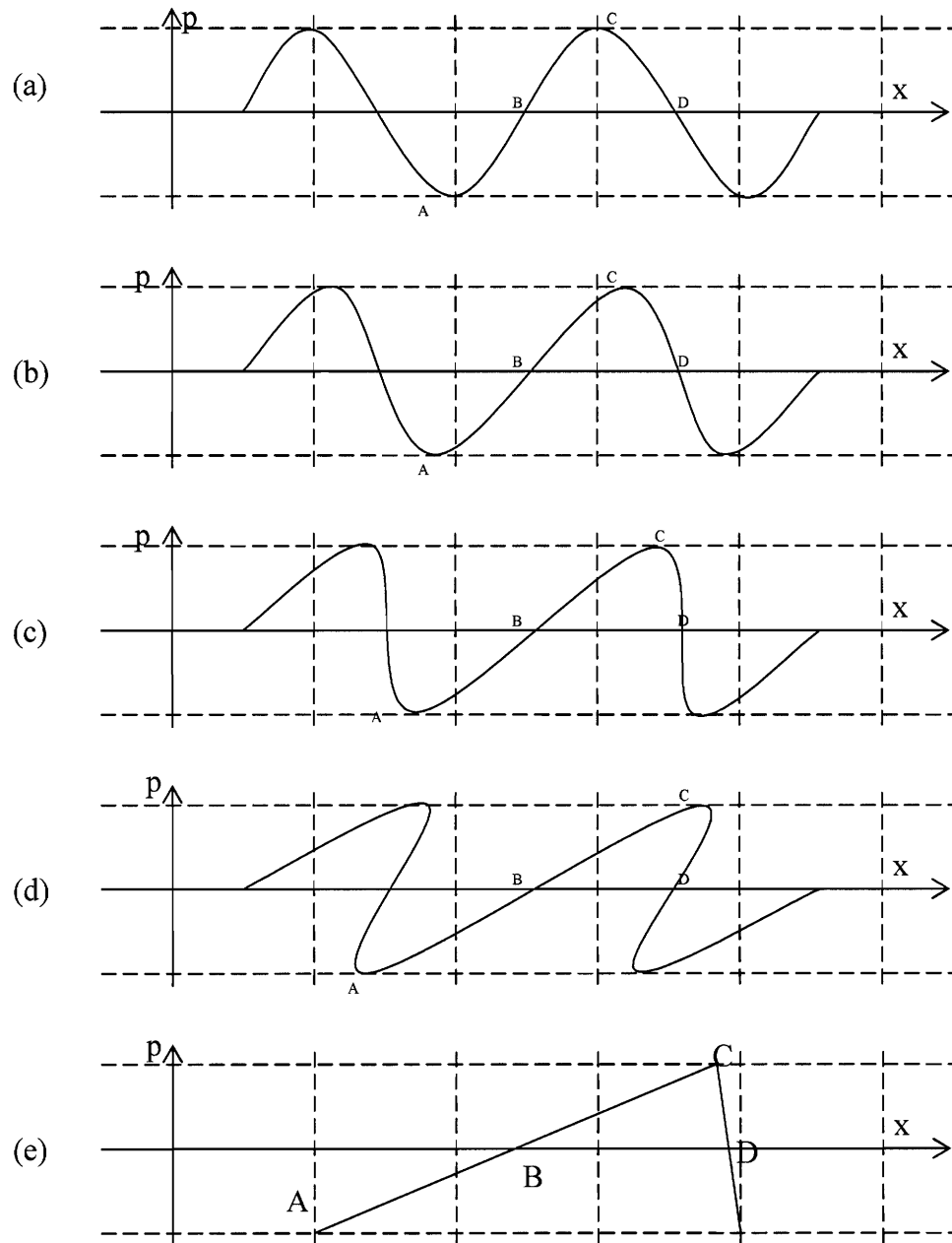


Figure 3-2: Distortion of a pressure wave of finite amplitude due to the nonconstant wave speed across the wave.

We are used to viscosity causing diffusion of momentum in direction normal to the velocity. However there is no reason why this should not happen also in direction along the local velocity of the fluid. Momentum diffusion along the streamlines is almost always neglected, because the term is much smaller than the convective term. However in this case, the velocity gradient along the streamline becomes so high, and the thickness of

the zone in which momentum is transferred to the gas ahead so small, that the viscous term becomes dominant. The wave reaches equilibrium state, shown in Figure 3-2e, which consists of repeating quick compressions followed by slow expansions. The compressive part is called shock wave, due to the high pressure gradient across it. Due to the significance of friction forces inside the shock wave, the flow there is not isentropic and positive entropy is generated. However, the flow on both sides of the shock wave remains isentropic, and the gas equations for this type of flow do hold on both sides of the shock region.

The width of the shock wave and the pressure profile are determined by the equilibrium of the inertial forces, trying to increase the pressure gradient, and the viscous forces, trying to decrease it. Therefore the properties of a fully developed shock wave depend on the properties of the gas and the pressures on the two sides of the shock wave, but do not depend on the initial shape of the wave. Provided transverse viscosity is negligible and given enough time, each compressive section of the wave will turn into a shock wave.

3.4 Characterization of the shock wave

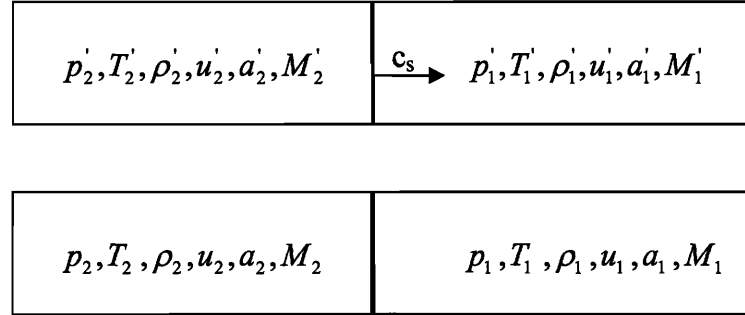
In section 3.3 we explained that the properties of the gas vary from point to point. More specifically the speed of sound is not constant everywhere and depends on the conditions at any given point. Therefore a stricter definition of the Mach number is:

$$M = u/a_{local} . \quad (3-8)$$

3.4.1 Stationary shock relations

Let us consider a one dimensional shock wave in a pipe of constant cross-section propagating to the right at speed c_s . The wave could be created by sudden motion to the right of a piston located at the left end of the pipe. This motion compresses the air in front of the piston bringing the gas in the pipe to a non-equilibrium state. The resulting compression wave propagates to the right, and eventually develops into a shock wave. Let us create a coordinate system traveling together with the shock front. We will derive equations describing the flow in this reference system, in which the shock is stationary

and then we will transform back to the laboratory reference frame. As seen in Figure 3-3, the primed quantities refer to the propagating shock wave, while the unprimed quantities refer to the stationary shock wave. Also the index 1 refers to the region on the right of the shock wave (the region ahead of the wave, not yet reached by it), and the index 2 refers to the region on the left of the shock wave (the region behind the shock wave).



**Figure 3-3: a) Propagating shock wave in a pipe before the transformation
b) Stationary shock wave after the transformation.**

The first equation governing the flow is the continuity equation for constant cross-sectional area:

$$\rho_1 u_1 = \rho_2 u_2. \quad (3-9)$$

The momentum equation for the case of compressible flow is:

$$p_1 + \rho_1 u_1^2 = p_2 + \rho_2 u_2^2. \quad (3-10)$$

Dividing the second equation by the first one, and using (3-4) in the form $a^2 = \gamma p / \rho$, we arrive at the equation:

$$\frac{a_1^2}{\gamma u_1} + u_1 = \frac{a_2^2}{\gamma u_2} + u_2. \quad (3-11)$$

Now we employ the energy equation which states that:

$$\frac{c_p}{\mu} T_1 + \frac{u_1^2}{2} = \frac{c_p}{\mu} T_2 + \frac{u_2^2}{2}. \quad (3-12)$$

We use the fact that $c_p = R \frac{\gamma}{\gamma - 1}$ and (3-4) again to obtain:

$$\frac{a_1^2}{\gamma-1} + \frac{u_1^2}{2} = \frac{a_2^2}{\gamma-1} + \frac{u_2^2}{2} = K. \quad (3-13)$$

Equation (3-13) holds for any two points in the flow, and more generally says that the value of K is constant along a streamline. If we label with u^* and a^* the value of the fluid velocity and the local speed of sound for a point in the flow for which $M=1$ (i.e. $u^*=a^*$) then we can relate the value of K to that a^* :

$$K = \frac{\gamma-1}{2(\gamma+1)} (a^*)^2. \quad (3-14)$$

Expressing a_1 and a_2 from (3-13) and substituting in (3-11) we finally get:

$$u_1 u_2 = (a^*)^2. \quad (3-15)$$

If we define $M^* = u/a^*$ then $M_1^* M_2^* = 1$. To relate the M and M^* quantities, we can use (3-14) and (3-13) written for the point at which M is evaluated. Simple algebra gives us:

$$M^* = \frac{(\gamma+1)M^2}{(\gamma-1)M^2 + 2}. \quad (3-16)$$

Clearly when $M=1$, then $M^*=1$; when $M<1$, then $M^*<1$; and when $M>1$, then $M^*>1$. This along with the fact that $M_1^* M_2^* = 1$ means that the flow on one side of the shock wave is supersonic and on the other side is subsonic. In the reference frame of the stationary shock wave the speed of the gas entering the shock wave is higher than the speed of the gas exiting the shock wave. Therefore supersonic flow enters from the right, and subsonic flow leaves to the left. It turns out that a stationary shock wave is the only way that a supersonic flow can become a subsonic flow and therefore is always present when supersonic flow decelerates.

The relationship between M_1 and M_2 can easily be derived using (3-16) and it is:

$$M_2^2 = \frac{1 + \frac{\gamma-1}{2} M_1^2}{\gamma M_1^2 - \frac{\gamma-1}{2}}. \quad (3-17)$$

Having obtained the relation between the Mach numbers across the shock wave, we can derive the relations between the kinematical and the thermo-dynamical quantities in the two regions. Continuity together with Equation (3-16) gives us the densities and the velocities.

$$\frac{\rho_2}{\rho_1} = \frac{u_2}{u_1} = (M_1^*)^2 = \frac{(\gamma + 1)M_1^2}{(\gamma - 1)M_1^2 + 2}. \quad (3-18)$$

To express the pressure, we use continuity again and the momentum equation:

$$p_2 = p_1 + \rho_1 u_1 (u_1 - u_2). \quad (3-19)$$

3.4.2 Traveling shock wave

Having derived the equations for a stationary shock wave, let us transform back to the laboratory reference frame to obtain the equations for a traveling shock wave. Remembering that the gas ahead of the shock wave is stationary, and using simple Galilean transformations between the reference frames we obtain:

$$\begin{aligned} u_1' &= 0, \\ u_2' &= u_1 - u_2, \\ c_s &= u_1. \end{aligned} \quad (3-20)$$

The static thermodynamic quantities (static pressure, static temperature and density) remain the same after the transformation as they are internal properties of the gas and do not depend on the choice of coordinate system.

In our device, as well as in many practical applications the basic independent parameter is the pressure relation across the shock wave. The ratio of the pressures across the shock is used as a measure of the “strength” of the shock wave and all other parameters can be expressed as function of that ratio. Because of the amount of tedious algebra involved in deriving these relations, they will only be stated here as results. The primes on all the quantities used are dropped, as from now on we will only be interested in the stationary laboratory system and will not use the reference system of the shock wave.

The propagating speed of the shock wave is:

$$c_s = a_1 \sqrt{\frac{\gamma-1}{2\gamma} + \frac{\gamma+1}{2\gamma} \frac{p_1}{p_2}}. \quad (3-21)$$

The speed of the gas behind the shock wave is given by:

$$u_2 = \frac{a_1}{\gamma} \left(\frac{p_2}{p_1} - 1 \right) \sqrt{\frac{2\gamma/(\gamma+1)}{p_2/p_1 + (\gamma-1)/(\gamma+1)}}. \quad (3-22)$$

The densities and temperatures are related by:

$$\frac{\rho_2}{\rho_1} = \frac{1 + \frac{\gamma+1}{\gamma-1} \frac{p_2}{p_1}}{\frac{\gamma+1}{\gamma-1} + \frac{p_2}{p_1}}. \quad (3-23)$$

$$\frac{T_2}{T_1} = \frac{p_2}{p_1} \frac{1 + \frac{\gamma+1}{\gamma-1} \frac{p_2}{p_1}}{1 + \frac{\gamma+1}{\gamma-1} \frac{p_2}{p_1}}. \quad (3-24)$$

3.5 Expansion Waves

Let us imagine a one dimensional expansion wave traveling to the right inside a pipe. The wave can be created by suddenly withdrawing to the left a piston located at the left end of the pipe. The motion of the piston decreases the pressure of the gas to the right of it and forms a non-equilibrium pressure profile. The resulting expansion wave propagates away from the piston. We noticed in Section 3.3 that the expansion waves flatten out with time, and therefore (unlike in the case of the propagating compression wave) no discontinuities result. In order to derive the equations governing the propagation of expansion waves of finite amplitude, we have to take into account the local motion of the fluid because it can be comparable to the local speed of sound (just like in the case of compression waves we had to change the reference frame). Looking from a stationary reference frame, the wave speed at a point is:

$$c = a + u. \quad (3-25)$$

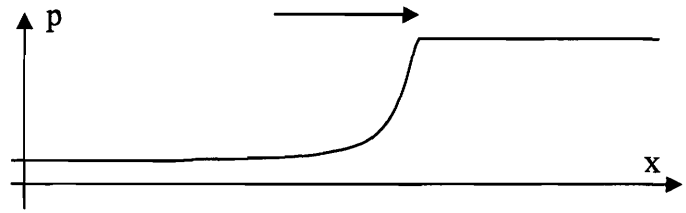
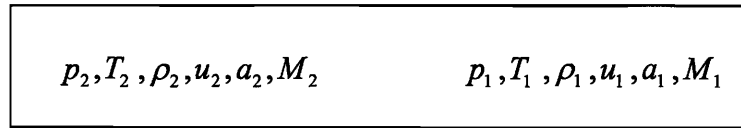


Figure 3-4: Propagation of an expansion wave along a pipe.

For a propagating wave of any amplitude the following relationship holds linking the changes of different thermodynamic parameters:

$$du = a(d\rho/\rho) = (a/\gamma)(dp/p). \tag{3-26}$$

Equation (3-2) substituted into (3-4) can help us express the local speed of sound only as a function of the pressure:

$$a = a_1 \left(\frac{p}{p_1} \right)^{(\gamma-1)/2\gamma}. \tag{3-27}$$

Substituting a from this equation into (3-26) and integrating it gives us:

$$u = \frac{2a_1}{\gamma-1} \left[\left(\frac{p}{p_1} \right)^{(\gamma-1)/2\gamma} - 1 \right]. \tag{3-28}$$

Rearranging this equation using (3-27) and substituting into (3-25) we obtain for the local speed of the wave:

$$c = a + \frac{\gamma+1}{2} u. \tag{3-29}$$

To determine the thermo-dynamical relation between the undisturbed fluid ahead of the wave and the fluid behind the expansion wave, we use (3-28) and the adiabatic pressure-density relationship:

$$\frac{p_2}{p_1} = \left(1 - \frac{\gamma - 1}{2} \frac{u_2}{a_1}\right)^{2\gamma/(\gamma-1)},$$

$$\frac{\rho_2}{\rho_1} = \left(1 - \frac{\gamma - 1}{2} \frac{u_2}{a_1}\right)^{2/(\gamma-1)}. \quad (3-30)$$

Where u_2 is the speed of the fluid behind the expansion wave, and a is the speed of sound in the undisturbed fluid.

3.6 Shock Tube

A shock tube is a device that generates a shock wave usually by rupturing a membrane separating a high pressure reservoir from a low pressure reservoir. A simple model will be presented here that quantifies the operation of the device and the characteristics of the shock wave generated.

The parameters for the initial state of the high pressure reservoir are denoted p_4, T_4, ρ_4, a_4 and those for the low-pressure reservoir- p_1, T_1, ρ_1, a_1 . After the rupture of the membrane an initial step-like pressure profile is created in the tube. If the rupturing process occurred instantly the profile would be a pure step. However in reality, as shown in Section 5.2.2, the membrane yields at a point, forms a crack and the crack propagates. Due to the non-zero time this process takes to occur and its irregularity, the initial pressure profile looks like the one in Figure 3-5b. The large pressure difference between the two parts of the flow, now free to move, creates two pressure waves propagating in opposite directions. An expansion wave starts traveling to the right into the high pressure gas, reducing its pressure, while a compression wave travels to the left into the low pressure gas, increasing its pressure. The imaginary boundary separating the two parts of the gas, which at time $t=0$ is at the position of the membrane, moves to the left behind the compression wave. It behaves as a solid wall in the sense that there is no flow across it; the two volumes of gas stay physically separated, as though the membrane is still there, but free to move. This boundary, together with the fronts of the compression and expansion waves divides the gas in four regions as shown in Figure 3-5c:

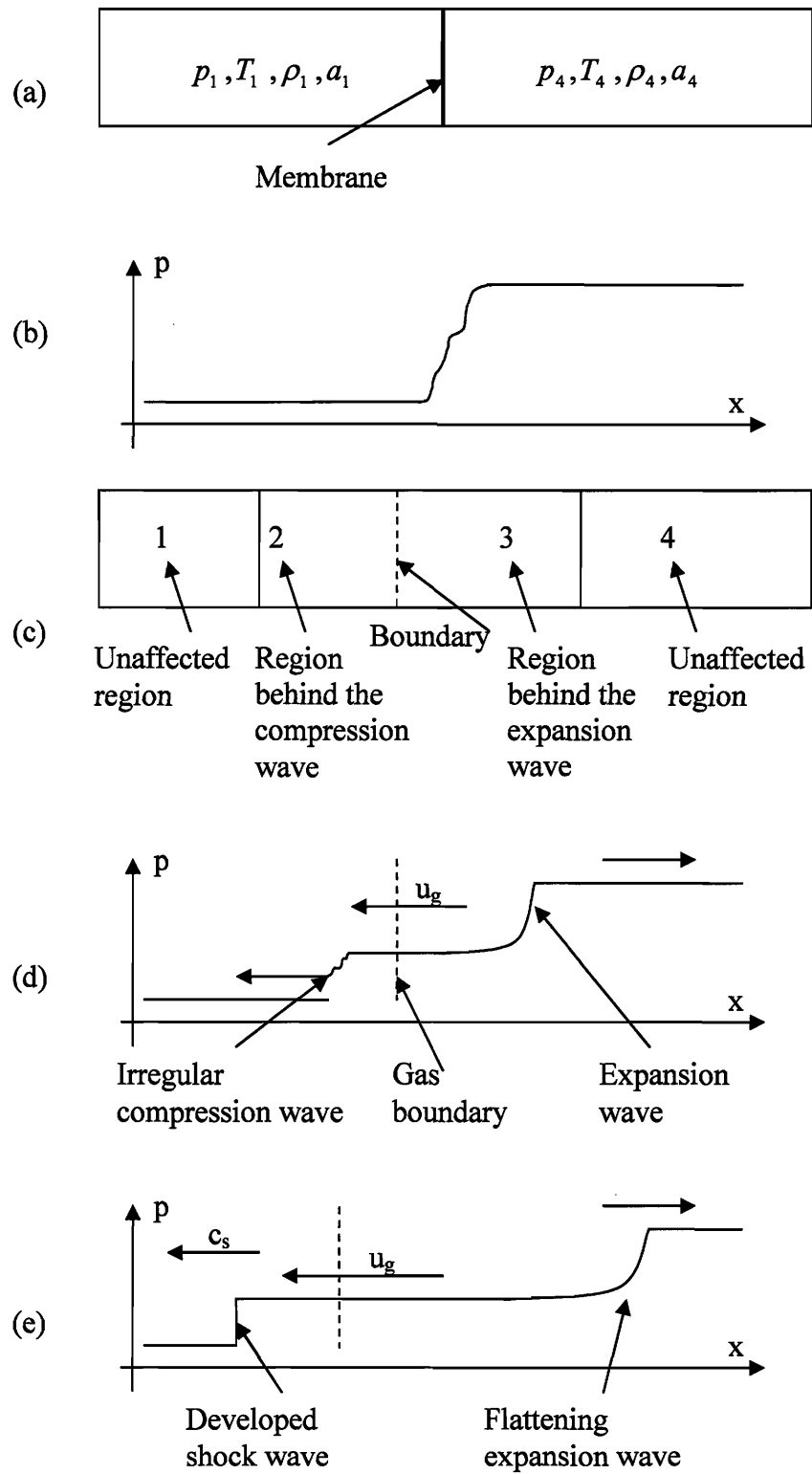


Figure 3-5: Operation of a shock tube

a) initial setup with a high- and low-pressure chamber b) regions in the gas c) initial step-like pressure profile c) propagating compression and expansion waves d) completely developed shock wave.

1. Region ahead of the front of the compression wave, unaffected by it.
2. Region between the compression wave front and the gas boundary
3. Region between the gas boundary and the expansion wave front
4. Region ahead of the front of the expansion wave, unaffected by it

The number of the region can be used as index of the variables describing the flow condition at the respective region. The “no flow across the boundary” condition for regions 2 and 3 requires that:

$$\begin{aligned} p_2 &= p_3, \\ u_2 &= u_3. \end{aligned} \quad (3-31)$$

We know from Chapter 3.3 that the expansion wave will flatten out and the compression wave will eventually develop into a shock wave, as shown in Figure 3-5e. So we can combine the relationships (3-22), linking pressure and velocity across the shock wave, and (3-30), linking pressure and velocity across the expansion wave, with the boundary conditions (3-31) to obtain:

$$\frac{p_4}{p_1} = \frac{p_2}{p_1} \left(1 - \frac{(\gamma_4 - 1)(a_1/a_4)(p_2/p_1 - 1)}{\sqrt{2\gamma_1}\sqrt{2\gamma_1 + (\gamma_1 + 1)(p_2/p_1 - 1)}} \right)^{-2\gamma_4/(\gamma_4 - 1)}. \quad (3-32)$$

This equation gives the initial pressure ratio before the membrane ruptures as a function of the pressure ratio across the shock wave. For practical purposes we need the inverse of this function, because p_4/p_1 is known. It is difficult if not impossible to give a close form expression for it, but a plot relating the two ratios is given in Figure 3-6 for two different cases:

1. High pressure gas is nitrogen at $T = 273$ K, low pressure gas is air at $T = 273$ K,
2. High pressure gas is water vapors at $T = 3000$ K, low pressure gas is air at $T = 273$ K.

For the second case γ is assumed to remain constant at high temperatures, which is a reasonable approximation.

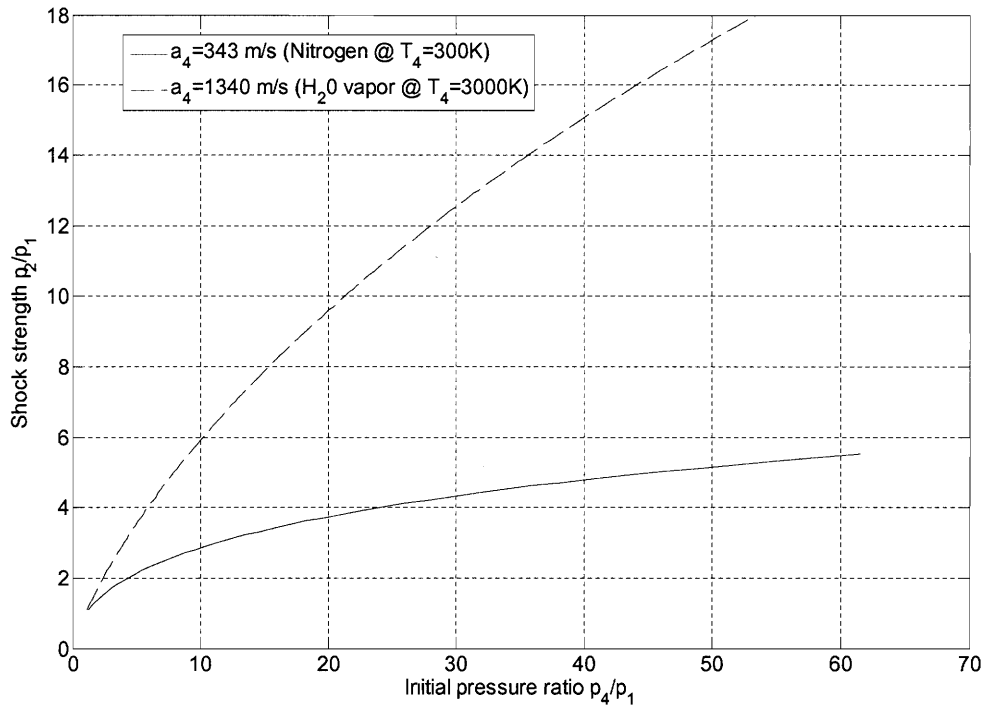


Figure 3-6: Shock wave strength versus initial pressure ratio at two different conditions.
In both cases the gas in the low pressure area is air at $p = 101$ kPa and $T = 300$ K.

Once p_2 is found, then using the shock wave relations given in Section 3.4.2 all the other parameters in region 2 can be found.

3.7 Shock wave formation distance

A simple estimation of the time and length necessary for the shock wave to develop can be made. Knowing the shock strength and the speed of sound in region 1, the shock speed c_s can be found. Combining (3-25) and (3-27) we obtain the propagation speed of the tail of the compression wave during the shock wave formation:

$$c_2 = a_1 \left(\frac{p_2}{p_1} \right)^{(\gamma_1 - 1)/2\gamma_1} + u_2, \quad (3-33)$$

where u_2 is the speed of the gas flow behind the shock wave obtained from Equation (3-22). If the time for rupturing the membrane is τ_{mem} , then the initial

spread of the compression wave is $c_s \tau_{mem}$, and the time it takes for the tail to catch up with the front of the shock is $c_s \tau_{mem} / (c_2 - c_s)$. Because the front shock propagates with speed c_s , then the distance traveled by the compression wave before it turns into shock wave is on the order of:

$$l_{formation} = \frac{c_s \tau_{mem}}{\frac{c_2}{c_s} - 1} \quad (3-34)$$

4

Experimental Setup

The first set of experiments performed aimed at studying the processes involved in the operation of the needle-free injection device powered by compressed gas and also at trying to improve the performance of the device. The goal was to achieve homogeneous particle flow at maximum possible speed, as well as achieve repeatability of the experiments. Nitrogen was chosen as a driving gas, in contrast to the helium used in the commercial devices. A diagram of the experimental setup is shown in Figure 4-1.

The nitrogen tank supplied pressurized gas and a pressure regulator attached to it reduced the pressure to the desired value. The output of the regulator was connected to a solenoid valve used to actuate the device. Once the valve was opened, the rupture chamber accumulated gas until the threshold pressure of the first membrane (the chamber membrane) was reached. A high bandwidth pressure transducer (Section 4.3), mounted on the chamber, provided readings for the internal pressure. After the chamber membrane ruptured, a rapid compression wave was released into the shock tube. During its propagation, it converted into a shock wave with extremely sharp wave front. This shock wave passed the second pressure transducer, struck the second membrane (the drug membrane) and rapidly accelerated the membrane and the drug. The object of interest for the given experiment (the membrane, the powder etc.) was imaged by the high speed camera (Section 4.4), which was triggered by the same button that opened the valve. The pressure measurements, taken by the sensors, were recorded by a digital oscilloscope, and then sent to a computer for analysis, together with the images taken from the camera.

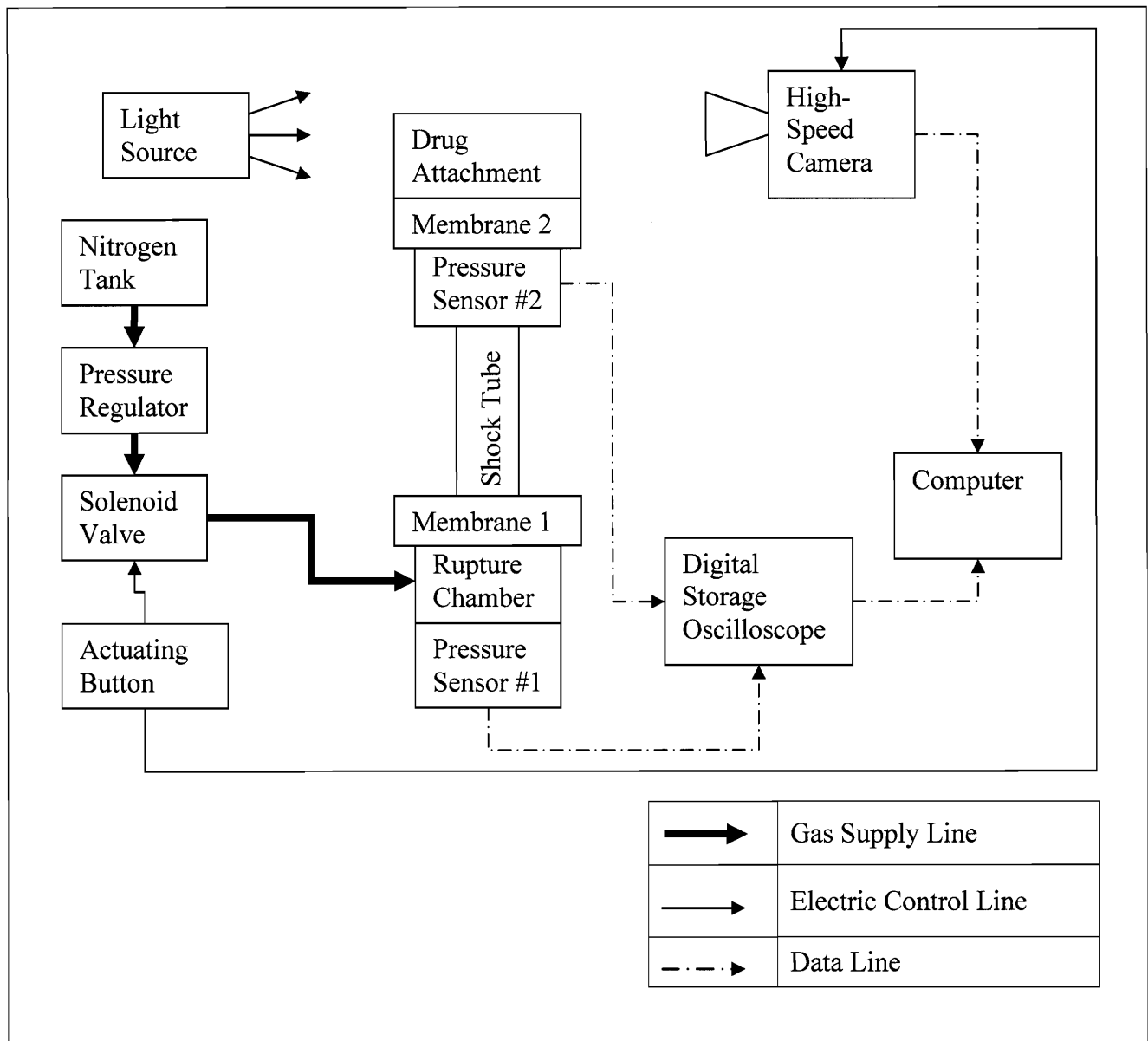


Figure 4-1: Experimental setup for studying the operation the needle-free injector powered by compressed nitrogen

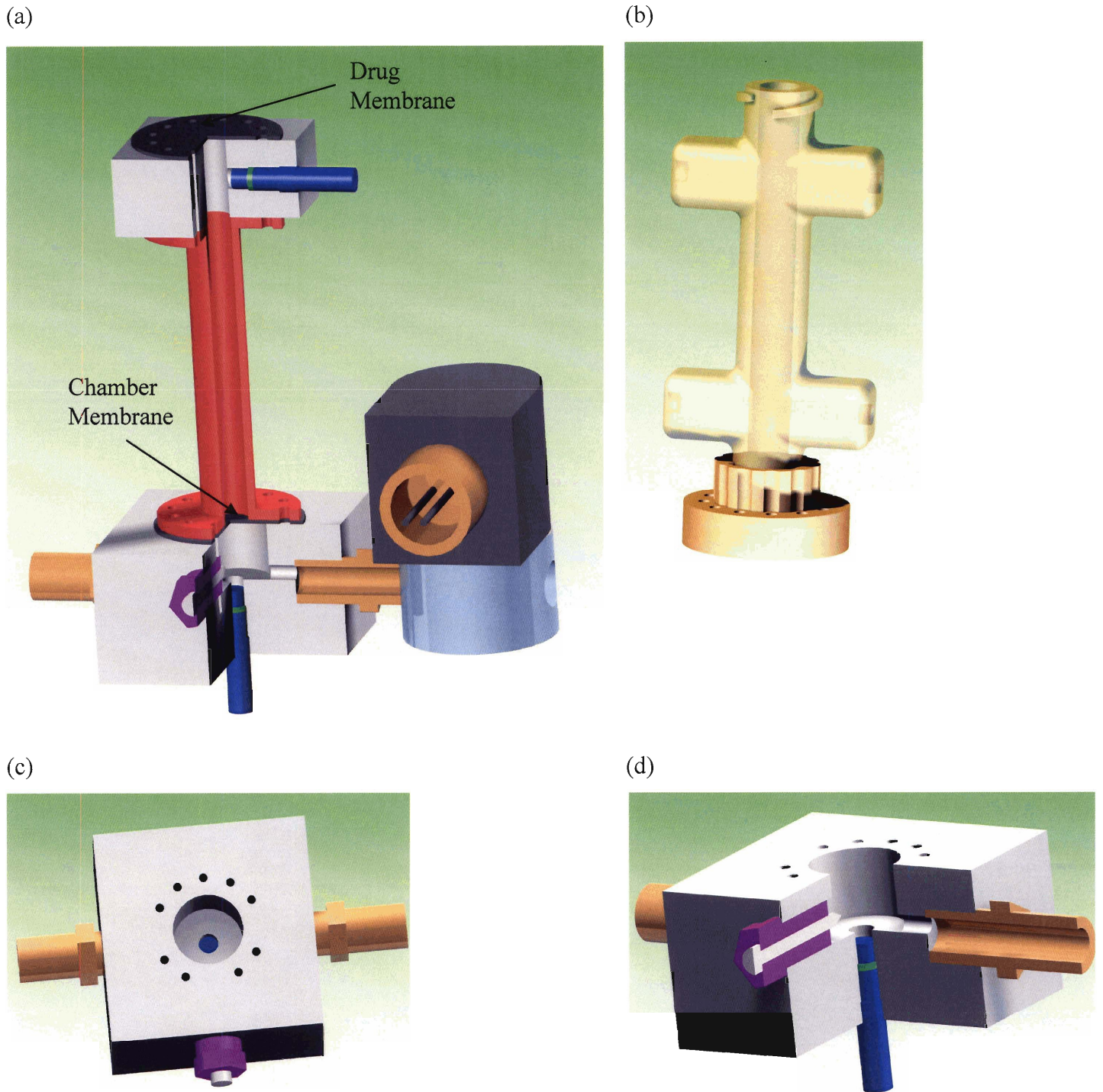


Figure 4-2: Rupture chamber and shock tube models

a) overall cutaway view of the setup b) alternative translucent plastic barrel c) top view of the rupture chamber d) close-up on a cutaway view of the chamber

4.1 The rupture/combustion chamber and the shock tube

The rupture chamber was designed so that it could be reused later in the hydrogen-oxygen combustion experiments. It was machined as a cylindrical cavity 20 mm in diameter and 15 mm deep in a block of aluminum, and had a volume of 4700 mm³.

Check valves were mounted on both inlets and a spark-plug was mounted on the front part of the chamber. The body of the spark plug had to be made of dielectric material, so we used polyimide (plastic with superior mechanical properties). The first pressure sensor was mounted on the bottom of the chamber, and RTV coating was applied on it to provide protection from the high-temperature gases. Although the device never ran in continuous mode, without coating, the temperature at the surface of the transducer got so high, that it returned completely incorrect readings. A set of 9 bolts provided the link between the chamber and the shock tube (the “barrel”). Fewer holes would not provide a sufficiently even spread of the contact pressure and would cause leakage of gas from the chamber. A gasket, below and above the chamber membrane improved the sealing further. The membranes and the gaskets were cut using a Trotec laser cutter and engraver.

One of two different barrels was used in the experiments, both having internal diameter of 10 mm. An aluminum barrel was used for injections and pressure tests, while a plastic, optically translucent barrel was used in some velocity measurements involving hot luminescent gases. The aluminum barrel was machined on a Mazak turning/milling center, while the plastic barrel was made of UV curing resin on a Viper Stereolithographic Apparatus (SLA). Although not optically clear, it was translucent enough to enable the propagating glowing hot gases to be visualized from the sides. A separate attachment was made on the SLA for this barrel, providing quick and easy membrane replacement between experiments.

When the aluminum barrel was used, an adapter for a second pressure sensor was attached to the other end of it onto which the drug membrane was affixed. The second transducer, mounted sideways, was used to provide a measure of the strength of the shock

wave, and together with the combustion chamber sensor, to measure the propagation speed of the wave.

4.2 Gas flow control

The Nitrogen tank supplied compressed gas at 14 MPa when full. The pressure regulator attached to the tank could be adjusted for output pressures in the full range 0 to 14 MPa. The valve used to turn the flow on and off was a Parker high speed 800 μm orifice solenoid valve rated for 17 MPa and powered by 24 V DC.

4.3 Pressure sensors

All the pressure measurements were performed using 211B1 pressure transducers from Kistler. These sensors were chosen for their fast response and miniature size. The 211B1 has natural frequency of 500 kHz and a rise time of 1 μs for pressures in the range 0 to 70 MPa. The transducer has a diameter of 6mm and length of 33 mm, which allowed it to be mounted in relatively tight space. The sensor is acceleration-compensated and the first stage of the signal amplifier is mounted inside the sensor, which reduces the noise level in the signal. A disadvantage of the sensor was that it could only measure dynamic pressure and had a finite time constant, which did not allow us to use it as an indicator of the static pressure inside the chamber. However this was not a major problem and whenever needed, we either used a mechanical gauge as an alternative, or performed differential measurements over short time intervals. The sensors were calibrated in the pressure range 100 kPa to 600 kPa and showed linear behavior with a sensitivity of 81×10^{-9} V/Pa.

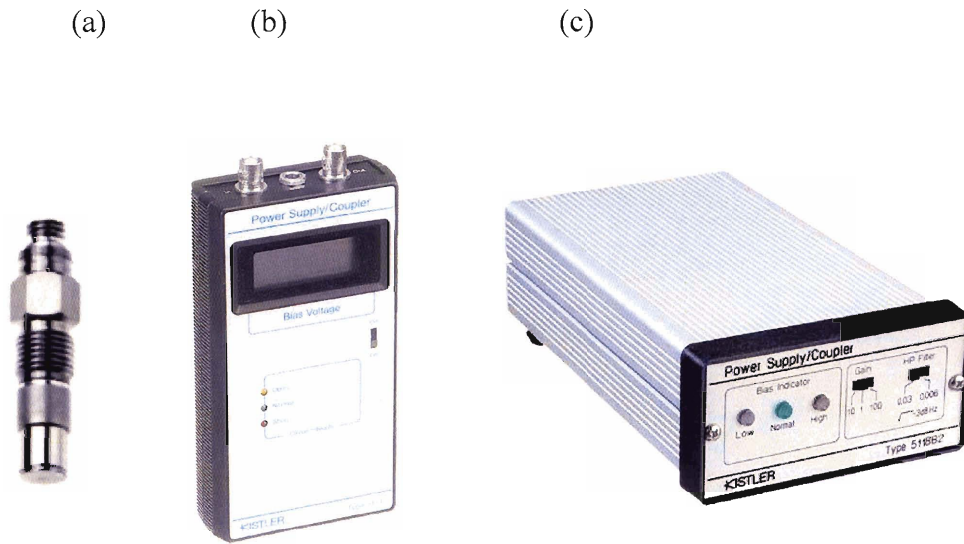


Figure 4-3: Pressure transducer and couplers (a) Kistler 211B2 pressure transducer (b) 5114 coupler and power supply (c) 5118B2 coupler and power supply.

4.4 High speed camera

The fast transient processes taking place during the operation of the device required a very fast camera. A Phantom v9.0 high speed camera from Vision Research Inc. [25] was used. The camera is state-of-the-art with a 1600×1200 color 10-bit SR-CMOS photosensitive array. At full resolution the camera was able to achieve 1000 frames per second (fps); however we needed much higher speed than that so we ran it at resolution of 192×96 and below, achieving frame rates up to 50,000 fps. The camera recorded each film (cine) in an internal memory and then it was downloaded via an Ethernet cable to a computer. An external triggering input was provided and was used to synchronize data acquisition in the majority of the experiments.

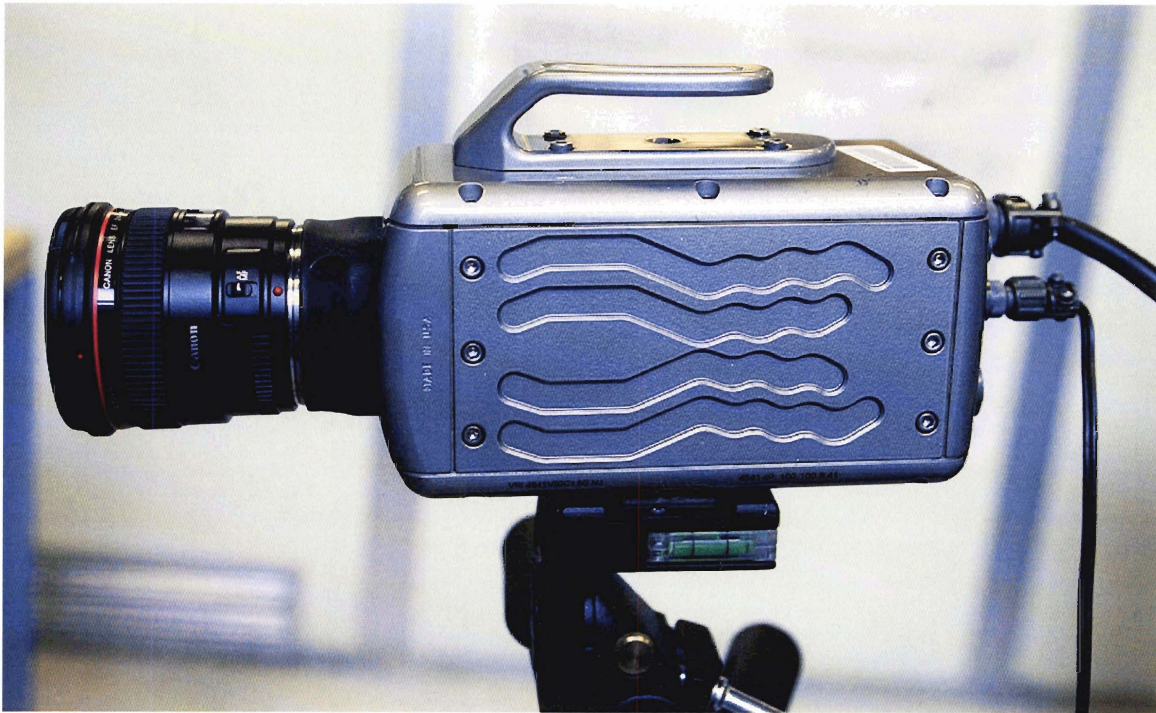


Figure 4-4: Phantom high-speed camera.

4.5 Optical setup

The high speed camera required very high light intensity over a small field of view. A xenon lamp provided illumination for the setup via a bundle of optical fibers. The speed of the particles was measured in transmission as shown in Figure 4-5. In this case a cylindrical lens was used to produce an elliptical light beam, with the major axis parallel to the velocity of the particles and the shadows of the particles were recorded by the camera.

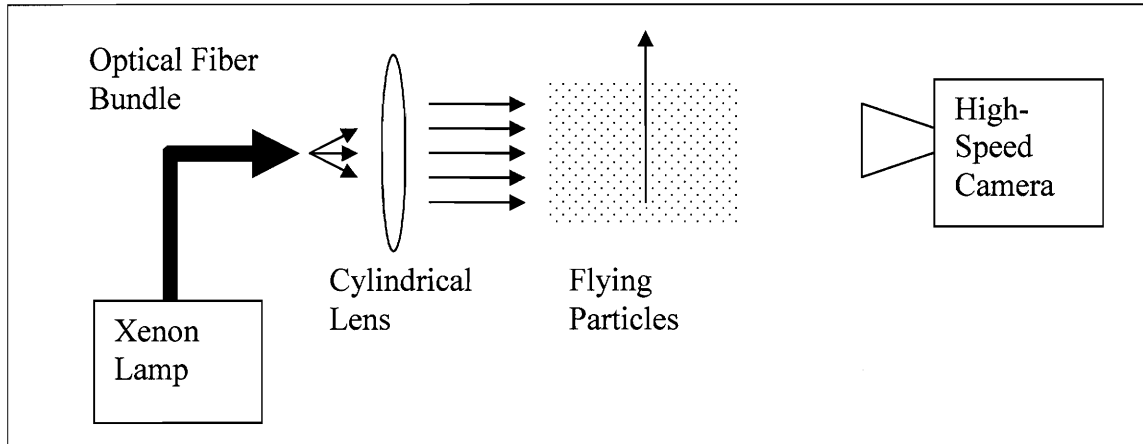


Figure 4-5: Optical setup for transmission measurements of velocity.

4.6 Oscilloscope

The readings from the pressure sensor were displayed and recorded using a Tektronix series 2000 Digital Storage Oscilloscope. The scope had two channels with a bandwidth of 200 MHz and maximum sample rate of 2 GS/s, although in the pressure measurements only sample rates of up to 5 MS/s were used. In most experiments it was run in a single acquisition mode, in which upon detecting of a triggering event, it collected and recorded 10,000 sample points at the current sampling rate. The scope was triggered by the voltage of the input channels and had the feature allowing it to record certain number of samples preceding the triggering event. The oscilloscope ran a HTTP web server, allowing easy data download through a web-based interface.

4.7 Lexan Enclosure

In order to ensure the safety of the people and devices working in the lab, we designed and built a “bulletproof” enclosure for the experimental setup. The supporting structure was built out of MK System 40 mm profiles. The side panels were made of 25 mm thick abrasion resistant Lexan, consisting of highly-durable polycarbonate core, laminated between two scratch resistant PMMA sheets on each side. The polycarbonate

provided high toughness and rigidity, while the PMMA provided the optical clarity necessary for filming the experiments with the high speed video camera.

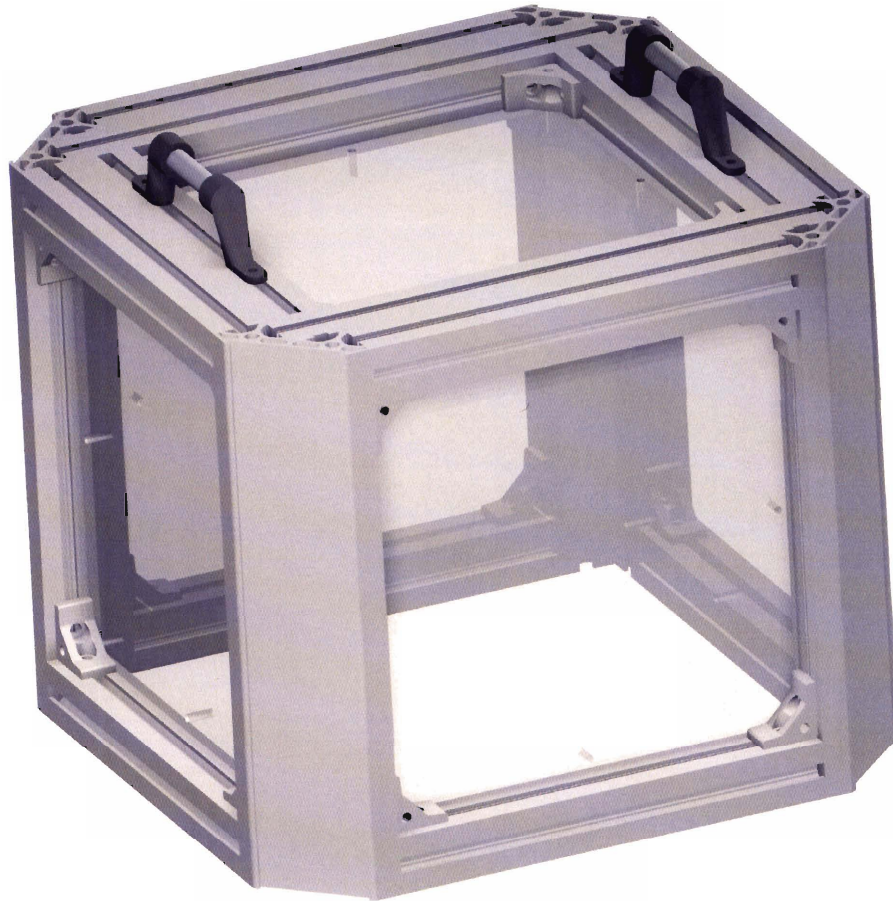


Figure 4-6: Lexan "bulletproof" enclosure.

The completely assembled setup positioned in the Lexan enclosure is shown in Figure 4-7

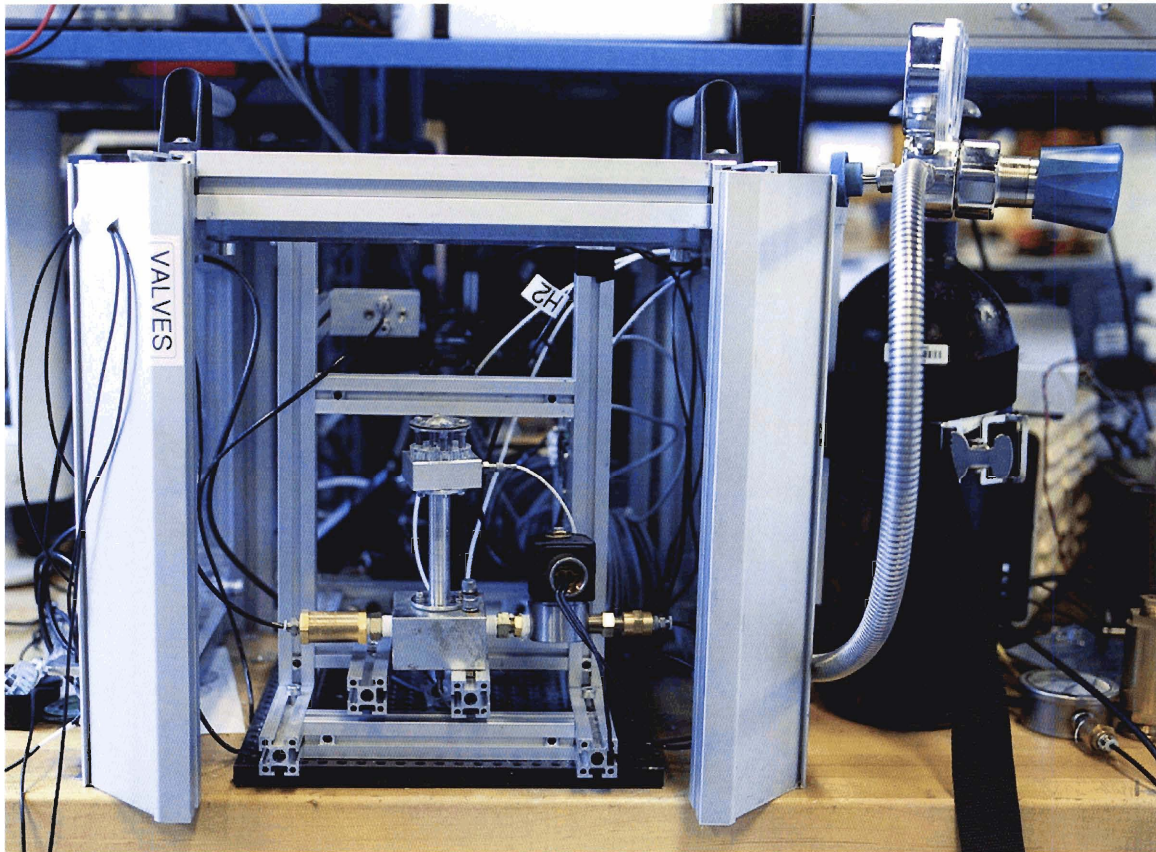


Figure 4-7: Completed device setup.

5 Experiments with Compressed Nitrogen

5.1 Overview

Several experiments were performed using the compressed nitrogen powered device. In the first set of experiments, the process of rupturing the chamber membrane was studied in order to determine its effect on shock wave formation. Next, the behavior of the shock wave itself was examined together with the way it impacted the drug membrane. A set of experiments looked at the eversion process of a concave membrane, similar to the one used in the original PowderJect device. A few alternative designs for the membrane were tested, and the one that proved most successful was used for injection tests.

In all the experiments the rupture membrane was made of polyester foil (Mylar). Three different thicknesses were used- 25 μm , 50 μm , and 100 μm . Polyester and polyurethane were tested as materials for the drug membrane.

5.2 Membrane rupture

These experiments were performed with the barrel removed. The rupture membrane sealed the rupture chamber, pressed in place by an aluminum ring-shaped holder, with an internal diameter of 20 mm (equal to the diameter of the chamber). During the membrane rupturing process, pressure measurements, indicating chamber pressure, and high-speed images of the deformation and rupture of the membrane were recorded. The clear polyester material was coated with a layer of white paint, so that it was easily imaged.

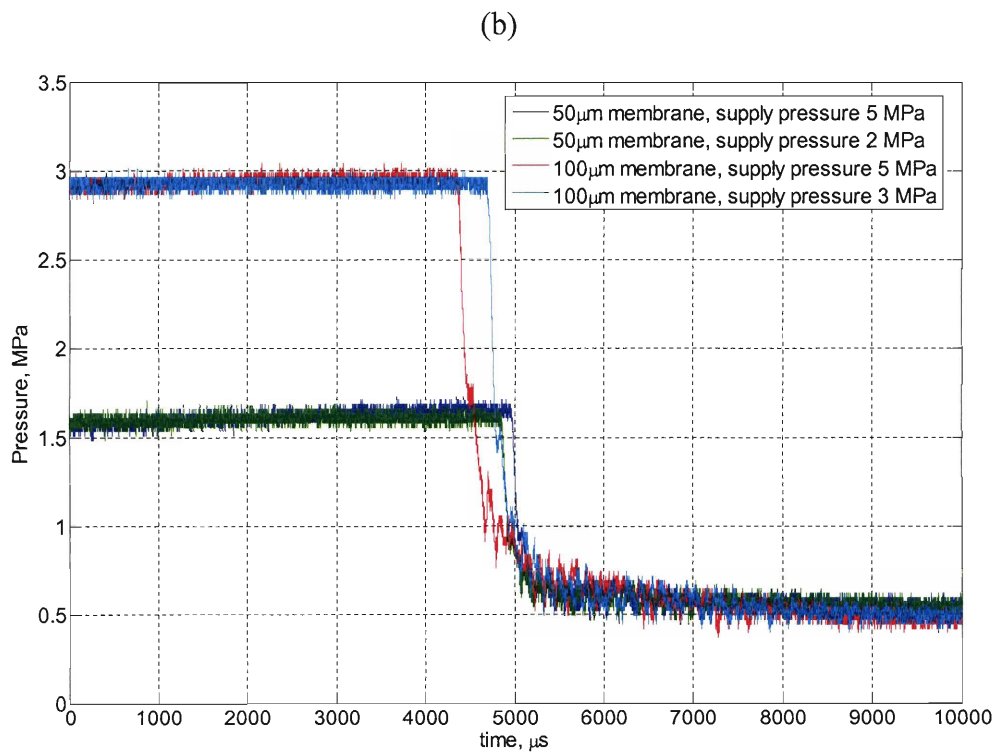
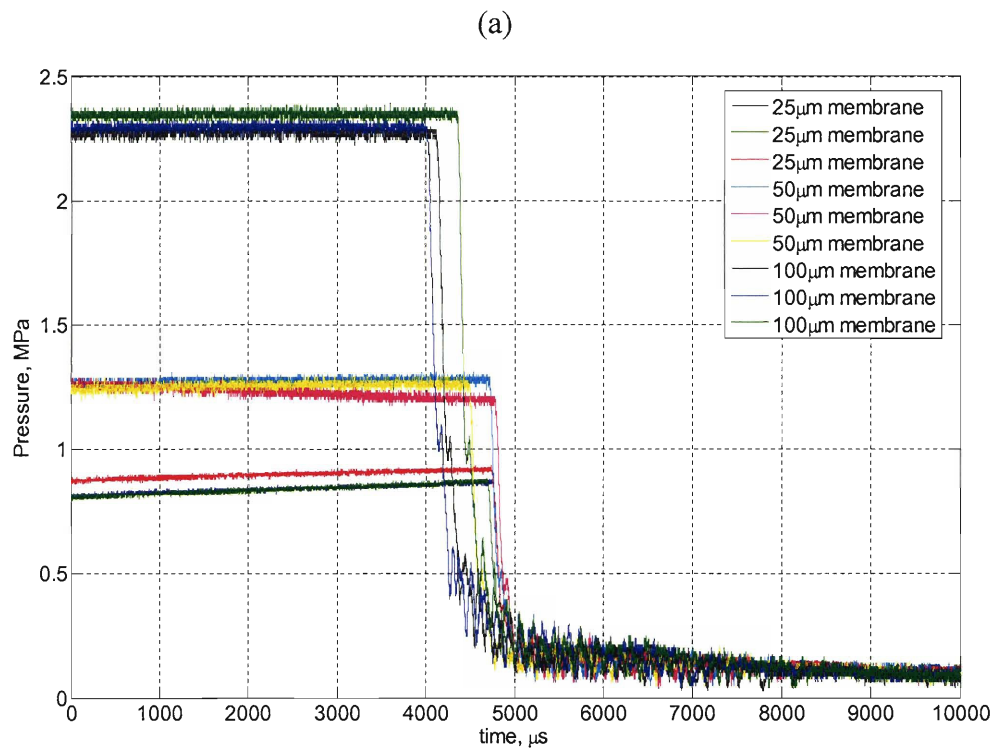


Figure 5-1: Pressure measurements of the chamber pressure demonstrating (a) repeatability of rupture pressure (b) independence of supply pressure.

5.2.1 Rupture Pressure

First, we decided to determine repeatability and dependence of rupture pressure on membrane thickness. All the available membrane thicknesses were used, and for each thickness the experiment was run three times. The results indicated in Figure 5-1a and in Table 5-1 demonstrate repeatability within 7% for a given membrane thickness. The rupture pressure shows linear increase with membrane thickness with a rate of 2×10^{10} Pa/m.

The second experiment aimed at determining whether the supply pressure had any effect on the pressure at which the membrane ruptures. Two different membrane thicknesses were used- 50 μm , and 100 μm and two different pressures were used for each thickness. The experimental data in Figure 5-1b shows, that varying the supply pressure has little or no effect on the resulting maximum pressure in the chamber.

Membrane thickness, μm	Mean achieved pressure, MPa	Standard deviation, MPa	Pressure fall time, μs
25	0.86	0.04	270
50	1.24	0.04	270
100	2.32	0.03	260

Table 5-1: Summary of measurement results from the rupture tests.

5.2.2 Membrane Dynamics

The first series of experiments in Section 5.2.1 was filmed using the high speed camera at frame rate of 26,316 fps and exposure time of 17 μs . For each measurement four consecutive frames were extracted and listed in Figure 5-2. It can be seen that the process is very similar for a given thickness and that the change of thickness of the membrane does not have a significant effect on the duration of the process. For every membrane it took about 40 μs to open halfway and about 70 μs to open completely.

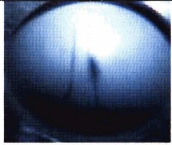








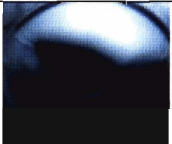
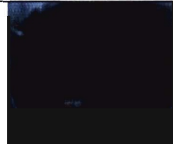
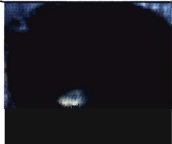



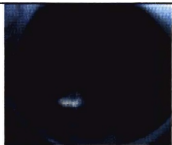

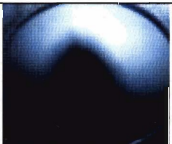


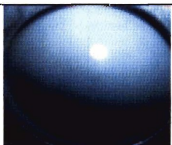
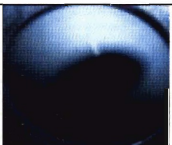

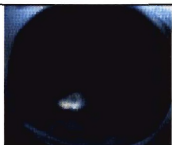

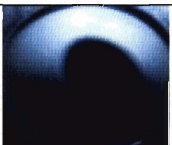


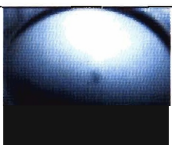

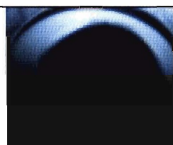
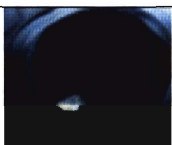




Membrane thickness	0 μ s	38 μ s	76 μ s	114 μ s
25 μ m				
25 μ m				
25 μ m				
50 μ m				
50 μ m				
50 μ m				
100 μ m				
100 μ m				
100 μ m				

Figure 5-2: Rupturing process for different membranes.

5.3 Shock wave generation

In these experiments measurements were taken of the chamber pressure and the pressure at the end of the shock tube in the short interval following the chamber membrane rupture. Two parameters were varied: the barrel-end conditions, and the thickness of the chamber membrane. The membrane thickness determined the maximum achieved pressure in the chamber before the membrane ruptured and therefore the strength of the shock wave.

5.3.1 Pressure Equilibration

Figure 5-3a shows the time variation of the two pressures with a closed downstream end of the shock tube. The tube was sealed using a PMMA cap. The chamber pressure reached a maximum and started falling, as the expansion wave propagates in the chamber. Shortly afterwards the pressure on the other end of the shock tube rapidly increased indicating the arrival of the shock wave. Due to the static boundary conditions at the end of the barrel, the pressure reached value close to that of the original chamber pressure, but slightly lower, due to shock wave losses. The shock wave was reflected back and propagated upstream the tube. Similarly the expansion wave was reflected off the bottom of the rupture chamber and started propagating in opposite direction. As both waves propagated at different speeds and kept changing their speed as the pressures equilibrated, oscillations with irregular shapes resulted. Cross correlation of the two signals is also shown in the figure, and it exhibits oscillation with period of about 330 μs . We did not attempt to model this behavior due to the complicated phenomena involved in the interaction of shock waves with expansion waves and boundaries and because we were primarily concerned with the initial transient phenomena up until the initial pressure peak at the downstream location.

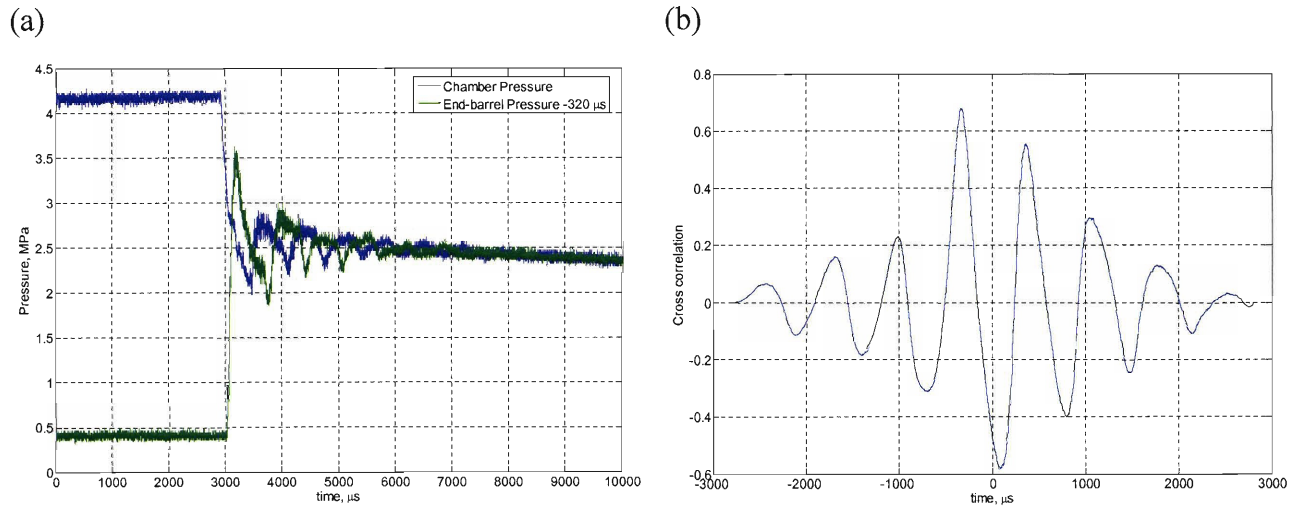


Figure 5-3: Pressure equilibration after membrane rupture
a) measured data b) cross correlation of the two signals.

5.3.2 Shock tube under different conditions

In order to get a better understanding of the initial transient phenomena, the measurements in the previous section were repeated with the downstream end of the shock tube open and with a 25 μm membrane attached to it. The results, for the first 300 μs after the “explosion” of the membrane are shown in Figure 5-4. At first they looked surprising, because the initial shock wave traveled faster than the speed of sound and did not “know” about the existence of membrane or cap at the end of the tube. Therefore the shock wave had to look exactly the same in all three experiments, but the only common part of the three graphs was the region between the points A and B. It represented a rapid but small increase in pressure. Remembering Figure 3-6, we realized that this indeed was what we had to see. The pressure rise due to the shock wave was a small fraction of the initial pressure difference across the chamber membrane. The gas behind the shock wave was moving at very high speeds and therefore had a relatively low static pressure, which is the pressure we measured. The plateau B-C then must represent the time in which the shock wave travels to the end of the barrel and is reflected back. In the case of open barrel there is no reflection and the pressure remains constant thereafter. In the case of closed barrel, the reflected shock wave, with much higher amplitude than the initial one, propagates upstream and causes a secondary pressure rise. Finally in the

case of membrane closing the end of the barrel, we have a partial reflection of the shock wave, before the pressure behind the membrane rises enough to rupture it.

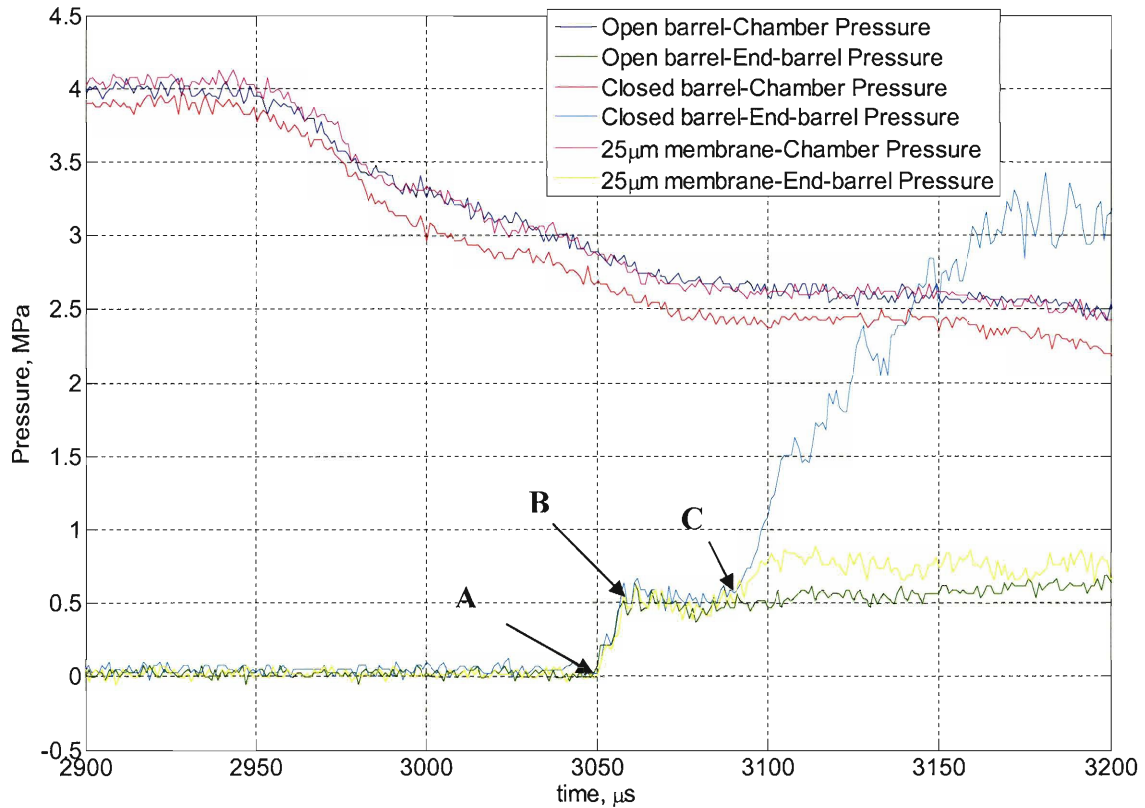


Figure 5-4: Shock wave behavior at different downstream end conditions of the shock tube.

5.3.3 Shock strength and speed variations.

A series of experiments were carried out to test the calculations of the shock wave velocity as a function of the initial pressure ratio. The results are summarized in Table 5-2, Figure 5-5 and Figure 5-6. P_4 represents the high pressure in the rupture chamber just before the membrane breaks, P_1 is atmospheric pressure and P_2 is the pressure behind the shock wave. The rupture of the membrane is detected by the onset of the chamber pressure decrease. The finite amount of time necessary for the expansion wave to reach the pressure sensor at the bottom of the rupture chamber is taken into account and is estimated to be 45 μs . We observe reasonable quantitative agreement. The measured shock speed is about 11% lower than the calculated speed, and the measured pressures are approximately 40% higher than the calculated pressures, which strongly suggests viscous losses inside the shock tube. The initial spread of the compression wave before it turns into a shock wave might also affect the measurements.

Membrane Thickness (μm)	P_4	P_4/P_1	P_2/P_1 measured	P_2/P_1 calculated	Measured shock speed, m/s	Calculated shock speed, m/s	Measured relative delay, μs	Calculated relative delay, μs
25	1.3	13	4.5	3.2	533	590	0	0
50	2.1	21	5.7	3.7	570	630	15	10
100	3.9	39	5.8	4.7	630	710	25	25

Table 5-2: Summary of the results comparing calculations and experimental results.

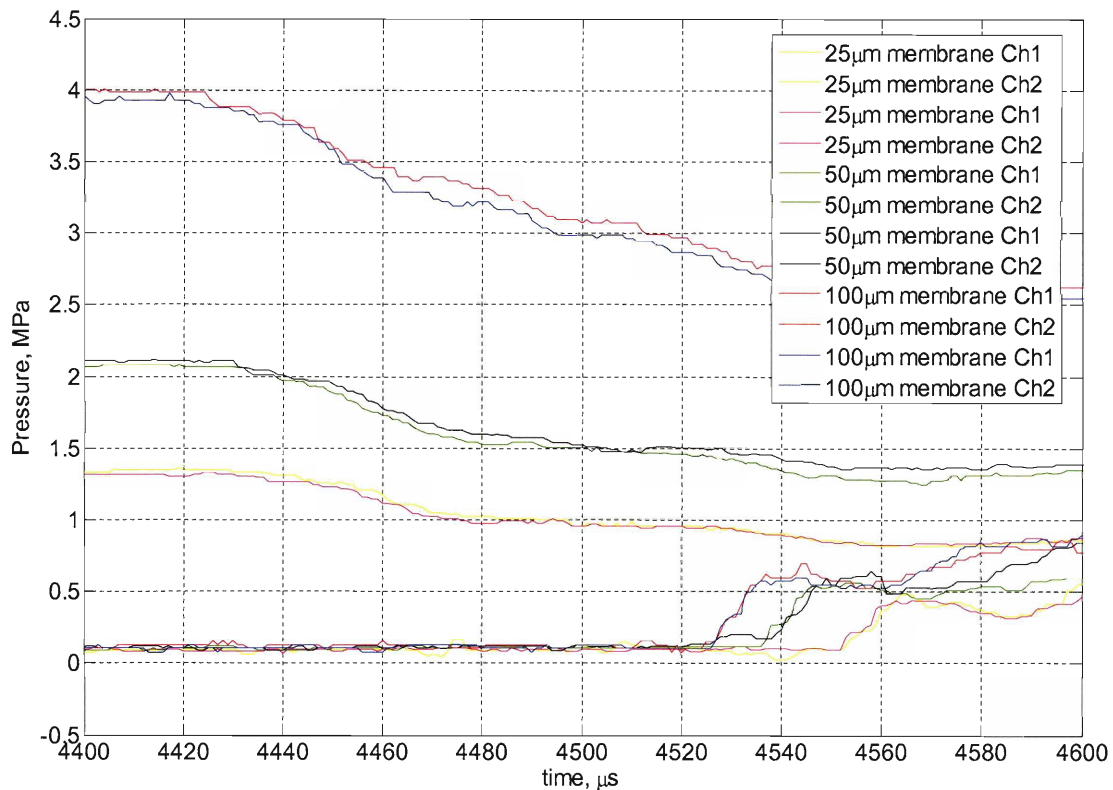


Figure 5-5: Shock wave propagation at different membrane thicknesses/ shock wave strengths.

The time required for the pressure to rise from atmospheric to the full pressure behind the shock wave for the case of 100 μm membrane is 10 μs measured from the graph. The major reason for this is the non-zero width of the pressure sensor. The diameter of the pressure sensor (6mm), divided by the shock speed gives an estimate of about 9 μs contribution to the rise time. Therefore the rise time of the shock wave is on the order or less than 1 μs and our assumption for developed shock wave at the end of the channel is confirmed by the experiment.

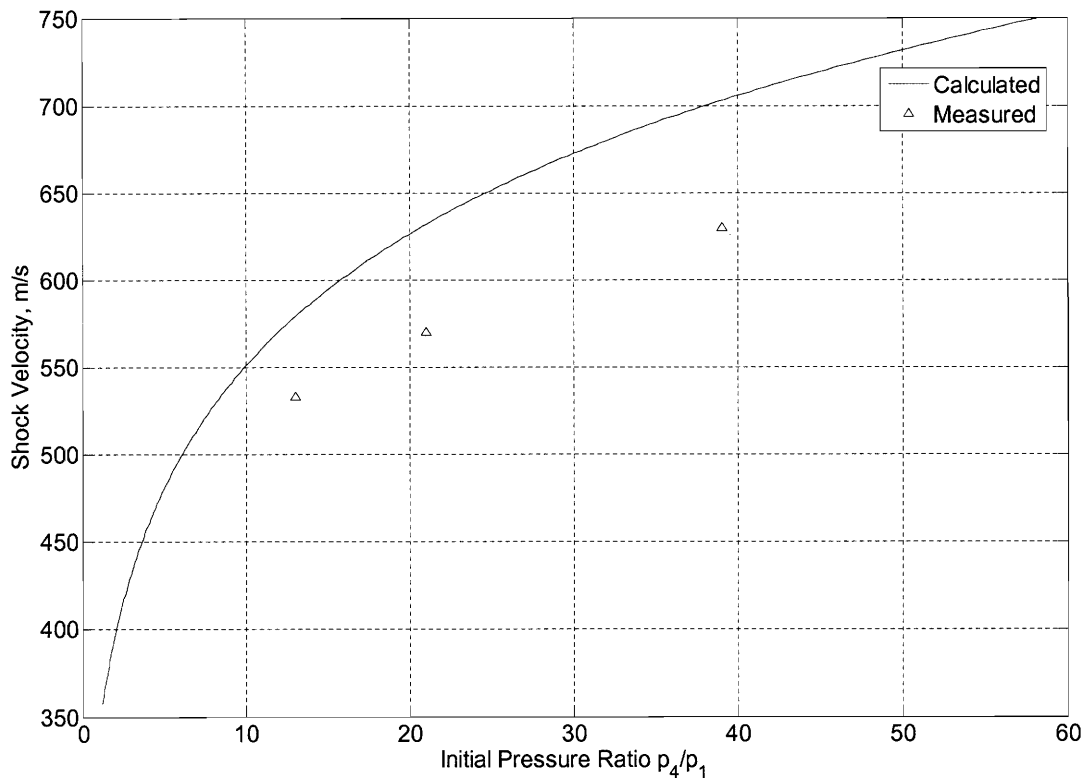


Figure 5-6: Comparison between theoretical predictions and experimental measurements for the shock wave speed.

Going back to Figure 5-4, the width of the plateau B-C, representing the time interval between the initial shock wave and the reflected shock wave reaching the pressure transducer is measured to be 30 μs . Calculations for the initial and the reflected shock wave predict a value of 40 μs for that interval, showing again reasonable agreement.

5.4 Injection experiments with eversible membrane

Having characterized the shock wave, we decided to go ahead and attempt to accelerate particles similar to the particles used in some of the commercial powder formulation. The first step, however, was to produce the concave eversible drug membrane. Initially we planned on cutting the membranes to shape out of 400 μm thick polyurethane sheet and thermoform them. The process produced good quality membranes of the desired shape; however experiments with everting these membranes yielded very unsatisfactory results. We decided to change to using 25 μm polyester which was lighter,

tougher and easier to evert than polyurethane. But the thermoforming process was inappropriate for this material, so we took another approach. Having cut the membrane to the correct shape, we attached it to the top of the rupture chamber, and increased the gas pressure until the desired deformed shape was achieved.

We used tungsten powder instead of gold because it had virtually the same density as gold ($19.25 \times 10^3 \text{ kg/m}^3$ vs. $19.3 \times 10^3 \text{ kg/m}^3$ for gold) and was less expensive. The powder used had a particle size in the range 1 to 5 μm , and an amount of 10 mg per test was used in these initial tests. A set of experiments, using the three different membrane thicknesses available (25, 50 and 100 μm) was conducted in an attempt to correlate the ejection velocity with the shock wave strength. A representative example of the filmed results with powder traveling to the right is shown in Figure 5-7, using 100 μm membrane. Unfortunately, the different parts of the particle cloud had very different velocities and the overall behavior of the cloud was very unpredictable. No clear front, that could be an indicator of the particle speed, was observed. Therefore the uncertainty in the velocity measurements was very high, and all we could conclude was that perhaps the speed was in the range 50 to 200 m/s.

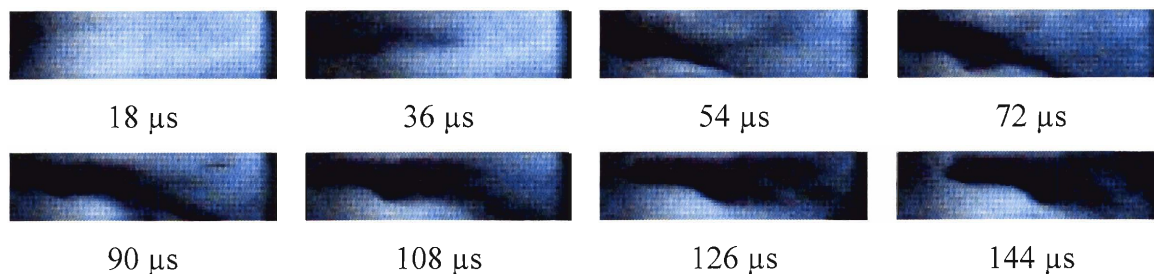


Figure 5-7: Tungsten particles ejected from the drug membrane.

5.5 Eversion of the drug membrane

The inconclusive results from the injection studies in Section 5.4 lead us to question the efficiency of the injection method using an eversible membrane. Because the eversion process occurred too quickly in a regular experiment to be filmed and analyzed, we used an experiment involving much slower processes. The membrane of the rupture chamber was replaced by a 25 μm concave polyester membrane which would flip

outwards when the pressure in the chamber increased after opening the solenoid valve. Filling the chamber required much longer time than the impact time of the shock wave with the membrane, and therefore the following events could be filmed with the high speed camera. The result of one of these experiments is shown below. The interval between the frames is $600\ \mu\text{s}$ and the whole process took about 14 ms. The process was very spatially irregular, chaotic and non-repeatable because the membrane passes through a range of unstable equilibrium states. It does not deform uniformly, but rather a 2-dimensional wave-like pattern, appears and develops with time in a very complicated way. The only theoretical treatment of membrane buckling dynamics that we could find in the literature [26, 27] described this phenomenon as stochastic and developing “a wavelike pattern in two dimensions with a wavelength that grows, via a coarsening process, as a power of time”.

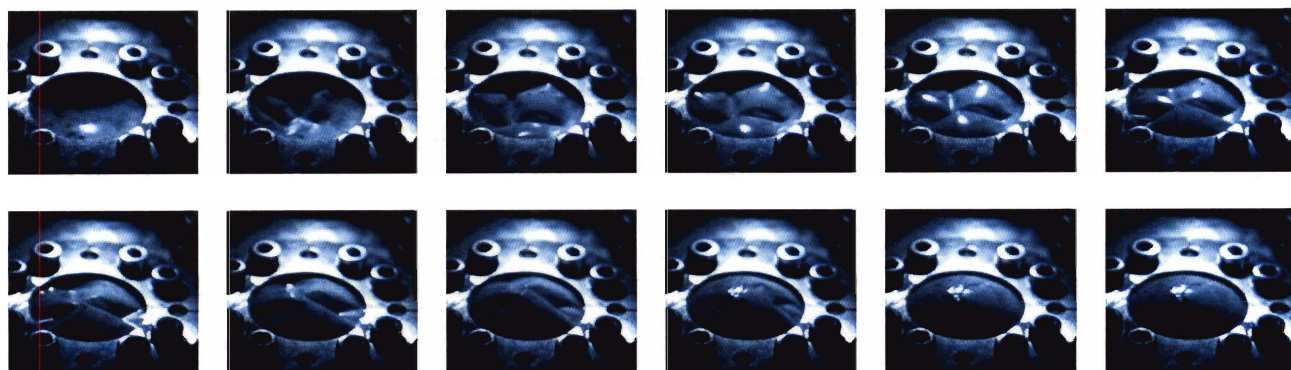


Figure 5-8: Series of frames showing the process of everting the drug membrane.

This led us to conclude that using an everting membrane does not provide enough accuracy and consistency and most likely is the factor responsible for the nearly chaotic trajectories of the tungsten particles observed in the experiments, as well as the low and inconsistent velocity measurements. Furthermore, remembering that work is defined as the product of force and distance, and that the force on the membrane was set by the pressure levels of the shock wave, the very short travel of the membrane ($\sim 5\ \text{mm}$ at best) was another factor for the low efficiency of the device and the resulting low velocities. Therefore an alternative method was needed for imparting motion to the drug particles.

5.6 Alternative designs for the drug membrane

We designed to alter the experiment to give the membrane enough travel distance to gain sufficient speed. Initially we decided to go to the extreme of simply leaving the membrane completely detached, lying freely on the end of the shock tube. In the same time we used small amount of ethyl alcohol to spread the tungsten powder in a thin and even layer over the surface of the membrane. Two experiments using this layout are shown in Figure 5-9. We can clearly see that the speed of the particles is much more homogeneous and the particle cloud retains its shape. However, we can also see that the membrane is unstable and spins sideways. The net torque on the membrane attempts to align its plane with the gas velocity direction in order to minimize flow resistance.

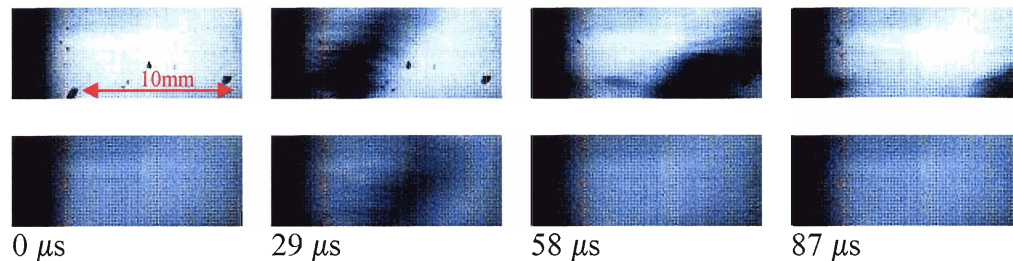


Figure 5-9: Experiments firing.

A head attachment, designed to constrain and stabilize the membrane is shown in Figure 5-10a and b. A set of six pins was placed around the exit of the shock tube, and the membrane was guided on these pins while traveling ahead. They allowed it to freely move parallel to the flow, but significantly restricted motion in any other direction, including spin. A very fine metal mesh was placed at the end of the membrane travel and prevented the membrane and the gases from impacting the tissue to be injected. As Figure 5-10 shows, although there is a deformation of the membrane, the guides have a definite stabilizing effect, and no sideways or spinning motion is observed.

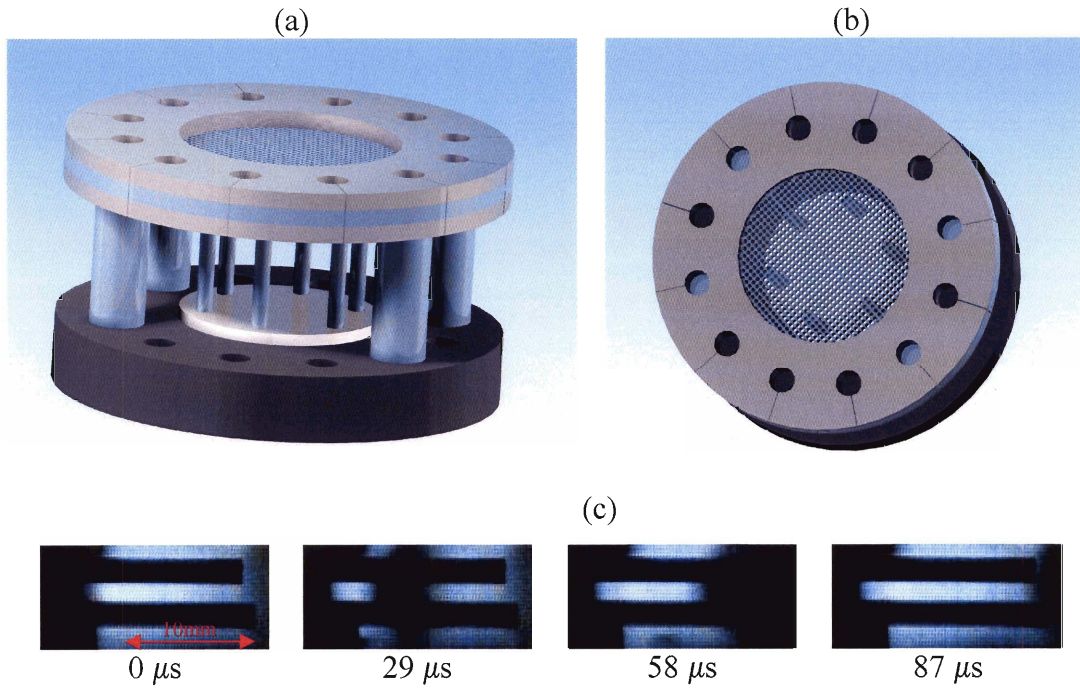


Figure 5-10: (a, b) Head attachment for the injection device (c) stabilized membrane traveling on the pins.

Tests using 3 to 4 mg of tungsten powder were performed in order to test the efficiency of the head attachment. The available membrane travel was 14 mm and the space above the mesh was filmed at 50,000 fps. The measurements from Figure 5-11 show a clear particle front, allowing us to perform velocity measurements with much greater accuracy. The result was 275 m/s and in these two sets of measurements was very repeatable.

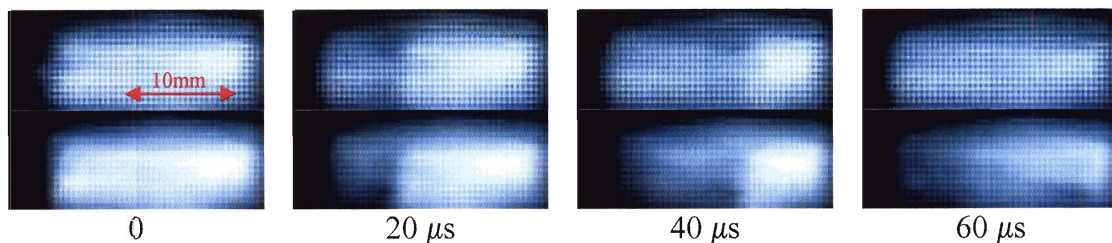


Figure 5-11: Tungsten particles cloud created with the device and the head attachment.

5.7 Injections into tissue

Three injections into post-mortem lamb skin were performed using a 25 μm eversible polyester membrane and a 100 μm chamber membrane. The 10 mm thick tissue plug comprised the epidermis, dermis, subcutaneous fat, and some underlying muscle. The formulation used consisted of 5 mg of tungsten particles 1 to 5 μm in diameter. The particles were positioned in the middle of the membrane concavity, forming a 1 to 2 mm diameter pile and were ejected 5 mm distant from the tissue. After the injection, excess powder was carefully swabbed from the surface and the tissue cut down the midline of the injection site to yield two pieces. The tissue was cut from the muscle to the skin surface in order to ensure that tungsten particles were not driven into the tissue by the scalpel blade. Out of the three samples, a successful localized injection was observed in one of them. This sample was embedded in Optimal Cutting Temperature (OCT) compound and snap-frozen in liquid nitrogen. Each mold was sectioned using a cryostat to yield 10 μm sections. The sections were lifted onto superfrost plus slides, air dried, fixed in acetone, and stained with hematoxylin. Representative sections are shown in Figure 5-12. The injection site is visible and well defined. The powder penetrated into the dermis to a depth of approximately 1 mm. Tungsten particles that were not able to penetrate in the skin are visible on top of the epidermis, which in the photographs appears as a thin blue/black layer.

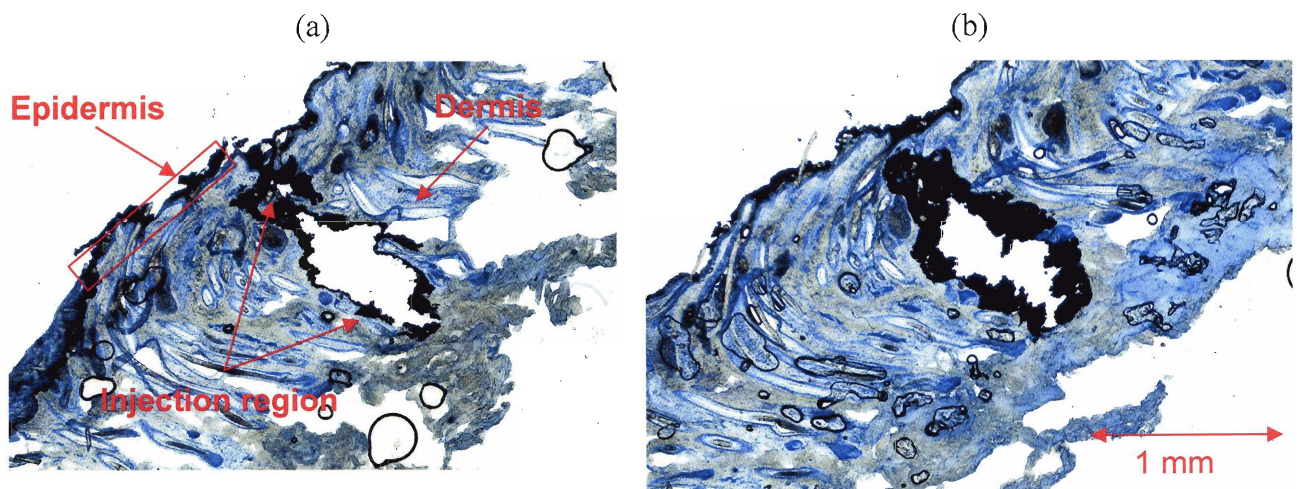


Figure 5-12: Transdermal injection in lamb skin.

Next, 3 mg of tungsten particles of the same size as before were fired into post-mortem pig skin. The head attachment described in Section 5.6 was used and the particles were spread to form an even layer over the membrane using a drop of alcohol. Three samples were injected again, but this time no localized injection was observed. However, studying the microtome sections, we found that the majority of tungsten powder which was visible at the edge of the skin was actually driven into the epidermis. This shallow delocalized injection resembled what Bellhouse et al. described in their patent [20] of the PowderJect device. With this skin we did not see the characteristic staining of the epidermis that was clearly pronounced in the lamb skin, which made us doubt its quality. But results from some other experiments seem to confirm the presence of epidermis, and we are inclined to believe that we performed a successful epidermal injection.

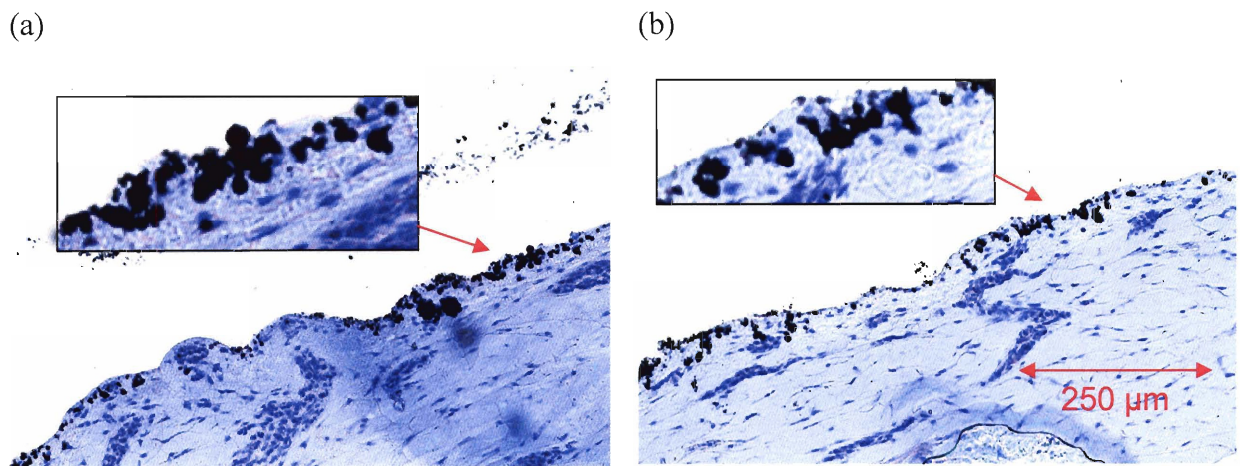


Figure 5-13: Epidermal injection in pig skin.

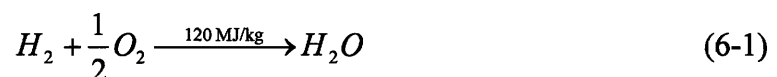
6 Combustion Analysis

6.1 Energy density of combustion

The experiments from the previous chapter demonstrate that the device powered by compressed nitrogen gas has the potential to successfully deliver powder drug to the epidermis and dermis. However, serious problem arises if we attempt to make the device reusable and portable. The compressed gas cartridge in these devices has a typical volume of 5000 mm³ and is good for a single injection. After that we have to either recharge it or replace it. Disposing will certainly make the use of the device too expensive, and carrying a large bottle of compressed nitrogen is impractical. The problem is the low energy density of compressed gases. At typical pressures used in compressed gas cylinders (~15 MPa) energy density varies between 0.15 MJ/kg for nitrogen and 1 MJ/kg for helium (or about 30 kJ/L for any gas). In contrast hydrogen releases 120 MJ/kg (1.2 MJ/L) when combusted, which is almost two orders of magnitude greater. Therefore as the next goal of our project, we attempted to produce a shock wave with similar characteristics to those produced in the nitrogen device, using a small explosion of hydrogen and oxygen gases.

6.2 Thermodynamic calculations for H₂ combustion

The familiar reaction of hydrogen and oxygen producing heated water vapor is:



This is a very simplified equation which only gives overall reaction balance for the case when we have complete combustion (products exhausted as far as possible) under stoichiometric conditions (products in exact molar proportions necessary for

complete chemical reaction, no excess of hydrogen or oxygen). In reality we can vary the initial conditions to run either fuel-rich (oxygen-deficient), or fuel lean (excess of oxygen). Under rich conditions, the excess hydrogen will be present post explosion, while under lean conditions, the excess oxygen will remain.

In order to obtain the thermo-dynamical conditions in the final mixture, we need to perform energy and chemical species (mass) balance, represented by the Equations (6-2) *a* and *b* respectively:

$$\alpha'_{H_2} u_{H_2}(T_i) + \alpha'_{O_2} u_{O_2}(T_i) = \alpha''_{H_2} u_{H_2}(T_f) + \alpha''_{O_2} u_{O_2}(T_f) + \alpha''_{H_2O} u_{O_2}(T_f), \quad (a)$$

$$2\alpha'_{H_2} = 2\alpha''_{H_2} + 2\alpha''_{H_2O}, \quad (b)$$

$$2\alpha'_{O_2} = 2\alpha''_{O_2} + \alpha''_{H_2O},$$

(6-2)

where α' and α'' are the moles of substance before and after the reaction, $u(T)$ is the internal energy (including energy of formation + thermal energy) at temperature T , T_i and T_f are the initial and final temperatures respectively. Because the heat capacities of the species are functions of the temperature, the internal energy is not a linear function of temperature. A good approximation is given by polynomial interpolation of the type:

$$u(T) = \left(a_0 + a_1 T + a_2 \frac{T^2}{2} + a_3 \frac{T^3}{3} + a_4 \frac{T^4}{4} + a_5 \frac{T^5}{5} \right) R, \quad (6-3)$$

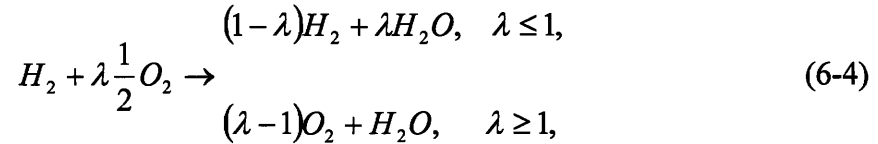
where T is in K, R is the gas constant and $u(T)$ is in J/mol. The coefficients a_i for the species of interest are given in the following table:

Chemical Species	a_0	a_1	a_2	a_3	a_4	a_5
H ₂	-8.35×10^2	1.99	7.00×10^{-4}	-5.63×10^{-8}	-9.23×10^{-12}	1.58×10^{-15}
O ₂	-1.23×10^3	2.70	6.14×10^{-4}	-1.26×10^{-7}	1.78×10^{-11}	-1.14×10^{-15}
H ₂ O	-2.99×10^4	1.67	3.06×10^{-3}	-8.37×10^{-7}	1.20×10^{-10}	-6.39×10^{-15}

Table 6-1: Coefficients for the energy polynomial used in the calculations.

6.2.1 Complete Combustion

If we assume that we have complete combustion, but not necessarily under stoichiometric conditions, then the reaction (6-1) becomes:



where λ is the excess-air ratio, defined as:

$$\lambda = \frac{(v_{H_2} / v_{O_2})_{actual}}{(v_{H_2} / v_{O_2})_{stoichiometric}}. \quad (6-5)$$

Using the energy Equations (6-2), we can calculate the final temperature and from then the final pressure as:

$$p = p_1 \frac{T}{T_1} \frac{\sum v_i''}{\sum v_i'}. \quad (6-6)$$

The results are shown in Figure 6-1. As could be expected, maximum pressure and temperature are achieved at stoichiometric conditions and pressure and temperature drop off quickly as we go either fuel rich or fuel lean. Assuming we start from room temperature, the final pressure is proportional to the initial pressure, and at $\lambda = 1$ the ratio is 12, that is we get 12-fold increase in pressure at the end of the combustion. This is the absolute maximum we can achieve, and it is only achieved if we assume complete combustion. As we will see in the next chapter, dissociation at high temperatures actually lowers the pressure and temperature. In the plot an initial pressure of 600 kPa is assumed, as used in most of our experiments. This model predicts a final pressure of 7.6 MPa.

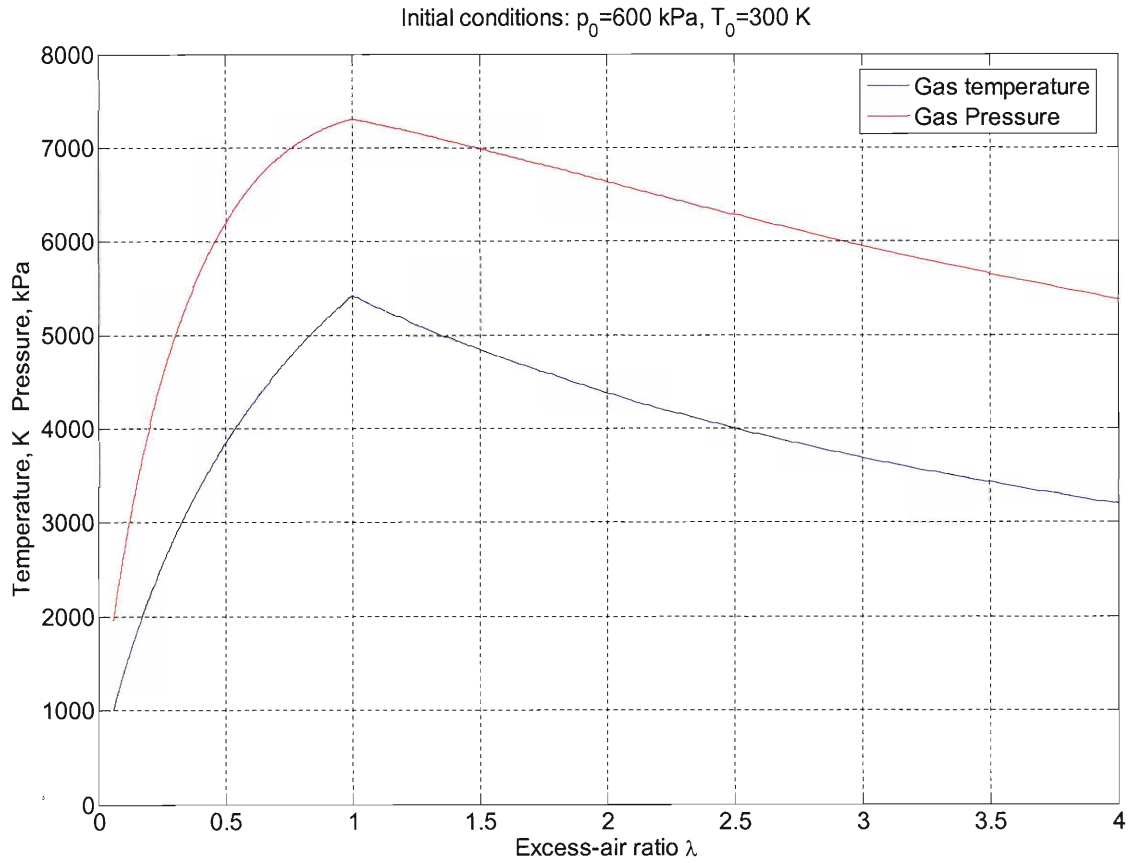
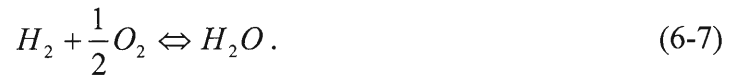


Figure 6-1: Final temperature of the product gases in Hydrogen-Oxygen combustion process.

6.2.2 Incomplete Combustion

Burning is an irreversible thermodynamic process, and proceeds only as long as the entropy increases with time. By performing the reaction analysis again, and taking this into account, it is clear that complete combustion is idealization that never occurs in reality. Instead a chemical equilibrium is reached in which both forward and reverse reactions occur:



To quantify this effect in the case of reacting gases, equilibrium constant is defined as:

$$K_{H_2O} = \frac{P_{H_2} P_{O_2}^{1/2}}{P_{H_2O}}. \quad (6-8)$$

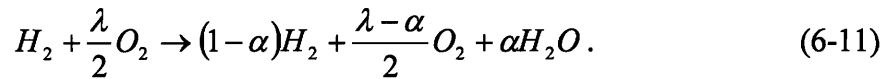
But partial pressures of gases in mixture are proportional to the species concentrations and therefore if $[X]$ is the concentration of the species X in the equilibrium state, then:

$$K_{H_2O} = \frac{[H_2][O_2]^{1/2}}{[H_2O]} \sqrt{p}. \quad (6-9)$$

For perfect gas the equilibrium constant, is only a function of the temperature and is determined by the Gibbs free energy of the reaction from the equation:

$$K = \exp\left(-\frac{\Delta G_{H_2O}}{RT}\right). \quad (6-10)$$

Like in the previous section we start with 1 mol of Hydrogen and $\lambda/2$ moles of oxygen but this time we have for the final state:



The parameter α is to be determined subject to the constraints $\lambda \geq \alpha$, $0 \leq \alpha \leq 1$.

Converting Equation (6-11) into an energy equation gives us:

$$\alpha = \frac{\left(u_{H_2}(T) + \frac{\lambda}{2}u_{O_2}(T)\right) - \left(u_{H_2}(T_0) + \frac{\lambda}{2}u_{O_2}(T_0)\right)}{u_{H_2}(T) + \frac{1}{2}u_{O_2}(T) - u_{H_2O}(T)}. \quad (6-12)$$

The equilibrium equation expressed in terms of α is:

$$\frac{(1-\alpha)\left(\frac{\lambda-\alpha}{2}\right)^{1/2}}{\alpha\left(1+\frac{\lambda-\alpha}{2}\right)} = \frac{1100 \times \exp\left(-\frac{3 \times 10^4}{T}\right)}{\sqrt{\frac{p_1}{p_0} \frac{T}{T_0} \left(\frac{1+\frac{\lambda-\alpha}{2}}{1+\frac{\lambda}{2}}\right)}}. \quad (6-13)$$

The temperature must be measured in K and p_0 is atmospheric pressure. Numerically solving Equations (6-12) and (6-13) produces the graphs in Figure 6-2. For comparison the results for complete combustion obtained in the previous chapter are also plotted. Far from stoichiometric conditions (resulting in lower final temperatures), the two models converge, because dissociation becomes insignificant. Only close to $\lambda = 1$ is the effect of dissociation significant, resulting in reduced

temperature and pressure of the burned gases. The graphs also become smoother near the maxima, and are not as sensitive to variations in λ as they are for complete combustion. The maximum temperature and pressure decrease to 4300 K and 6.6 MPa respectively, but change less than 1% in the interval $0.7 \leq \lambda \leq 1.2$.

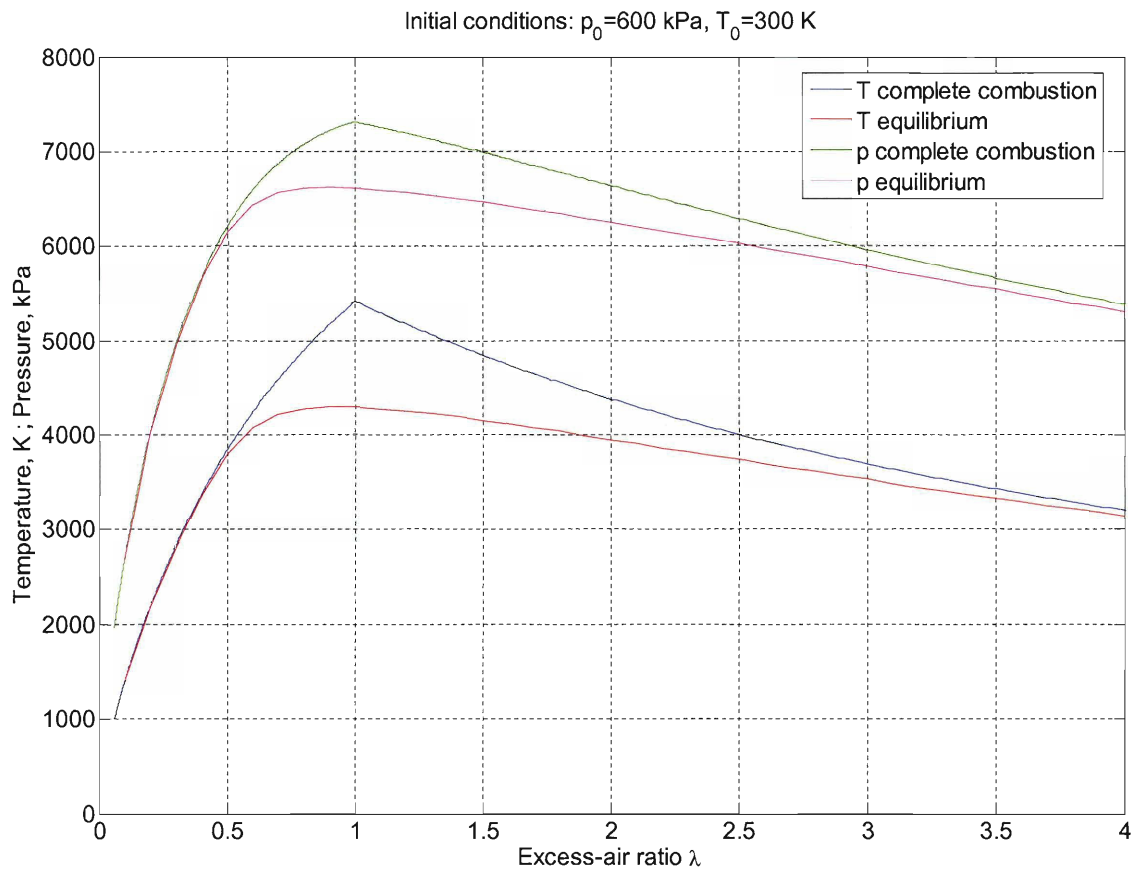


Figure 6-2: Thermodynamic state of the hot products, assuming equilibrium state is reached.

6.3 Effects of temperature on the shock wave

In Section 3.6 we described the procedure to calculate the properties of the shock wave formed in a shock tube. The same procedure can be used in the case when we have hot gases in the high pressure chamber resulting from hydrogen-oxygen combustion. The predictions, however, are not as reliable as in the case of expanding nitrogen, because the behavior of the hot gases deviates more from the isentropic assumption. The high temperatures and the resulting high temperature gradients will accelerate the heat

exchange with the walls and within the gas. Also, because the membrane ruptures before the combustion is completed, there is a net heat generation during the shock wave propagation. Trying to model these additional factors is prohibitively complicated, so in the quantitative predictions they are neglected. Qualitatively we can say that the heat exchange with the walls will slightly decrease the gas temperature, slowing down the expansion. Conversely, the continued combustion will increase the temperature and the speed as the shock wave propagates.

From the measurements in Section 5.3.3 it has been shown that the 100 μm polyester membrane ruptures at about 4 MPa. The corresponding temperature of the burning gases necessary to achieve this pressure, starting from 600 kPa initial pressure, is about 3000 K. Figure 3-6 shows the relation between the initial pressure ratio and the shock strength for superheated water vapor at 3000 K. The elevated temperature increases the local speed of sound to 1340 m/s, and as a result increases significantly the strength of the shock wave. For an initial pressure of 4 MPa, the pressure ratio across the shock wave increases 3 times compared to the case of nitrogen (from ~ 5 to ~ 15). This accelerates the shock wave to 1200 m/s and the gas behind it to 930 m/s. A comparison of the predicted thermodynamic quantities for each of the shock waves is given in Table 6-2. In terms of speed and strength the combustion generated shock wave outperforms the compressed gas generated wave. However the combustion generated shock wave carries with it very hot gases, which are a major complication. These gases must either be contained in the device or be directed away from the injection tissue, because they can result not only in severe burning but can also destroy the medication.

Case	p_1 , MPa	p_4 , MPa	T_1 , K	T_4 , K	a_1 , m/s	a_4 , m/s	p_2 , MPa	c_s , m/s	u_2 , m/s	T_2 , K	T_3 , K
Compressed Nitrogen	0.1	4.0	300	300	343	343	4.8	700	450	508	160
Hydrogen Combustion	0.1	4.0	300	3000	343	1340	14.5	1215	932	988	2240

Table 6-2: Comparison between the calculated properties for the shock waves generated under the different experimental conditions.

7 Hydrogen Combustion Experiments

7.1 Modifications of the setup

A set of experiments was designed and carried out to test the theoretical combustion models. As mentioned previously, the experimental setup was designed so that it can be reused for combustion experiments. However, certain modification had to be made.

The two intake ports of the rupture chamber were connected through check-valves (20 MPa max, 7 kPa opening pressure) with Festo solenoid valves (24V DC, 0.8 MPa max). As there was no suitable direct way to measure and adjust the amount of hydrogen and oxygen entering the chamber, we took an indirect approach using the gas pressure as an indicator. If a pre-combustion pressure of 600 kPa was desired, to achieve stoichiometric conditions, the oxygen regulator was set to 200 kPa and the hydrogen to 600 kPa. The chamber was initially flushed with oxygen to remove air and any waste gases and then sealed from the top, either with a membrane or a cap, depending on the experiment. The oxygen valve was opened again, until the pressure equilibrates and then closed. The same was repeated for the hydrogen valve.

A polyimide spark plug was used to ignite the mixture with the high voltage to the spark provided by a mechanically actuated piezo-crystal device. The high voltage pulse created by the piezo crystal radiated a strong electromagnetic that could be detected immediately. We decided to use this pulse as an indicator of the beginning of the combustion and utilized it to synchronize the data acquisition devices. It appeared as a series of spikes in the pressure sensor channels, and was used to trigger the oscilloscope acquisition. It also created a voltage pulse at the output of the circuit in Figure 7-1, which triggered the high speed camera

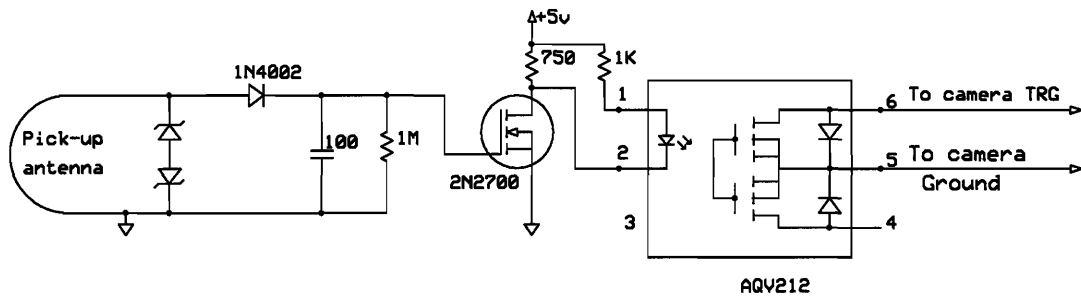


Figure 7-1: Triggering circuit for the high-speed camera.

Most of the combustion experiments we performed did not require any external light source as the hot gases were luminescent enough to be imaged by the high speed camera.

7.2 Hydrogen flame propagation and pressure rise

In order to study the combustion dynamics, a transparent PMMA cover was used to seal the top of the chamber, and combustion was performed under stoichiometric conditions. The images in Figure 7-2 were taken with the high-speed camera looking down at the chamber ($38 \mu\text{s}$ intervals, $17 \mu\text{s}$ exposure time). The whole combustion chamber, having a diameter of 20 mm is visible. The initial conditions for the mixture were room temperature and 600 kPa pressure. The graph of the pressure during the process is shown in Figure 7-3a, and Figure 7-3b shows the rising portion of the graph in more detail.

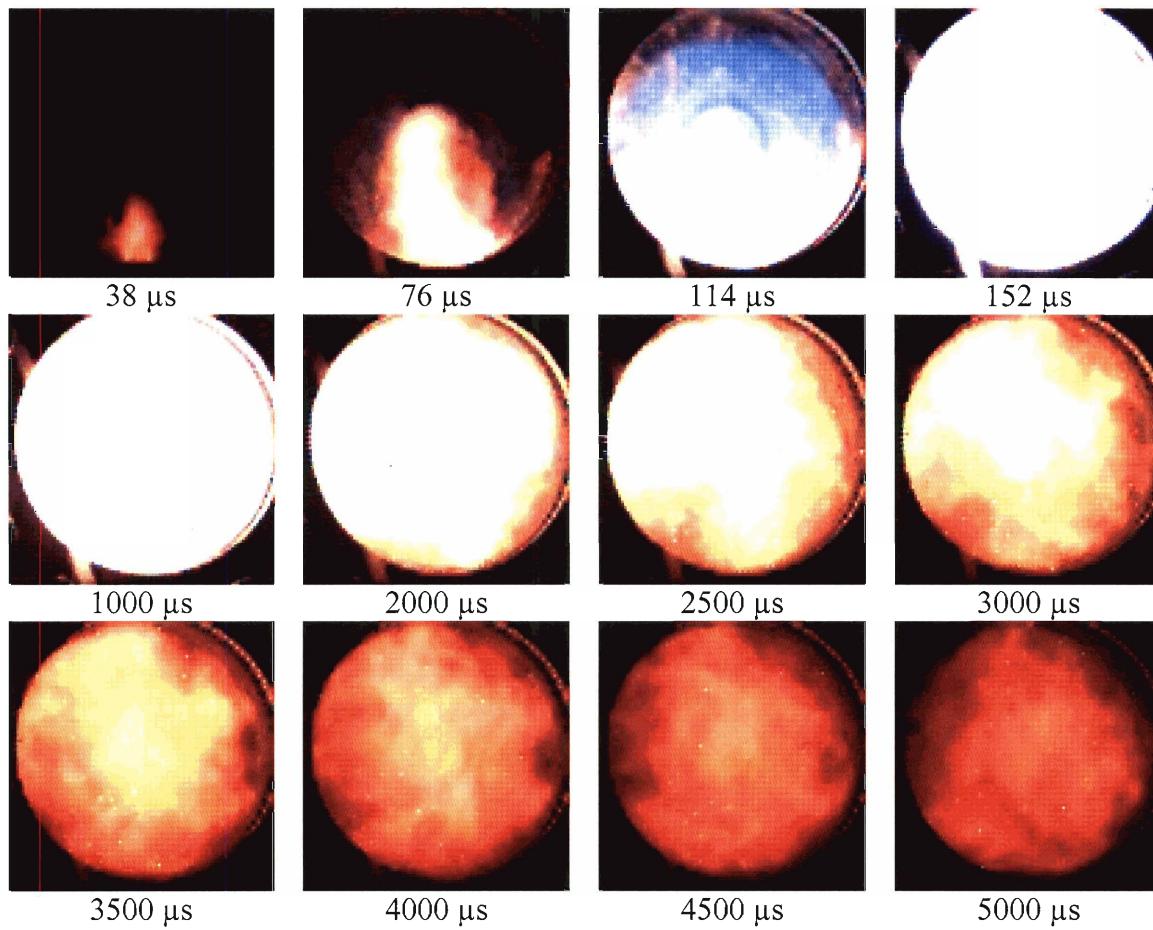


Figure 7-2: Images from constant volume stoichiometric hydrogen burning.

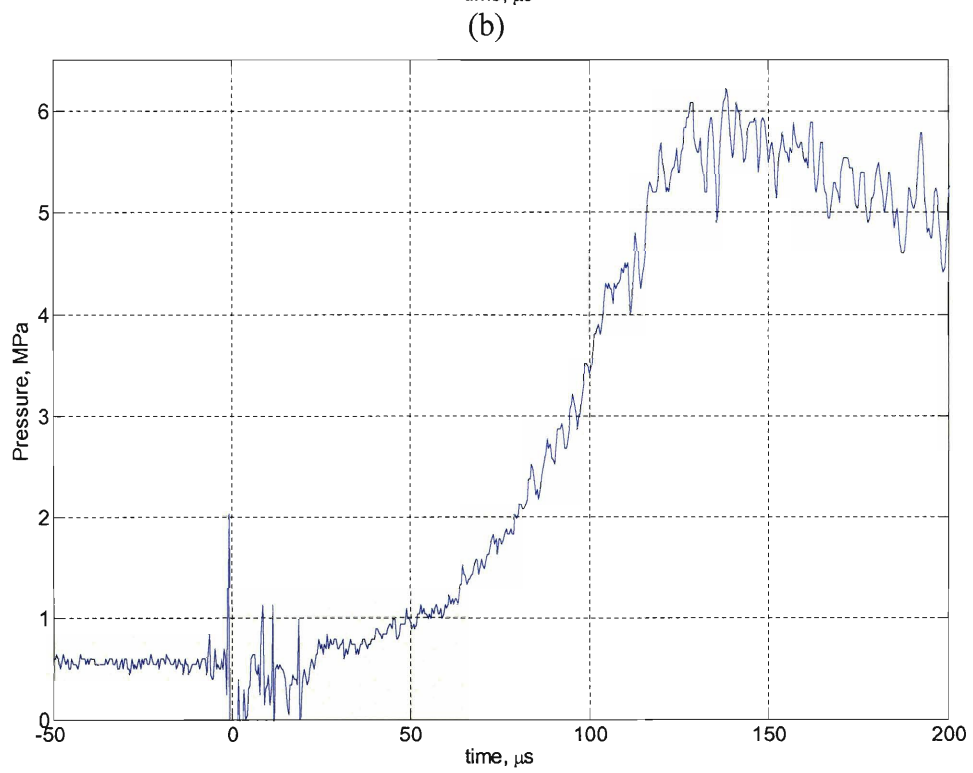
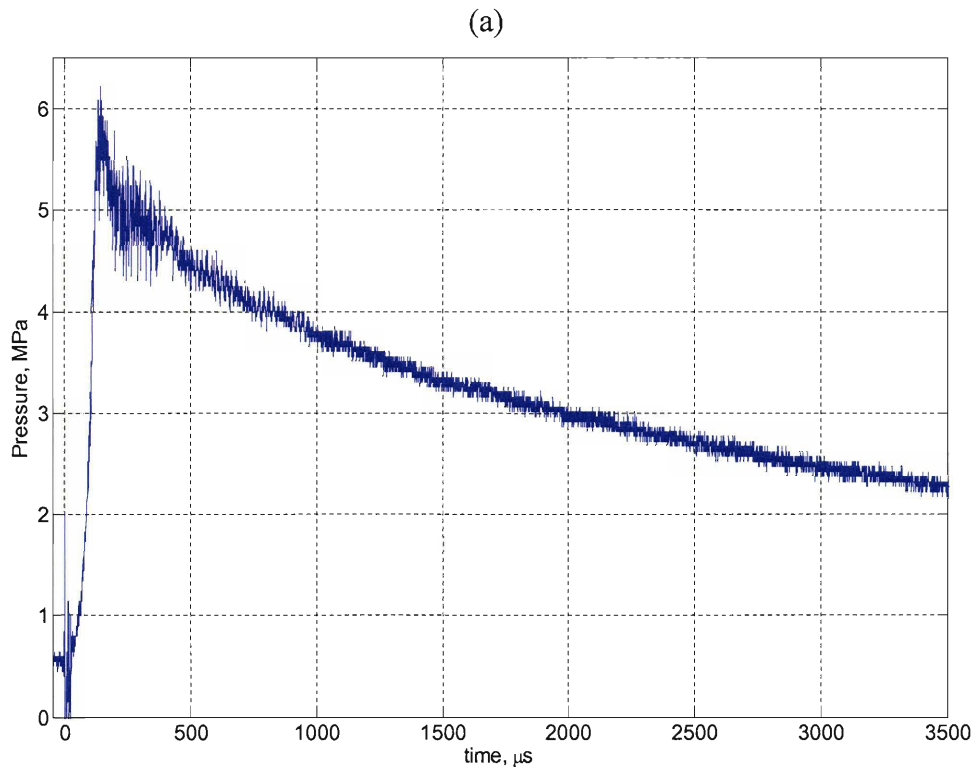


Figure 7-3: Measured pressure during the combustion process.

According to the images it takes about 150 μs for the flame to fill the combustion chamber which corresponds to the pressure rise in Figure 7-3b. No further pressure rise is observed after that, which implies that the combustion process is very fast, and each volume of gas burns as soon as the flame front reaches it. Therefore what we observe on the pictures from the later times is not burning gas, but rather hot products residing in the chamber. The maximum reached pressure of 6 MPa is very close to the value predicted by the incomplete combustion model described in Section 6.2.2, indicating that chemical equilibrium is quickly attained.

From the size of the chamber, and the time it takes the flame to cross it, we can obtain a mean apparent flame speed of 130 m/s. This, however, is not the real flame speed, as the hot gases exiting the flame expand, raise the pressure and compress the cold reactants ahead of the flame. The flame speed with respect to the gas is given by:

$$u_{\text{flame}} \approx \frac{\rho_{\text{burned}}}{\rho_{\text{unburned}}} u_{\text{apparent}} \quad (7-1)$$

This gives an estimate for the laminar flame speed of about 20 m/s, which is rather high for a laminar flame. This can be attributed to the high heating value of the hydrogen-oxygen reaction, the high thermal conductivity of hydrogen and the reactive OH radicals formed. As the flame propagates the flame front area and the burning rate increases explaining the increasing slope of the pressure graph.

The images and the pressure data can also help us estimate the significance of the heat exchange with the wall. We see that it takes about 2 ms for the pressure to drop from 6 MPa to 3 MPa, which is an order of magnitude longer than the pressure rise time. A fraction of this decrease is also attributed to the “dead space” inside the check valves. Therefore the heat losses to the wall are very small for the initial stages of combustion and could be neglected.

7.3 Shock wave propagation

Shock wave measurements, similar to the ones performed in Section 5.3.3 were done with the combustion setup and the recorded pressures are given in Figure 7-4. The first thing to notice is that the signal was extremely noisy in this case. Because we do not see any noise in the second channel before the arrival of the shock wave, we believe that

this is not an electrical artifact, but real pressure fluctuations due to ongoing combustion processes and turbulences created. We also noticed that the pressures achieved in the chamber before the rupture are significantly different from the ones in the nitrogen device. We observe about 4 MPa for the 50 μm membrane and about 7 MPa for the 100 μm membrane. This perhaps indicates that the membrane rupture pressure is a function of the rate of increase of pressure, as in this case the rate is much higher than in the compressed nitrogen case.

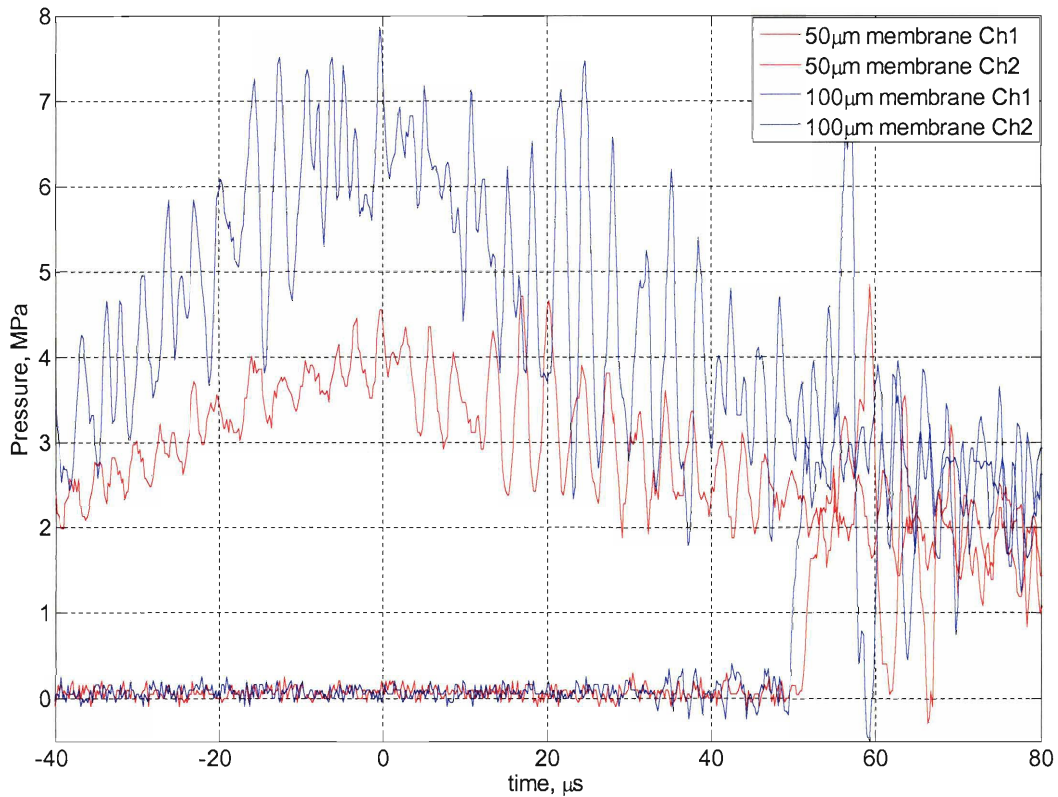


Figure 7-4: Shock wave pressure measurements.

Figure 7-4 indicates about 50 μs interval between the onset of the pressure decrease in the combustion chamber and the shock wave recorded by the downstream pressure transducer. Estimating the time it takes the expansion wave to reach the chamber transducer to 10 to 15 μs , we calculate shock wave speed of 1300 to 1500 m/s- more than twice as high as that measured in the compressed gas device. The strength of the shock wave for the two membranes is 1.6 and 1.8 MPa respectively and the rise time is shorter than before- only about 1 to 2 μs . From these numbers, using the shock wave relations we predict gas velocity close to 1000 m/s. To test this number we observe the propagation of

the hot gases behind the shock wave in a translucent shock tube. Figure 7-5 (22 μs frame interval, 9 μs exposure time) shows an experiment using 50 μm polyester chamber membrane (4 MPa maximum chamber pressure). The measured speed of the shock wave was 1050 m/s, which agrees well with the estimated value. We conclude that the shock wave created by combustion is stronger than the shock wave created by compressed gas, has a shorter rise time and travels substantially faster.

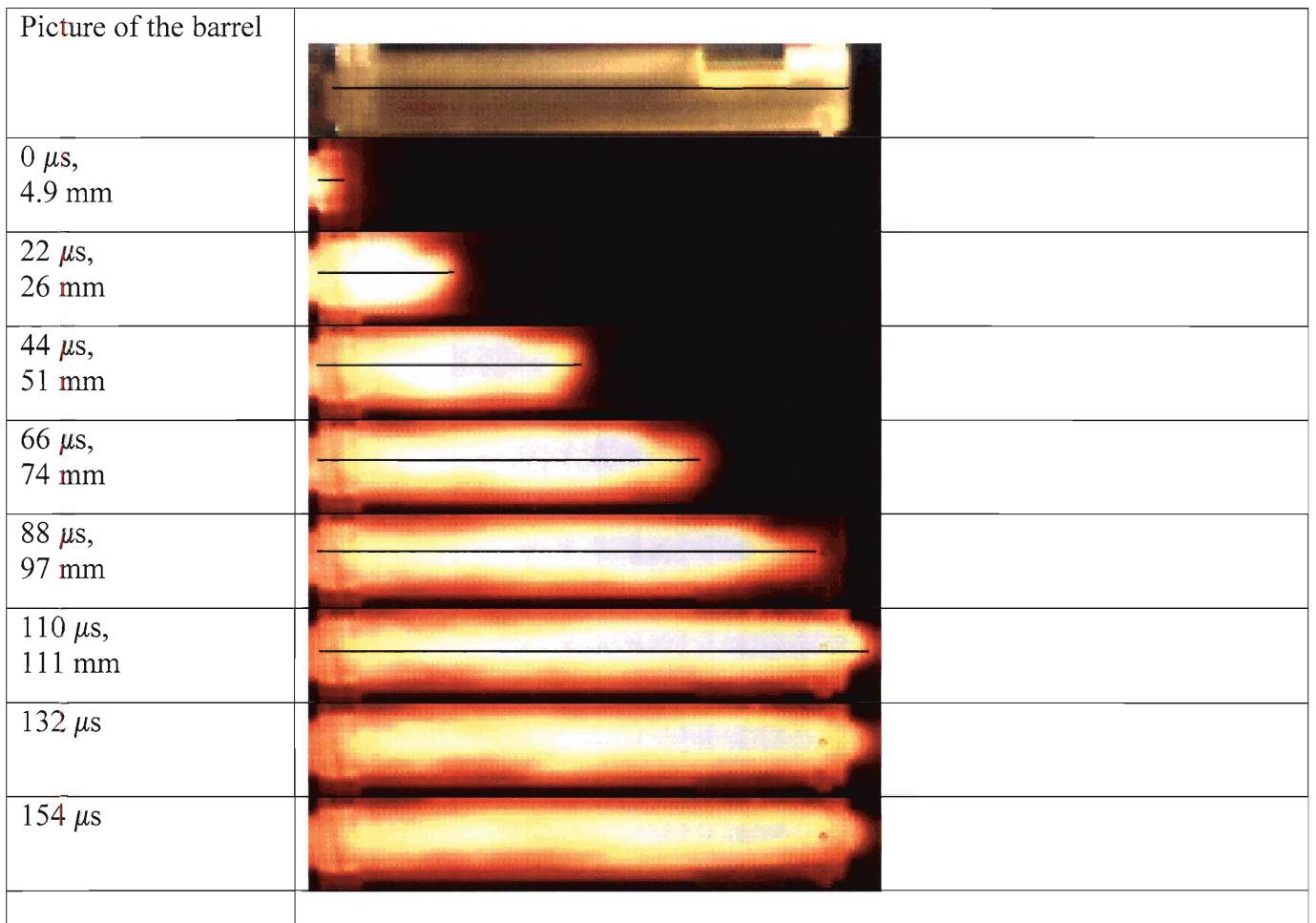


Figure 7-5: Combustion generated shock wave propagating in a translucent shock tube.

7.4 Accelerated plastic slug

In a series of experiments an alternative to the double membrane injections setup used in the compressed nitrogen experiments was tested. A plastic cylinder 10 mm in

diameter and 6 mm thick was cut out of acrylic and placed at the base of the shock tube. After the rupture of the membrane the slug was accelerated along the barrel and flew out at high speeds. Tungsten powder was placed in a pit in the middle of the slug and accelerated together with it. A metal plate with a hole in the middle stopped the slug, but allowed the formulation to continue ahead.

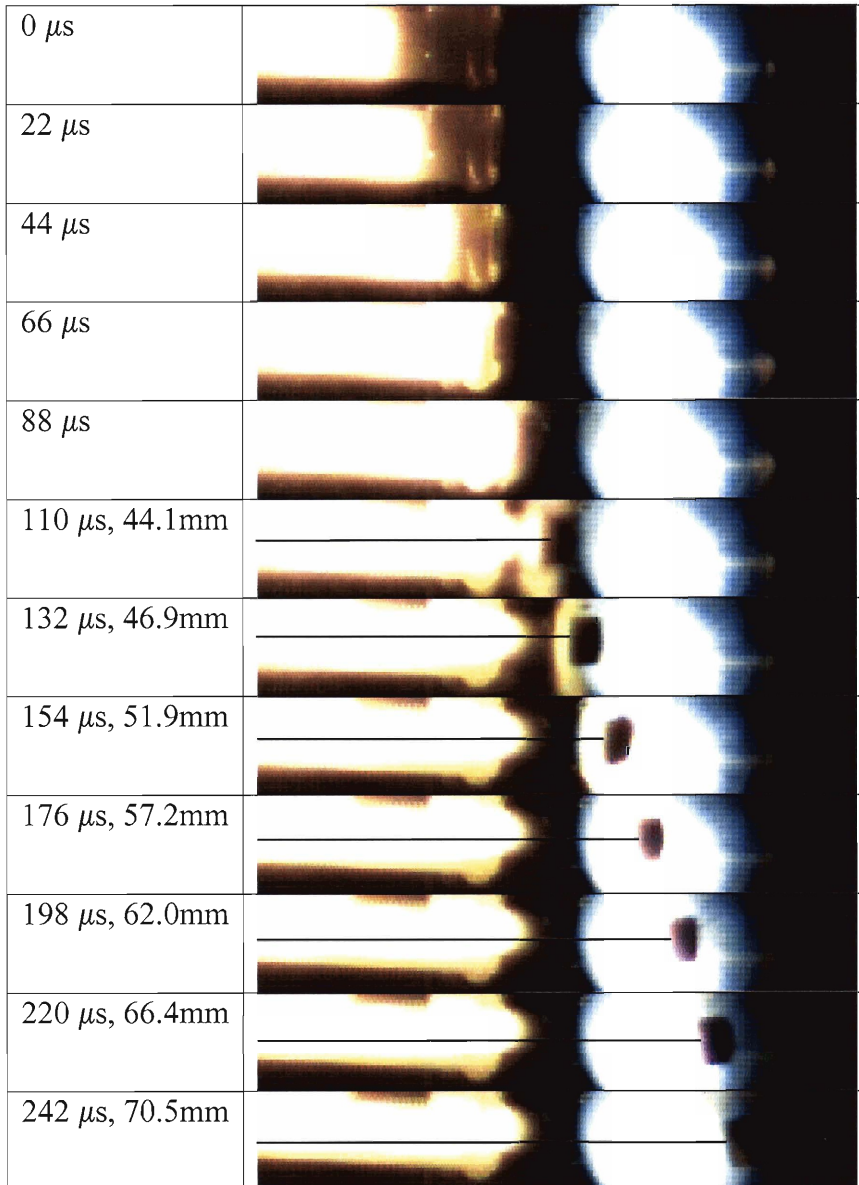


Figure 7-6: Plastic slug accelerated by the hot gases in the shock tube.

The experiment shown in Figure 7-6 used the 50 μm polyester chamber membrane. Because the slug prevented the hot gases from escaping after membrane

rupture, the pressure reached a maximum of 6 MPa. The slug left the device at a speed of 210 m/s. This speed is satisfactory, and demonstrates the potential of the method. A problem we faced was that we could not find a way to stop the slug without breaking it to pieces and thus creating a cloud of debris which continued flying along with the powder. So if this method was to be used, further work was required.

7.5 Alternative Methods of Powering the Device

In the view of making the device fully portable and powered from a conventional source like a battery, rather than compressed hydrogen, we attempted to produce hydrogen and oxygen in place by electrolyzing water. A current of 4 A produces 2.1×10^{-5} mol/s, which is about 40 $\mu\text{g/s}$. To fill the combustion chamber we needed about 1.7 mg of hydrogen at atmospheric pressure, which could be produced in less than a minute at this rate. We had to face two challenges- producing and storing the hydrogen and oxygen separately and producing them at the high pressure needed- 600 kPa as the target pressure for the reactants before the beginning of combustion. We tried two different devices- traditional electrolyzer and an electrolyzer using PEM.

The traditional electrolyzer we made is shown in Figure 7-7a. The electrodes were coaxial, (the central one being the anode) and 40% NaOH was used as electrolyte. The anode shown in Figure 7-7b was made out of nickel in order to be corrosion-resistant. It was cut using a wire EDM in a star shape in order to increase the surface area and therefore the rate of gas production. The cathode, made out of sheet steel, was attached to the wall of the cylindrical plastic body. A plastic separator with many holes was placed between the anode and the cathode. It provided easy passage for the ions in the solution but prevented the gases from mixing directly into the device.

Using this device we managed to achieve gas pressures of up to 700 kPa within 5 minutes. The relatively long time was due to the low currents achieved (less than 1 A). We managed to ignite the mixture and recorded pressures similar to the pressures, achieved using hydrogen and oxygen from gas cylinders. The device however did not manage to properly separate the hydrogen and oxygen, and during one of the experiments

the flame from the combustion chamber backfired into the electrolyzer and destroyed the device. Also the nickel anode slowly oxidized with time, deteriorating the operation of the device.

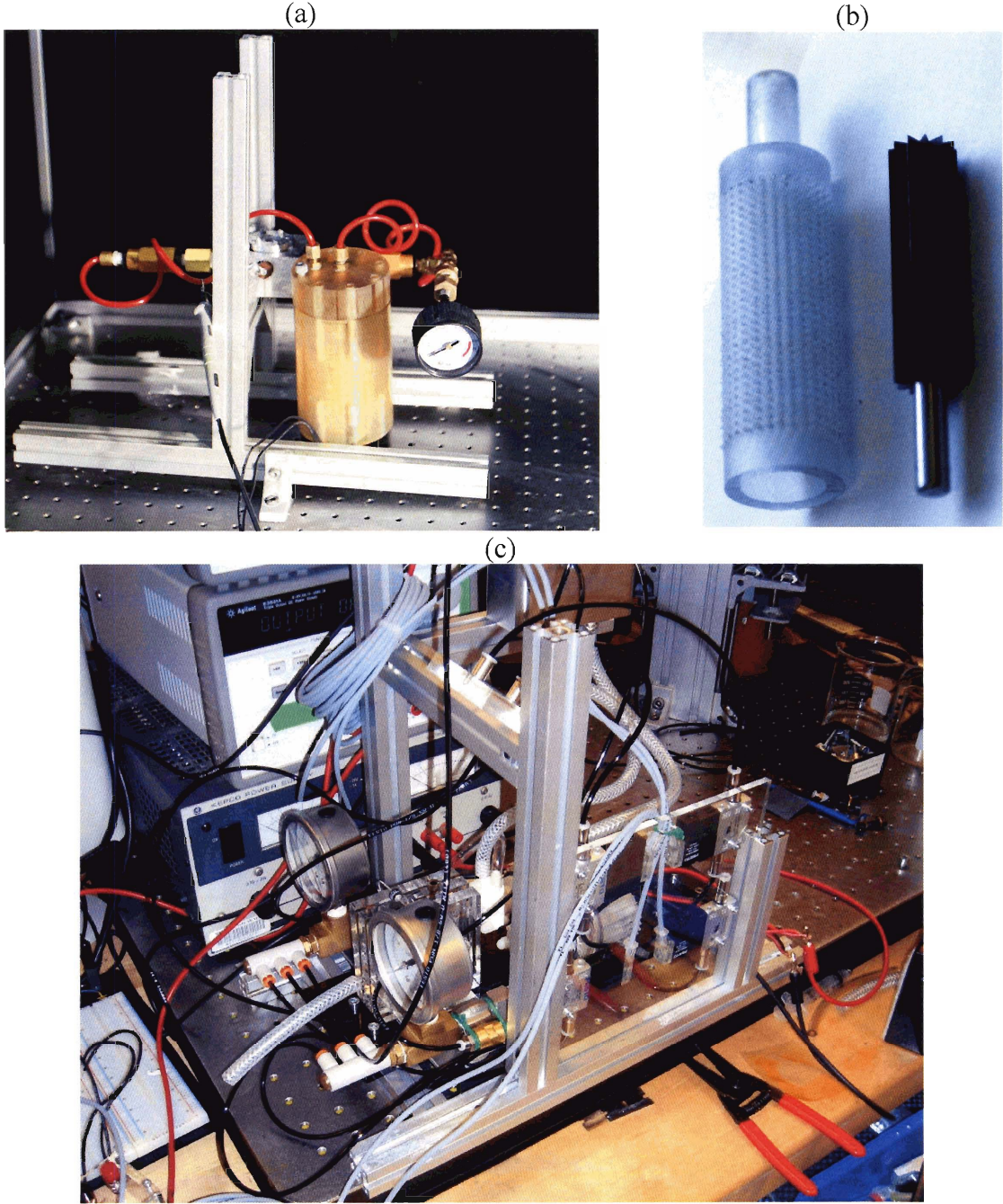


Figure 7-7: Electrolyzers for hydrogen production.

In attempt to get better performance and reliability we tried to constructed an electrolyzer based on Nafion membrane. Nafion is a sulfonated Teflon copolymer, which does not conduct electrons and anions, but allows cations to pass through ionic channels. In our set up it was used as Proton Exchange Membrane (PEM), allowing the hydrogen cations to reach the cathode and neutralize to produce hydrogen. Oxygen and the water were retained on the other side of the membrane. Additional advantages in using PEM were that the electrolyte needed was simply distilled water and higher current densities were achieved. The device we built using a commercial PEM electrolyzer is shown in Figure 7-7c. Water was circulated by the pumps between water reservoirs and the electrolyzer, and the gases were carried to the storage tanks at the top of the picture. This allowed us to run the hydrogen-oxygen production in continuous mode, obviating the need to wait every time to produce the gases right before an experiment.

We achieved high rates of gas production, significantly outperforming the traditional style electrolyzer (4A compared to less than 1A). Also the gases were successfully separated and kept apart. However the commercial device failed to reach significant increase in pressure. It was clearly not designed to operate under pressure and numerous leaks showed in the device, along with decreasing performance at high pressures. We attempted to build a PEM electrolyzer on our own, but never achieved the operational characteristics of the commercial device. We did not rule out using PEM as a means to produce pressurized hydrogen, but apparently it was not in our expertise.

8

Conclusions and Future Work

We demonstrated that a shock-wave device powered by compressed nitrogen has the potential to accelerate tungsten particles to almost 300 m/s. We also showed that this speed is sufficient to allow the particles to penetrate the stratum corneum and reach the lower layers of the viable epidermis. We described a theoretical model for the formation and the propagation of the shock wave, and supported it with experimental evidence. We proved that combustion of hydrogen and oxygen, carried out under the correct conditions, creates even stronger and faster shock waves than compressed gas creates and therefore can be used effectively to power the injection device. Finally we showed how hydrogen can be produced in place, so that the device is independent of a hydrogen supply.

However a great deal of work still needs to be done before this device can be realized as a medical device. First and foremost the safety of the patient must be guaranteed. The shock wave carries a lot of energy, and if not handled carefully, this energy can cause serious damage. It has to be contained and kept away from the patient, which is especially challenging in the case of the hot combustion products of the hydrogen-oxygen reaction. Future iterations of this device should concentrate on minimizing the combustion volume in order to create a very short shock wave pulse and increase efficiency. The check valves have to be integrated in the chamber in order to minimize losses and maximize pressure. Velocity measurements have to be conducted using this optimized setup comparing its performance to the compressed nitrogen device. A simple and quick way must be developed to manufacture the chamber, (for example from plastics using a laser cutter). Membrane change must be performed with a single motion and adjustable depth of penetration must be provided by varying the pressure in the chamber. Finally the sterility of the device must be guaranteed to prevent cross contamination.

Appendix

A Material And Physical Properties

From Air Liquide website: <http://www.airliquide.com/en/>

A.1 Physical Properties of Air

- Molecular weight : 28.95 g/mol
- Gas density (1.013 bar at boiling point) : 3.2 kg/m³
- Gas density (1.013 bar and 15 °C (59 °F)) : 1.202 kg/m³
- Compressibility Factor (Z) (1.013 bar and 15 °C (59 °F)) : 0.9992
- Specific gravity (air = 1) (1.013 bar and 21 °C (70 °F)) : 1
- Specific volume (1.013 bar and 21 °C (70 °F)) : 0.833 m³/kg
- Heat capacity at constant pressure (Cp) (1.013 bar and 21 °C (70 °F)) : 0.029 kJ/(mol.K)
- Heat capacity at constant volume (Cv) (1.013 bar and 21 °C (70 °F)) : 0.02 kJ/(mol.K)
- Ratio of specific heats (Gamma:Cp/Cv) (1.013 bar and 21 °C (70 °F)) : 1.4028
- Viscosity (1 bar and 0 °C (32 °F)) : 0.0000169 Pa.s
- Thermal conductivity (1.013 bar and 0 °C (32 °F)) : 0.0239 W/(m.K)

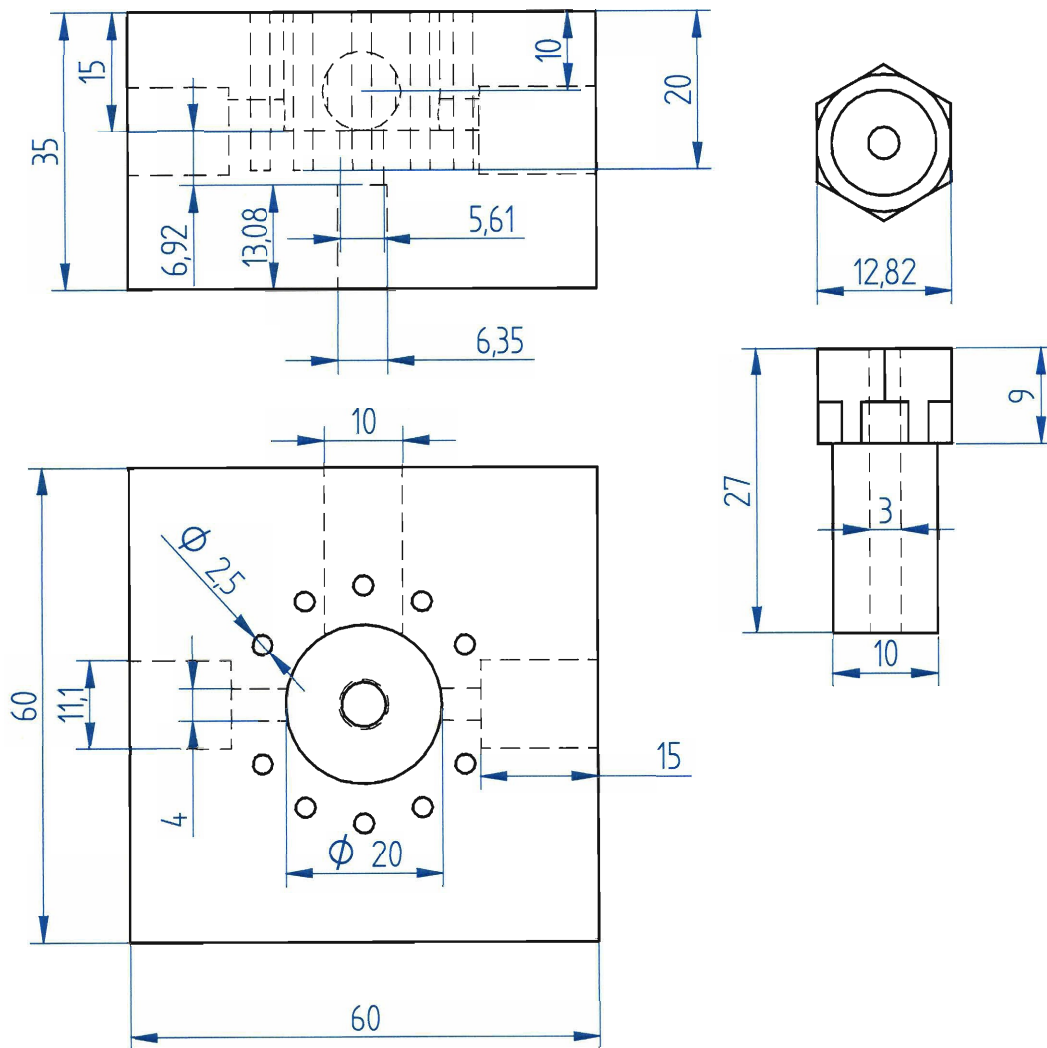
A.2 Physical Properties of Hydrogen

- Molecular weight : 2.016 g/mol
- Gas density (1.013 bar at boiling point) : 1.312 kg/m³
- Gas density (1.013 bar and 15 °C (59 °F)) : 0.085 kg/m³
- Compressibility Factor (Z) (1.013 bar and 15 °C (59 °F)) : 1.001
- Specific gravity (air = 1) (1.013 bar and 21 °C (70 °F)) : 0.0696
- Specific volume (1.013 bar and 21 °C (70 °F)) : 11.986 m³/kg
- Heat capacity at constant pressure (Cp) (1 bar and 25 °C (77 °F)) : 0.029 kJ/(mol.K)
- Heat capacity at constant volume (Cv) (1 bar and 25 °C (77 °F)) : 0.021 kJ/(mol.K)
- Ratio of specific heats (Gamma:Cp/Cv) (1 bar and 25 °C (77 °F)) : 1.384259
- Viscosity (1.013 bar and 15 °C (59 °F)) : 0.0000086 Pa.s
- Thermal conductivity (1.013 bar and 0 °C (32 °F)) : 0.1683 W/(m.K)

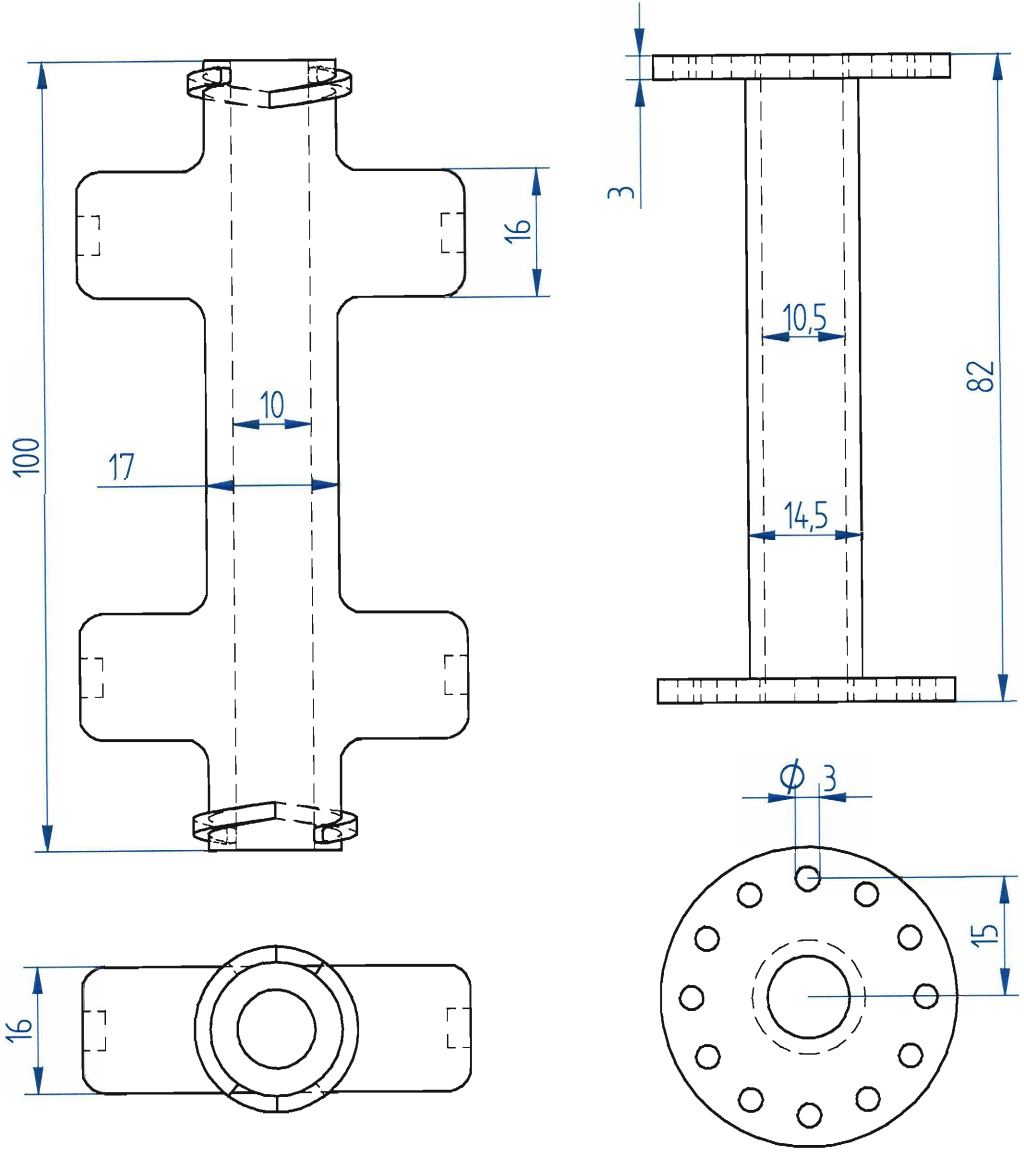
B Drawings

All dimensions are in mm.

Chamber and Spark Plug



Shock Tubes



C Code and simulations

C.1 Matlab Shock wave graphs

This function graphs the Mach number relation across a stationary shock wave

```
gamma=1.4;
M1=[1:0.1:10];
M2=sqrt((1+(gamma-1)/2*M1.^2)./(gamma*M1.^2-(gamma-1)/2));
plot(M1,M2);
xlabel('M1- Supersonic flow');
ylabel('M2- Subsonic flow');
grid on;
```

The function below produces graph for the velocity of shock wave generated from a compressed nitrogen chamber as a function of the initial pressure ratio

```
%Shock velocity vs initial pressure ratio for nitrogen
clear;
clc;
gamma1=1.4;
gamma4=1.4;
a1=343;
a4=343;

x1=[1.1:0.02:5.5];
y1=x1.*(1-(gamma4-1)*(a1/a4)*(x1-
1)./(sqrt(2*gamma1)*sqrt(2*gamma1+...
(gamma1+1)*(x1-1))))).^(-2*gamma4/(gamma4-1));

cs=a1*sqrt((gamma1-1)/(2*gamma1)+(gamma1+1)/(2*gamma1)*x1);
plot(y1,cs);
xlabel('Initial Pressure Ratio p_4/p_1');
ylabel('Shock Velocity, m/s');
axis([0 60 350 750]);
grid on;
```

C.2 MathCad shock wave model

This document presents some calculations on shock wave propagation using a shock tube model. The the high pressure gas is nitrogen at $p=4\text{MPa}$ and temperature of $T=293\text{K}$, and the low pressure gas is air at $p=101\text{kPa}$ and $T=293\text{K}$. Once a polyester membrane breaks a shock wave is formed, propagating down the cylindrical barrel, while an expansion wave propagates in the opposite direction inside the chamber. The model is concerned with the events following the explosion. p_4 refers to the initial pressure in the chamber (and the pressure ahead of the expansion wave), $p_3=p_2$ is the pressure in the gas between the shock wave and the expansion wave, and p_1 is the pressure ahead of the shock wave. Same for all other gas properties. The assumption is that the gasses on the two side of the membrane do not mix, even after the rupturing event. The flow is assumed to be isentropic.

The properties of the gases on both side of the membrane are as follows

$$R_g := 8.31 \frac{\text{J}}{\text{mol}\cdot\text{K}}$$

$$\gamma_1 := 1.4$$

$$T_1 := 293\text{K}$$

$$p_1 := 101 \times 10^3 \text{Pa}$$

$$\mu_1 := 28.95 \times 10^{-3} \frac{\text{kg}}{\text{mol}}$$

$$\gamma_4 := 1.4$$

$$T_4 := 293\text{K}$$

$$p_4 := 4 \times 10^6 \text{Pa}$$

$$\mu_4 := 29 \times 10^{-3} \frac{\text{kg}}{\text{mol}}$$

$$a_1 := \sqrt{\frac{\gamma_1 \cdot R_g \cdot T_1}{\mu_1}}$$

$$a_1 = 343.142 \frac{\text{m}}{\text{s}}$$

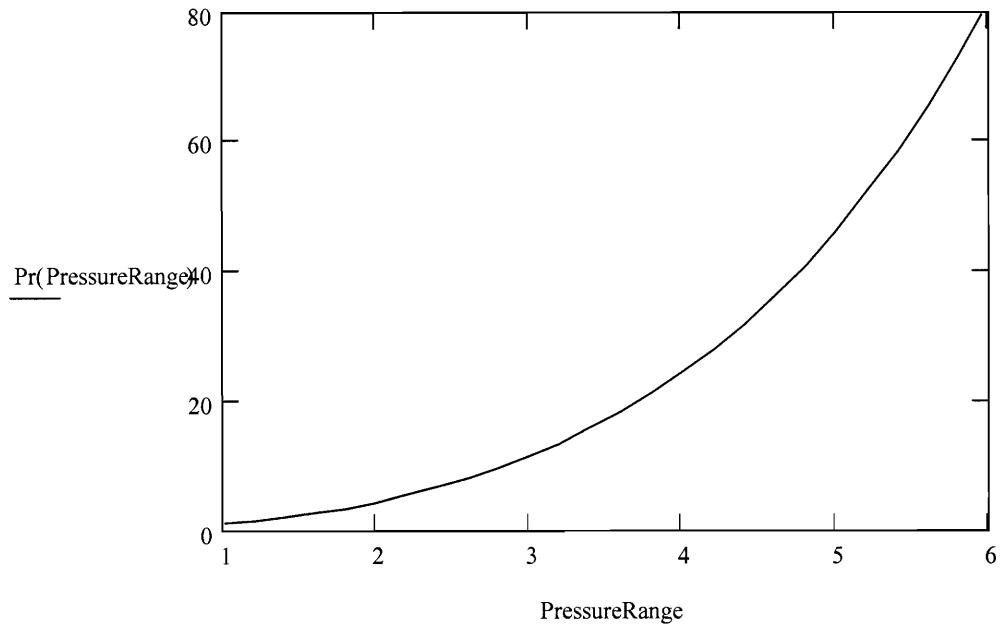
$$a_4 := \sqrt{\frac{\gamma_4 \cdot R_g \cdot T_4}{\mu_4}}$$

$$a_4 = 342.846 \frac{\text{m}}{\text{s}}$$

Pressure ratio p_2/p_1 is x , and p_4/p_1 is $y=\text{Pr}(x)$. We know that $y=p_4/p_1=4\text{MPa}/100\text{kPa}=40$

$$\text{Pr}(x) := x \left[1 - \frac{(\gamma_4 - 1) \cdot \left(\frac{a_1}{a_4}\right) \cdot (x - 1)}{\sqrt{2 \cdot \gamma_1} \cdot \sqrt{2 \cdot \gamma_1 + (\gamma_1 + 1)(x - 1)}} \right]^{\frac{-2\gamma_4}{\gamma_4 - 1}}$$

PressureRange := 1, 1.2.. 6



We can read from the graph $p_2/p_1=4.78$, giving us

$$Pr(4.78) = 40.27$$

$$PressureRatio := 4.78$$

$$p_2 := p_1 \cdot PressureRatio$$

$$p_2 = 4.828 \times 10^5 \text{ Pa}$$

$$p_3 := p_2$$

$$p_3 = 4.828 \times 10^5 \text{ Pa}$$

Therefore the shock velocity is:

$$c_s := a_1 \cdot \sqrt{\frac{\gamma_1 - 1}{2 \cdot \gamma_1} + \frac{\gamma_1 + 1}{2 \cdot \gamma_1} \cdot \frac{p_2}{p_1}}$$

$$c_s = 706.573 \frac{\text{m}}{\text{s}}$$

And the velocity of the gas behind the shock is:

$$u_p := \frac{a_1}{\gamma_1} \cdot \left(\frac{p_2}{p_1} - 1 \right) \cdot \sqrt{\frac{\frac{2\gamma_1}{\gamma_1 + 1}}{\frac{p_2}{p_1} + \frac{\gamma_1 - 1}{\gamma_1 + 1}}}$$

$$u_p = 449.94 \frac{\text{m}}{\text{s}}$$

$$T_2 := T_1 \cdot \frac{\frac{\gamma_1 + 1}{\gamma_1 - 1} \frac{p_2}{p_1} + \frac{p_2}{p_1}}{1 + \frac{\gamma_1 + 1}{\gamma_1 - 1} \frac{p_2}{p_1}}$$

$$T_2 = 508.687\text{K}$$

$$T_3 := T_4 \cdot \left(\frac{p_3}{p_4} \right)^{\frac{\gamma_4 - 1}{\gamma_4}}$$

$$T_3 = 160.138\text{K}$$

The densities on both sides of the shock wave are:

$$\rho_1 := \frac{p_1 \cdot \mu_1}{R_g \cdot T_1}$$

$$\rho_1 = 1.201 \frac{\text{kg}}{\text{m}^3}$$

$$\rho_2 := \frac{p_2 \cdot \mu_1}{R_g \cdot T_2}$$

$$\rho_2 = 3.306 \frac{\text{kg}}{\text{m}^3}$$

And the density of the expanding hot gas at the gas boundary is:

$$\rho_3 := \frac{p_3 \cdot \mu_4}{R_g \cdot T_3}$$

$$\rho_3 = 10.521 \frac{\text{kg}}{\text{m}^3}$$

C.3 Combustion calculations

The set of functions collected in this file performs thermodynamic calculations for complete combustion or chemical equilibrium. The first argument of the main function is the name of the subfunction, followed by the arguments for the subfunction.

```
function varargout=combustion_calc(str,varargin)
switch str
case 'compl_comb'
    [varargout{1},varargout{2},varargout{3}]=compl_comb;
case 'incompl_comb'
```

```

    [varargout{1},varargout{2},varargout{3}]=incompl_comb(4);
    case 'equil_temp_res'
        varargout{:}=equil_temp_res(varargin{:});
    case 'compl_vs_incompl'
        compl_vs_incompl();
end;

% A function that calculates the final temperature and
pressure
% as a function of the excess-air ratio lambda
function [lambda,Tcc,pcc]=compl_comb()
PC=[5,4,3,2,1,1];
aH2rev=[-8.35e2,1.99,7e-4,-5.63e-8,-9.23e-12,1.58e-15];
aH2=aH2rev(6:-1:1)./PC;
aO2rev=[-1.23e3,2.70,6.14e-4,-1.26e-7,1.78e-11,-1.14e-15];
aO2=aO2rev(6:-1:1)./PC;
aH2Orev=[-2.99e4,1.67,3.06e-3,-8.37e-7,1.2e-10,-6.39e-15];
aH2O=aH2Orev(6:-1:1)./PC;

T=[1000:10:6000];
T0=300;
p1=6*101;

lambda1=(polyval(aH2,T0)-polyval(aH2,T))./(polyval(aH2O,T)-
polyval(aH2,T)-0.5*polyval(aO2,T0));
lambda2=(polyval(aH2,T0)+0.5*polyval(aO2,T)-
polyval(aH2O,T))./(0.5*polyval(aO2,T)-
0.5*polyval(aO2,T0));
i=1;
while lambda1(i)<1
    lambda(i)=lambda1(i);
    Tcc(i)=T(i);
    i=i+1;
end;
j=length(lambda2);
while lambda2(j)<1
    j=j-1;
end
while j>1;
    lambda(i)=lambda2(j);
    Tcc(i)=T(j);
    j=j-1;
    i=i+1;
end;
alpha=lambda.*(lambda<1)+(lambda>=1);
pcc=p1*(Tcc/T0).*(1+lambda/2-alpha/2)./(1+lambda/2);

% Optional part to graph the results
% plot(lambda,Tcc);hold on; plot(lambda,pcc,'r');hold off;
% axis([0,4,0,8000]);grid on;
% legend('Gas temperature, K','Gas Pressure, kPa');
% xlabel('Excess-air ratio \lambda');
% title('Initial conditions: p_0=600 kPa, T_0=300 K');

% This function calculates the residual function Q1-Q2

```

```

% the root of which gives the chemical equilibrium
    temperature
function [Res,Pres]=equil_temp_res(lambda,T)
PC=[5,4,3,2,1,1];
aH2rev=[-8.35e2,1.99,7e-4,-5.63e-8,-9.23e-12,1.58e-15];
aH2=aH2rev(6:-1:1)./PC;
aO2rev=[-1.23e3,2.70,6.14e-4,-1.26e-7,1.78e-11,-1.14e-15];
aO2=aO2rev(6:-1:1)./PC;
aH2Orev=[-2.99e4,1.67,3.06e-3,-8.37e-7,1.2e-10,-6.39e-15];
aH2O=aH2Orev(6:-1:1)./PC;

T0=300;
p0=101;
p1=6*p0;

alpha1=(polyval(aH2,T)+lambda/2*polyval(aO2,T))-
    (polyval(aH2,T0)+lambda/2*polyval(aO2,T0))...
    ./ (polyval(aH2,T)+0.5*polyval(aO2,T)-polyval(aH2O,T));
alpha=alpha1.*(alpha1<lambda).*(alpha1<1)+(alpha1>=lambda).*
    (alpha1<1)*lambda+(alpha1>=1);
Pres=(p1/p0)*(T/T0).*(1+lambda/2-alpha/2)/(1+lambda/2);
Q1=(1-alpha).*sqrt((lambda-alpha)/2)./(alpha.*(1+(lambda-
    alpha)/2));
Q2=1100*exp(-2.993e4./T)./sqrt(Pres);
%plot(T,alpha);
Res=Q1-Q2;

% This function calculates equilibrium temperature and
    pressure
% as a function of the excess-air ratio using the
    incompl_comb
% residue function
function [lambda,Teq,Peq]=incompl_comb(lambda_max)
T=[1000:10:6000];
Npoints=floor(lambda_max/0.1);
for i=1:Npoints
    lambda(i)=0.1*i;
    [Res,Pres]=equil_temp_res(lambda(i),T);
    %finding the 0 of the residue
    Res=Res>0;
    dRes=diff(Res);
    n=find(dRes);
    if length(n)==0
        Teq(i)=0;
    else
        Teq(i)=T(n(1));
        Peq(i)=Pres(n(1))*101;
    end;
end;
%plot(lambda,Teq);

% Graphs the results for complete and incomplete combustion
function compl_vs_incompl()
[lambda1,Tcc,pcc]=compl_comb;
[lambda2,Teq,peq]=incompl_comb(4);
plot(lambda1,Tcc);
hold on;

```

```
plot(lambda2,Teq,'r');
plot(lambdal,pcc,'g');
plot(lambda2,peq,'m');
hold off;
axis([0,4,0,8000]);grid on;
legend('T complete combustion','T equilibrium','p complete
       combustion','p equilibrium');
xlabel('Excess-air ratio \lambda');
ylabel('Temperature, K ; Pressure, kPa');
title('Initial conditions: p_0=600 kPa, T_0=300 K');
```


References

1. Copenhagen, W. M., D.E.K., R. L. Wood, *Bailey's textbook of histology*. 1978, Williams & Wilkins. p. 423-446.
2. Wikipedia, *Skin*, <http://en.wikipedia.org/wiki/Skin>
3. BBC, *Resurfacing the Skin with Lasers*, <http://www.bbc.co.uk/science/hottopics/extremecosmetics/lasers.shtml>
4. *Epidermis*, <http://webanatomy.net/anatomy/epidermis.jpg>
5. Bos, J.D. and M.L. Kapsenberg, *The skin immune system: progress in cutaneous biology*. Immunol Today, 1993. **14**(2): p. 75-8.
6. Partidos C.D., A.S. Beignon, F. Brown, E. Kramer, J.P. Briand, S. Muller, *Applying peptide antigens onto bare skin: induction of humoral and cellular immune responses and potential for vaccination*. J Control Release, 2002. **85**(1-3): p. 27-34.
7. Williams, I.R. and T.S. Kupper, *Immunity at the surface: homeostatic mechanisms of the skin immune system*. Life Sci, 1996. **58**(18): p. 1485-507.
8. Demicheli V., T. Jefferson, D. Rivetti, J. Deeks, *Prevention and early treatment of influenza in healthy adults*. Vaccine, 2000. **18**(11-12): p. 957-1030.
9. Chen D., M. Burger, Q. Chu, R. Endres, C. Zuleger, H. Dean, LG Payne , *Epidermal powder immunization: cellular and molecular mechanisms for enhancing vaccine immunogenicity*. Virus Res, 2004. **103**(1-2): p. 147-53.
10. Henderson, E.A., T.J. Louie , K. Ramotar , D. Ledgerwood , K.M. Hope, A. Kennedy, *Comparison of higher-dose intradermal hepatitis B vaccination to standard intramuscular vaccination of healthcare workers*. Infect Control Hosp Epidemiol, 2000. **21**(4): p. 264-9.
11. Kane A., J. Lloyd, M. Zaffran, L. Simonsen, M. Kane, *Transmission of hepatitis B, hepatitis C and human immunodeficiency viruses through unsafe injections in the developing world: model-based regional estimates*. Bull World Health Organ, 1999. **77**(10): p. 801-7.
12. Bioject, *Biojector® 2000*, <http://www.bioject.com/biojector2000.html>
13. Biovalve, *Mini-Ject*, <http://www.biovalve.com/products/miniject.shtml>
14. Wendell, D., *Controllable Needle-Free Injection*. 2006, MIT.
15. Yang, S., *Researchers developing MicroJet for ouchless injections*, http://www.berkeley.edu/news/media/releases/2005/03/16_microjet.shtml
16. BioRAD, *Helios Gene Gun*, <http://www.biorad.com>
17. Chiron, *High Speed, Needle-Free Delivery Systems*, <http://www.eng.ox.ac.uk/pjrc/plan.html>
18. Bellhouse, B.J., N.J. Quinlan, and R.W. Ainsworth. *Needle-less delivery of drugs, in dry powder form, using shock waves and supersonic gas flow*. in *21st International Symposium on Shock Waves*. 1997. Great Keppel Island, Australia.
19. Bellhouse, B.J., *Method of delivering powder transdermally with needleless injector*, Patent Number: 5630796, 1997
20. Bellhouse, B., *Particle Delivery*, Patent Number: 6685669, 2004

21. Quinlan, N.J., et al., *Investigation of gas and particle dynamics in first generation needle-free drug delivery devices*. Shock Waves, 2001. **10**: p. 395-404.
22. Liepmann, H. W., A.R., *Elements of Gasdynamics*. 1957: New York, Wiley.
23. Owczarek, J., *Fundamentals of gas dynamics*. 1964: Scranton, International Textbook Co.
24. Rudinger, G., *Nonsteady duct flow, wave-diagram analysis*. 1969: Dover Publications.
25. *Vision Research Inc.*, <http://www.visible-solutions.com/phantomv9.html>
26. Moldovan D., L.G., *Buckling Dynamics of Compressed Thin Sheets (Membranes)*. Physical Review Letters, 1999. **82**(14): p. 2884-2887.
27. Golubovic L., D.M., A. Peredera, *Dynamics of the Euler Buckling Instability*. Physical Review Letters, 1998. **81**(16): p. 3387-3390.
26. Ainsworth R.W., S.J. Thorpe, R.J. Manners, *A new approach to flow-field measurement -- A view of Doppler global velocimetry techniques*, International Journal of Heat and Fluid Flow, Volume 18, Number 1, February 1997, pp. 116-130(15)
27. Meyers, J. F., Development of Doppler global velocimetry as a flow diagnostics tool, 1995 *Meas. Sci. Technol.* **6**, p.769-783